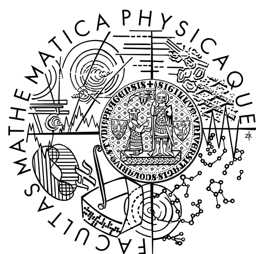

FACULTY
OF MATHEMATICS
AND PHYSICS
Charles University

LIGHT POLARIZATION A PROBE OF NANOMATERIALS

Application of spectroscopic ellipsometry and magneto–optics

Jan MISTRÍK

HABILITATION THESIS

Prague 2022

Table of Contents

Introduction **7**

I Spectroscopic ellipsometry and magneto–optics **9**

1 Light polarization **11**

2 Light-matter interaction **17**
2.1 Macroscopic approach 17
2.1.1 Maxwell's equations and constitutive relations 17
2.1.2 Light propagation 19
Optically isotropic medium 20
Optically anisotropic medium - linear birefringence and dichroism 21
Magneto-optical medium 22
Faraday effect - circular magnetic birefringence and dichroism 24
Voigt effect - linear magnetic birefringence and dichroism 26
2.1.3 Dispersion and Kramers-Kronig relations 27
2.2 Microscopic approach 29
2.2.1 Optical constants 29
2.2.2 Magneto-optical constants 32
2.3 Ab-initio calculations 34

3 Ellipsometry **37**
3.1 Measurable quantities 37
3.1.1 Isotropic case 37
3.1.2 Anisotropic case 40
3.2 Instrumentation 41
3.3 Single interface 43
3.3.1 Optically isotropic sample 44
Fresnel equations 44
Brewster and Principal angles 45
Inverse analytical formula 47
Determination of optical constants of bulk nickel ferrite 47
Beilby overlayer - limitation of single interface approximation 48

3.3.2 Optically anisotropic sample 49
Determination of ordinary and extraordinary refractive index of ZnO and PET . 50
3.3.3 Normal reflectivity and Kramers-Kronig analyses 51
Determination of optical constants of $PbZr_{1/2}Ti_{1/2}O_3$ 52
3.4 Single layer 53
3.4.1 Ideal $As_{50}Se_{50}$ chalcogenide film 55
3.4.2 Assessment of defects in SiO_2 films 57
3.5 Multilayer 59
3.5.1 Inner structure and quality of nanocrystalline diamond films 59
3.6 Linear grating 63
3.6.1 Sinusoidal linear Ni grating 64
3.7 Conclusions 68

4 Magneto–optics **69**
4.1 Measurable quantities 69
4.2 Instrumentation 71
4.3 Single interface 72
4.3.1 Polar Kerr configuration 73
Magneto–optical constants of nickel ferrite determined by analytic formula . . . 76
Beilby overlayer and its curing 77
4.3.2 Longitudinal and transverse Kerr configurations 78
4.3.3 Quadratic magneto-optical effects in reflection 80
4.4 Single layer 83
4.4.1 Propagation and interface contributions 84
4.4.2 Examination of pulsed laser deposited $SmFeO_3$ films 86
Magnetic phase formation and Curie temperature - Faraday rotation magnetometry 87
Film thickness – propagation contribution of polar Kerr rotation spectra 89
4.5 Multilayer 90
4.5.1 Interdiffusion in αFe_2O_3/NiO multilayers 91
4.6 Linear grating 93
4.6.1 Surface oxidation and edge effect of permalloy lamellar gratings . . 95
4.7 Conclusions 98

II Contribution to the field 99

5 Optical and magneto-optical constants **101**
5.1 Combined method of spectroscopic ellipsometry and magneto–optics 101
5.2 Optical ellipsometry 103

6 Characterization of nanostructures **107**
6.1 Single layers 107
6.2 Multilayers 111
6.3 Linear gratings 113

6.4 Complex architectures 114

7 Theoretical approaches **115**

8 Application motivated research **117**
8.1 Murakami Kaimeido, Ltd., Japan 117
8.2 Komatsu Electronics, Ltd., Japan 118
8.3 ELLA-CS, s.r.o., Czech Republic 118
8.4 TOSEDA, s.r.o., Czech Republic 119
8.5 Synthesia, a.s. Czech Republic 119

III Selected papers **121**

9 List of selected publications **123**

Perspectives **125**

Acknowledgement **127**

References **128**

Appendices **140**

A Single interface reflection matrix **141**

Introduction

One of the fundamental properties of light is its polarization. Historically, the first scientific presentation of a phenomenon related to light polarization is credited to Erasmus Bartholin, who in 1669 studied the double refraction of light in a crystal of Iceland spar. Since then, within three centuries, many great scientists have contributed to the description, understanding, and application of light polarization (for a detailed historical survey, refer, for example, to Refs. [1, 2, 3]).

At the end of the nineteenth century, Paul Drude [4, 5, 6] extensively studied the change in the polarization upon light reflection from a sample surface and its correlation with sample optical properties. This technique was later named ellipsometry since elliptical polarization is the most general polarization state of light. Drude also rederived Fresnel's formulas from Maxwell's equations and thus laid the theoretical foundation of ellipsometry. Furthermore, he constructed the very first ellipsometer – an instrument capable of measuring the polarization change in reflected light. Therefore, it is no wonder that Drude is known as the father of ellipsometry.

Optical interaction with a matter depends on its electronic structure. If this interaction is influenced by an external magnetic field or internal magnetic ordering, then we talk about magneto–optical effects. These effects played an important role in clarifying the electromagnetic nature of light, in the development of both classical and quantum theory of electronic structure, and in the discovery of electron spin. In 1845, it was Michael Faraday who first observed rotation of the plane of polarization of linearly polarised light propagating in a glass rod along the direction of an external magnetic field [7]. 30 years later, in 1876, John Kerr detected a similar but considerably weaker effect when the light was reflected from a ferromagnetic mirror magnetized perpendicularly to its surface [8]. Faraday and Kerr effects depend on the polarity of the magnetic field and this makes them particularly different from the change of polarization observed by Drude on a non–magnetized sample surface. Other, well–known magneto–optical phenomenon, linear birefringence of light induced by a magnetic field oriented perpendicularly to the direction of light propagation was first observed by W. Voigt in 1897. He also published the very first book about magneto–optics [9]. Voigt effect is quadratic (even) in magnetization, whereas Faraday and Kerr effects are in magnetization linear (odd), which is important for applications. The theoretical frame for the understanding of magneto–optical effects was laid down by P. Zeeman by his discovery of atomic spectral line splitting due to external magnetic field [10]. Soon after this discovery, classical microscopic models were proposed to clarify the origin of magneto–optical effects. However, these early models did not take

into account the quantum nature of these effects and therefore, were not satisfactory. On the other hand, macroscopic formal description of the magneto–optical effects that was pioneered by C. G. Darwin [11] had no such limitations.

During the last century, numerous researchers significantly improved both the theoretical concepts and instrumentation of optical and magneto–optical ellipsometry. Simultaneously, materials databases with accurately determined optical and magneto–optical constants were considerably expanded. This effort was particularly triggered by the needs of the semiconductor and data storage industry for the production of high-quality microelectronics and high capacity (magneto)–optical discs. The increased performance of personal computers, in turn, made possible further improvements in the numerical treatment of ellipsometry data and automation of fast spectroscopic ellipsometers. Presently, ellipsometry is a highly accurate and precise surface characterization tool that is routinely used for the determination of bulk, single, and multilayer optical and structural parameters and their magnetic ordering. Moreover, it is worth noting that ellipsometry recently gave evidence of its potentiality in the characterization of modern nanostructured materials such as gratings, photonic crystals, or plasmonic materials (see [12] and references therein). This opens promising perspectives for further development of these methods.

This thesis consists of two parts. The first part aims to provide a brief introduction to optical and magneto-optical ellipsometry, starting with an overview of light polarization, light–matter interaction, the definition of measurable quantities, and instrumentation. The applications of ellipsometry (optical and magneto–optical) to "standard" systems such as bulks, single layers, and multilayers are also provided. The key theoretical formulas and approaches are supported by selected case studies that I carried out on real samples. The final sections in both optical and magneto–optical chapters deals with scatterometry. Described is one of its particular applications, id est, characterization of linear gratings. The advantages and disadvantages together with the complementarity of optical and magneto–optical ellipsometry with respect to conventional techniques are continuously mentioned to underscore the real value of these methods. As far as I know, this introductory text covering both spectroscopic ellipsometry and magneto-optics that are closely related is not available. I hope it will be of interest to students and newcomers in the field. The ellipsometry section is an expanded version of book chapter that I published in [13]. The second part of the thesis summarizes my main contributions to the presented field, particularly in (i) determination of new or refinement of existing optical and magneto–optical constants of selected materials, (ii) characterization of various nanostructures, (iii) theoretical approach refinement, and (iv) contribution to the application motivated research with industrial partners. The thesis is concluded by an overview of future perspectives and acknowledgments. The attached appendices cover (i) explicit representation of reflection matrix derived for single interface and general form of permittivity tensor and (ii) my selected papers.

Part I

Spectroscopic ellipsometry and magneto–optics

Chapter 1

Light polarization

Within the framework of electromagnetic theory, light propagating in a vacuum can be described as a transverse electromagnetic wave. The spatial and temporal dependencies of electric and magnetic field vectors, which are transverse to each other and are perpendicular to the direction of propagation, are important contributors to light polarization. Several approaches have been developed to describe different polarization states (see, e.g. [1]). Here, we briefly introduce basic ideas that will be employed in the following chapters. To keep the formalism (and figures) as simple as possible, we assume a plane monochromatic wave propagating in a vacuum along the z-axis. Plane monochromatic wave is a solution of the wave equation (1.1), derived from Maxwell equations[1] (1.2-1.5).

$$\Delta \boldsymbol{E} = \frac{1}{c^2}\frac{\partial^2 \boldsymbol{E}}{\partial t^2} \tag{1.1}$$

$$\nabla \cdot \boldsymbol{E} = 0 \tag{1.2}$$

$$\nabla \times \boldsymbol{E} = -\frac{\partial \boldsymbol{B}}{\partial t} \tag{1.3}$$

$$\nabla \cdot \boldsymbol{B} = 0 \tag{1.4}$$

$$\nabla \times \boldsymbol{B} = \varepsilon_0 \mu_0 \frac{\partial \boldsymbol{E}}{\partial t} \tag{1.5}$$

Vacuum phase velocity of light c is equal to $(\varepsilon_0\mu_0)^{-\frac{1}{2}}$, where ε_0 and μ_0 are electric permittivity and magnetic permeability of a vacuum, respectively. We usually select the electric intensity $\boldsymbol{E}$ of an electromagnetic wave to represent the light behavior. The main reason for this is that the magnetic induction $\boldsymbol{B}$ can always be calculated from the electric field using Maxwell's equations [2]; also, in optical frequencies, the magnetic field is often less important than the electric field when considering light interaction with the matter [14, 15].

The most general case of spatial dependence of the electric field vector in the wave is

[1] No charge and current density is considered in a vacuum. Maxwell equations and constitutive relations for solids are introduced and discussed in the following chapter.

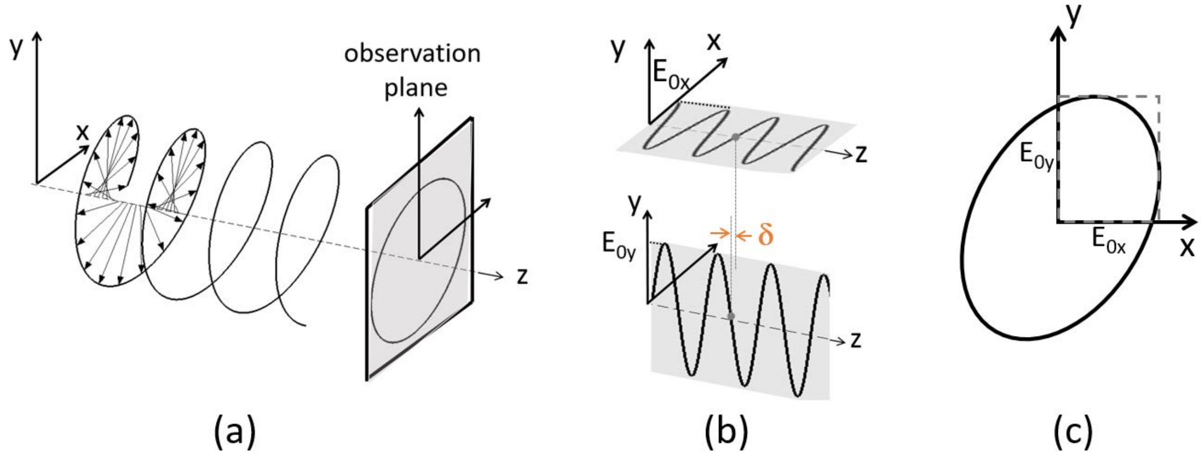

Fig. 1.1: Spatial dependence of an electric field in an ellipticaly polarized wave (a). Its orthogonal components and their relative phase shift (b). Ellipse of polarization in the observation plane (c).

schematically presented in Figure 1.1a. Its orthogonal components E_x and E_y

$$E_x = E_{0x}\, e^{i(\omega t - kz + \delta_x)} \tag{1.6}$$
$$E_y = E_{0y}\, e^{i(\omega t - kz + \delta_y)} \tag{1.7}$$

mutually shifted in phase by $\delta = \delta_y - \delta_x$ and with amplitudes E_{0x} and E_{0y} are presented in Figure 1.1b. Here ω is the wave angular frequency, and k is the wavenumber of the plane wave. The absolute phases of the x and y components are denoted as δ_x and δ_y, respectively. In a plane perpendicular to the z-axis (let us call it the observation plane), the time dependence of the electric field vector $\boldsymbol{E}(t)$ can be imagined as a superposition of the two orthogonal electric vibrations $E_x(t)$ and $E_y(t)$ and It can be shown [16] that Eqs. (1.6) and (1.7) can be reorganized there to the equation of an ellipse

$$\left(\frac{E_x}{E_{0x}}\right)^2 + \left(\frac{E_y}{E_{0y}}\right)^2 - 2\frac{\cos\delta}{E_{0x}E_{0y}}E_xE_y = \sin^2\delta \tag{1.8}$$

Hence, the endpoint of the electric field vector $\boldsymbol{E}(t)$ traces in the observation plane an ellipse (cf. Figure 1.1a and 1.1c) as the wave propagates, and we call this electromagnetic wave elliptically polarized.

In ellipsometry and magneto-optics, it is the shape of the ellipse and its orientation (with respect to the system of coordinates) that is important. Therefore, the light intensity

$$I = \frac{1}{2}c\varepsilon_0\left(E_{0x}^2 + E_{0y}^2\right),$$

which is related to the size of the ellipse, is usually normalized to unity and then only two real parameters are sufficient to define the polarization state (for example relative phase shift δ and amplitude ratio E_{0x}/E_{0y}).

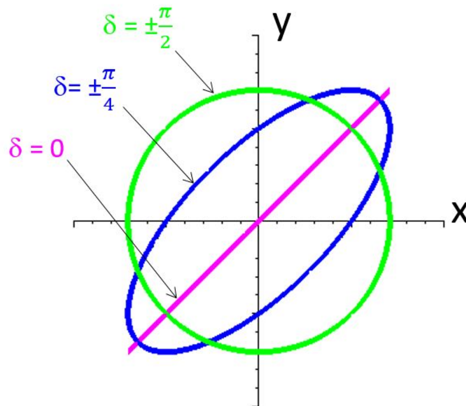

Fig. 1.2: Linear(pink), elliptical (blue), and circular (green) polarization together with the relative shift δ. The component amplitudes E_{0x} and E_{0y} are considered to be equal.

The linear ($\delta = 0, \pm\pi, \pm 2\pi, \ldots$) and circular ($E_{0x} = E_{0y}$ and $\delta = \pm\frac{\pi}{2}, \pm\frac{3\pi}{2}, \ldots$) polarizations are special cases of the general elliptical polarization state. Selected cases of light polarization are shown in Figure 1.2. Note that the sign of δ determines the handedness (for example, left-handed or right-handed circular polarization). In fact, it is not only the spatial dependence of electric field $\boldsymbol{E}$ but also its temporal dependence in terms of its handedness that plays important role in light interaction with a medium (cf. Section 2.2.2).

As all useful information on the polarization state lies in its component amplitudes and phases, it is convenient to combine them into a single quantity: the complex amplitudes

$$\hat{E}_x = E_{0x}\, e^{i\delta_x} \tag{1.9}$$

$$\hat{E}_y = E_{0y}\, e^{i\delta_y} \tag{1.10}$$

Any change in the polarization is then solely expressed by these complex amplitudes of the wave. However, there are many other parameters that can be used for the description of the polarization state as well (for an exhaustive review on this topic refer, for example, to [1]). Given the focus of this work, we introduce here parameters that are closely related to ellipsometric and magneto-optical measurable quantities. In ellipsometry we encounter angles α and δ whose definition are mentioned in Tab. 1.1. Angle δ, as it was already pointed out, gives phase shift of the x and y wave component, and angle α expresses the ratio of their amplitudes (cf. Fig. 1.3). On the other hand, in the field of magneto–optics, we use angles θ and ϵ. Parameter θ, known as *azimuth*, gives an angle between Cartesian axis x and major semi–axis of the polarization ellipse (cf. Fig. 1.3). Parameter ϵ is called *angle of ellipticity* and is defined as

$$\tan\epsilon = \pm\frac{a}{b}\,, \tag{1.11}$$

where a and b stands for minor and major semi–axis, respectively. The sign plus corresponds to the right-handed polarized wave for which the electric field vector rotates

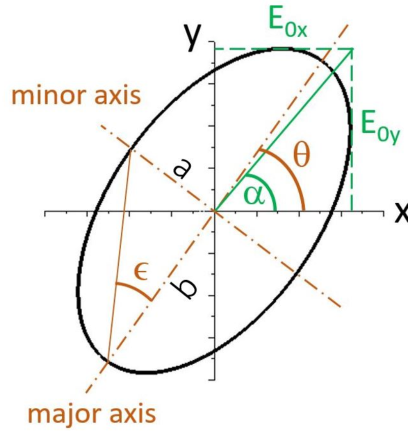

Fig. 1.3: Geometric meaning of polarization ellipse parameters used in ellipsometry and magneto-optics.

clockwise when looking into the beam. For the left-handed wave, we set the minus sign.

It is obvious that all parameters describing light polarization are inter–related. Relation between ellipsometric and magneto–optical parameters and amplitudes and phase difference of x and y light components are listed in Tab. 1.1.

Ellipsometry	Magneto-optics
$\tan\alpha = \frac{E_{0y}}{E_{0x}}$, $\delta = \delta_y - \delta_x$	$\tan 2\theta = \frac{2E_{0x}E_{0y}}{E_{0x}^2 + E_{0y}^2}\cos\delta$, $\tan 2\epsilon = \frac{2E_{0x}E_{0y}}{E_{0x}^2 + E_{0y}^2}\sin\delta$
$\cos 2\alpha = \cos 2\epsilon \cos 2\theta$, $\tan\delta = \tan 2\epsilon(\sin 2\theta)^{-1}$	$\tan 2\theta = \tan 2\alpha \cos\delta$, $\sin 2\epsilon = \sin 2\alpha \sin\delta$

Tab. 1.1: Parameters of polarization ellipse used in ellipsometry and magneto-optics and their inter–relation [3].

We do not deal with unpolarized or partially polarized light here, even though these polarization states become important when a depolarizing sample comes under examination. Partially polarized light and its interaction with solids are treated in more detail, for example, in Ref. [3].

Given the forthcoming discussion of the microscopic origin of magneto–optical effects in Section 2.2.2, it is worth giving a note here about spin and helicity of photons. The concept of light polarization is in quantum electrodynamics associated with the spin momentum of a photon. Photons can exist in two states with angular momentum projection $m = \pm 1$ (the helicities), and their moment magnitudes are $\pm\hbar$. These photons are asso-

ciated with electromagnetic waves having left (right) circular polarization[2]. Elliptically and linearly polarized light is, in the quantum concept, a superposition of photons with different helicities.

[2]The handedness of the waves, helicities of photons, and sign convention applied in magneto–optics is discussed, for example, in [17].

Chapter 2

Light-matter interaction

As it was already mentioned in Introduction, the optical and magneto–optical properties of a matter are strongly related to its electronic structure. Light–matter interaction can be treated in macroscopic or microscopic frames. The macroscopic approach is governed by Maxwell's equations coupled with constitutive relations, whereas the microscopic approaches are based on classical or semi–quantum electrodynamics. With increasing computer power, the electronic band structure of solids can be calculated from the first principles as well. Recent significant progress in the ab–initio calculations allowed theoretical prediction of optical and magneto-optical effects with reasonable accuracy.

2.1 Macroscopic approach

In this section, we present Maxwell's equations and constitutive relations in the form they usually appear in optics and magneto–optics. Particular care is devoted to applied approximations when deriving optical and magneto–optical material constants. The work of Wooten [18] and Collins [19] (optics), and Wettling [20] (magneto–optics) is mostly followed.

2.1.1 Maxwell's equations and constitutive relations

Assuming no external charges and currents in a solid, Maxwell equations get the form presented in Table (2.1). Induced charge density ρ and current density $\boldsymbol{j}$ are mainly due to light interaction with bound electrons from valence band (ρ_{bound}, $\boldsymbol{j}_{bound}$) and with free electrons from conduction band ($\boldsymbol{j}_{cond}$). These are usually approximated by induced polarization $\boldsymbol{P}$ and magnetization $\boldsymbol{M}$ of a medium[1]

$$\rho = \rho_{bound} = -\nabla \cdot \boldsymbol{P}\,, \tag{2.1}$$

$$\boldsymbol{j} = \boldsymbol{j}_{bound} + \boldsymbol{j}_{cond} = \frac{\partial \boldsymbol{P}}{\partial t} + \nabla \times \boldsymbol{M} + \boldsymbol{j}_{cond}\,. \tag{2.2}$$

[1] Mentioned are only the first terms of multipole moments expansion [21, 22].

Tab. 2.1	Tab. 2.2	Tab. 2.3
$\nabla \cdot \boldsymbol{E} = \frac{\rho}{\varepsilon_0}$	$\nabla \cdot \boldsymbol{D}_r = 0$	$\nabla \cdot \boldsymbol{D} = 0$
$\nabla \times \boldsymbol{E} = -\frac{\partial \boldsymbol{B}}{\partial t}$	$\nabla \times \boldsymbol{E} = -\frac{\partial \boldsymbol{B}}{\partial t}$	$\nabla \times \boldsymbol{E} = -\frac{\partial \boldsymbol{B}}{\partial t}$
$\nabla \cdot \boldsymbol{B} = 0$	$\nabla \cdot \boldsymbol{B} = 0$	$\nabla \cdot \boldsymbol{B} = 0$
$\nabla \times \boldsymbol{B} = \mu_0(\varepsilon_0 \frac{\partial \boldsymbol{E}}{\partial t} + \boldsymbol{j})$	$\nabla \times \boldsymbol{H} = \frac{\partial \boldsymbol{D}_r}{\partial t} + \boldsymbol{j}_{cond}$	$\nabla \times \boldsymbol{H} = \frac{\partial \boldsymbol{D}}{\partial t}$

We can formally eliminate the appearance of bound charges ρ_{bound} and related currents $\boldsymbol{j}_{bound}$ from Maxwell equations introducing the electric displacement $\boldsymbol{D}_r$ and magnetic intensity $\boldsymbol{H}$ by relations

$$\boldsymbol{D}_r = \varepsilon_0 \boldsymbol{E} + \boldsymbol{P}\,, \tag{2.3}$$

$$\boldsymbol{H} = \frac{1}{\mu_0}\boldsymbol{B} - \boldsymbol{M}\,. \tag{2.4}$$

With the help of these quantities, Maxwell's equations get the form mentioned in Table 2.2. Both, the electric displacement and magnetic intensity, are real vectors, and we label the displacement vector $\boldsymbol{D}_r$ by a subindex r to distinguish it from its complex value counterpart $\boldsymbol{D}$ that is defined later in Eq. (2.10).

Within the approximation of linear optics, we can further express the polarization $\boldsymbol{P}$ and magnetization $\boldsymbol{M}$ by the electric χ_e and magnetic χ_m susceptibility, respectively

$$\boldsymbol{P} = \varepsilon_0 \chi_e \boldsymbol{E}\,, \tag{2.5}$$

$$\boldsymbol{M} = \chi_m \boldsymbol{H}\,. \tag{2.6}$$

Constitution relations (2.3) and (2.4) that supplements Maxwell's equations from Tab. 2.2 can be written in a compact form introducing the relative electric permittivity ε_r and the relative magnetic permeability μ_r of a medium

$$\boldsymbol{D}_r = \varepsilon_0 \varepsilon_r \boldsymbol{E}\,, \tag{2.7}$$

$$\boldsymbol{B} = \mu_0 \mu_r \boldsymbol{H}\,, \tag{2.8}$$

$$\boldsymbol{j}_{cond} = \sigma_r \boldsymbol{E}\,. \tag{2.9}$$

A complete set of these constitutive relations includes also Ohm's law, Eq. (2.9), with the electric conductivity σ_r of a medium. All the material constants ε_r, μ_r, and σ_r are real quantities, and this is indicated by subindex r. In the range of optical frequencies, the relative permeability μ_r gets for most of materials value close to unity [14, 15, 21]. Therefore, only the electric field of the light $\boldsymbol{E}$ is considered in the light–matter interaction.

It is further convenient to introduce the **complex** electric displacement $\boldsymbol{D}$ that covers both effects of bound and free charges

$$\boldsymbol{D} = \boldsymbol{D}_r - \frac{i}{\omega}\boldsymbol{j}_{cond}\,. \tag{2.10}$$

As a result, we can combine the two material relations (2.7) and (2.9) into one complex

$$\boldsymbol{D} = \varepsilon_0\varepsilon_r\boldsymbol{E} - \frac{i}{\omega}\sigma_r\boldsymbol{E}\,, \tag{2.11}$$
$$= \varepsilon_0\varepsilon\boldsymbol{E}\,, \tag{2.12}$$

where the electric permittivity ε of a material becomes a **complex** quantity with real ε_r and imaginary ε_i parts

$$\varepsilon = \varepsilon_r - i\varepsilon_i\,, \tag{2.13}$$
$$= \varepsilon_r - i\frac{\sigma_r}{\varepsilon_0\omega}\,. \tag{2.14}$$

Introducing the complex displacement $\boldsymbol{D}$ into the Maxwell's equations (Tab.2.2), these can be rewritten into the final form presented in Tab. 2.3. The corresponding constitutive relations are then

$$\boldsymbol{D} = \varepsilon_0\varepsilon\boldsymbol{E}\,, \tag{2.15}$$
$$\boldsymbol{B} = \mu_0\boldsymbol{H}\,. \tag{2.16}$$

To conclude this section, it is worth noting *complex* optical conductivity σ that is in some cases (for example, in theoretical ab–inition calculations) preferred quantity over the electrical permittivity ε. Both complex material constants are related to each other by relation

$$\sigma = i\varepsilon_0\omega(1-\varepsilon)\,, \tag{2.17}$$

that can be reformulated in terms of its real σ_r and imaginary σ_i parts

$$\sigma = \sigma_r - i\sigma_i\,, \tag{2.18}$$
$$= \sigma_r - i\varepsilon_0\omega(1-\varepsilon_r)\,. \tag{2.19}$$

In the following sections, we treat light propagation in isotropic, anisotropic, and magneto-optical media, taking into consideration the particular form (scalar or tensor) of their complex electric permittivity ε.

2.1.2 Light propagation

The wave equation derived for vacuum, Eq. (1.1), is no longer valid for a solid that is characterized by electric permittivity ε. Maxwell's equations (cf. Tab. 2.3)

$$\nabla\times\boldsymbol{E} = -\frac{\partial\boldsymbol{B}}{\partial t}\,, \tag{2.20}$$
$$\nabla\times\boldsymbol{H} = \frac{\partial\boldsymbol{D}}{\partial t}\,, \tag{2.21}$$

together with the constitutive relations (2.15), (2.16), and with help of vector algebra identity

$$\nabla\times\nabla\times\boldsymbol{V} = \nabla(\nabla\cdot\boldsymbol{V}) - \Delta\boldsymbol{V}\,, \tag{2.22}$$

leads to the wave equation

$$\Delta \boldsymbol{E} - \nabla(\nabla \cdot \boldsymbol{E}) = \frac{\varepsilon}{c^2}\frac{\partial^2 \boldsymbol{E}}{\partial t^2}\,. \tag{2.23}$$

Assuming a plane wave solution

$$\boldsymbol{E}(\boldsymbol{r}, t) = \hat{\boldsymbol{E}}_0\, e^{i(\omega t - \boldsymbol{k}\cdot\boldsymbol{r})}\,, \tag{2.24}$$

the wave equation (2.23) can be transformed to the form

$$\boldsymbol{k}^2 \boldsymbol{E}_0 - \boldsymbol{k}(\boldsymbol{k}\cdot\boldsymbol{E}_0) = \frac{\omega^2}{c^2}\varepsilon \boldsymbol{E}_0\,, \tag{2.25}$$

that is also known as the Fresnel equation [2].

Optically isotropic medium

The electric permittivity ε of optically isotropic media (amorphous, polycrystalline, and crystalline solids with cubic symmetry) is a scalar quantity. An electromagnetic wave propagating in such media carries an electric field $\boldsymbol{E}$ that is parallel to the displacement vector $\boldsymbol{D}_r$ and perpendicular to the wave vector $\boldsymbol{k}$. In this case, the Fresnel wave equation (2.25) reduces to

$$k^2 = \left(\frac{\omega}{c}\right)^2 \varepsilon\,, \tag{2.26}$$

and can be further rewritten to the form

$$k = \frac{\omega}{c} N\,, \tag{2.27}$$

where the complex refractive index $N = n - i\kappa$ was defined by relation

$$N = \sqrt{\varepsilon}\,. \tag{2.28}$$

Here n is the usual refractive index which determines the phase velocity $v_p = c/n$ and κ is the extinction coefficient which is related to the absorption coefficient α by

$$\alpha = \frac{4\pi\kappa}{\lambda}\,. \tag{2.29}$$

The inverse of the absorption coefficient, $1/\alpha$, is the penetration depth of the light, i.e., estimated distance where the light penetrates under the sample surface (in case of normal incidence). The real and imaginary parts of the electric permittivity and refractive index are inter–related by the following formulas

$$\varepsilon_r = n^2 - \kappa^2\,, \tag{2.30}$$

$$\varepsilon_i = 2n\kappa\,, \tag{2.31}$$

and

$$n = \sqrt{\frac{\varepsilon_r + \sqrt{\varepsilon_r^2 + \varepsilon_i^2}}{2}}\,, \tag{2.32}$$

$$\kappa = \sqrt{\frac{-\varepsilon_r + \sqrt{\varepsilon_r^2 + \varepsilon_i^2}}{2}}\,. \tag{2.33}$$

Due to the isotropic nature of the medium, any polarization state of the light is the proper mode, i.e., it does not change during light propagation and does not depend on the light direction in a material. The latter holds for the refractive index as well.

Optically anisotropic medium - linear birefringence and dichroism

Electric permittivity of crystals with lower structural symmetry takes form of a second–rank tensor

$$\varepsilon = \begin{bmatrix} \varepsilon_{11} & \varepsilon_{12} & \varepsilon_{13} \\ \varepsilon_{21} & \varepsilon_{22} & \varepsilon_{23} \\ \varepsilon_{31} & \varepsilon_{32} & \varepsilon_{33} \end{bmatrix}. \tag{2.34}$$

For materials that are not optically or magneto–optically active, the tensor is symmetric (this holds even for the spectral range where the material is absorbing). For crystals where the reference frame can be oriented along the main crystallographic axes, the permittivity tensor becomes diagonal

$$\varepsilon = \begin{bmatrix} \varepsilon_{11} & 0 & 0 \\ 0 & \varepsilon_{22} & 0 \\ 0 & 0 & \varepsilon_{33} \end{bmatrix}. \tag{2.35}$$

The number of its independent elements, and thus, the uniaxial or biaxial nature of material optical anisotropy, depends on its structural symmetry. For more details refer, for example, to Refs. [19, 22, 2].

Let us consider the orientation of the reference system where the permittivity tensor becomes diagonal (so–called principal axes frame), and let us suppose that the light propagates along the direction defined by a unity vector $\boldsymbol{s}$. Introducing *reduced wave vector* $\bar{\boldsymbol{N}}$

$$\bar{\boldsymbol{N}} \equiv \frac{c}{\omega}\boldsymbol{k} = N\boldsymbol{s}\,, \tag{2.36}$$

where N is the complex refractive index, the wave equation (2.25) for anisotropic media can be reformulated to the Fresnel's equation of wave normals

$$\frac{s_x^2}{N^2 - \varepsilon_{11}} + \frac{s_y^2}{N^2 - \varepsilon_{22}} + \frac{s_z^2}{N^2 - \varepsilon_{33}} = \frac{1}{N^2}\,. \tag{2.37}$$

This equation gives, in general, two solutions of refractive index N for every direction vector $\boldsymbol{s}$. Thus, every $\boldsymbol{s}$ corresponds to two waves with different phase velocities c/n and extinctions. It can be further shown that these waves (proper modes) are linearly

polarized and can propagate in any given direction alone or superposed to each other. Optical effects that arise from the difference of real and imaginary parts of the refractive indices are known as linear birefringence and linear dichroism, respectively[2].

Alternatively, one can get the solution of the Fresnel equation (2.25) in the form of so-called index ellipsoid (or optical indicatrix) defined by the relation

$$\frac{x}{\varepsilon_{11}} + \frac{y}{\varepsilon_{22}} + \frac{z}{\varepsilon_{33}} = 1\,. \tag{2.38}$$

Cross–section of the indicatrix with the plane normal to the direction of light propagation $\boldsymbol{s}$ (colinear with the wave vector $\boldsymbol{k}$) gives an ellipse (cf. Figure 2.1a). Its two semi–axes define two orthogonal directions of proper linear modes (indicated by electric displacement D_1 and D_2). These two modes experience two different refractive indices N_1 and N_2 (cf. Figure 2.1b). If the wave propagating along direction $\boldsymbol{s}$ contains contributions of both proper modes, then, due to the difference of their refractive indices, it encounters a change of polarization as indicated in Figure 2.1c.

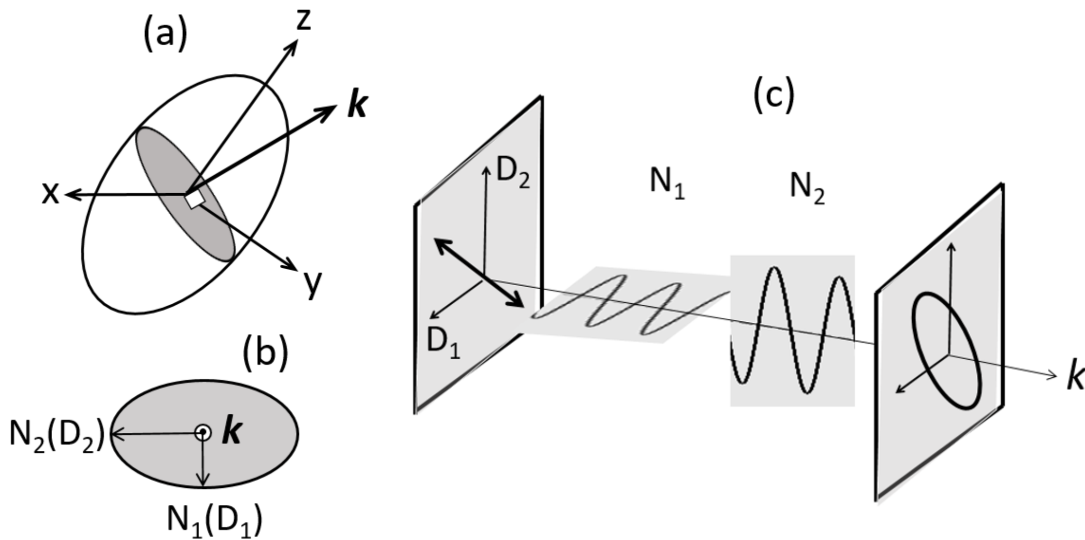

Fig. 2.1: Fresnel indicatrix a), its cross-section b), and linearly polarized proper modes propagating in an optically anisotropic medium c). Refractive indices N_1 and N_2 and polarization change due to linear birefringence nan dichroism are indicated as well.

Magneto-optical medium

Phenomenological description of light interaction with an optically isotropic but magnetically ordered media or media placed in an external magnetic field has a lot in common

[2]Circular birefringence and circular dichroism refer to chiroptical effects of optically active media.

with crystal optics. That is because the net magnetization or the applied magnetic field reduces the spatial symmetry of the system. In the case of isotropic non–absorbing medium subjected to a static magnetic field[3] with magnetic intensity $\boldsymbol{H}$ the constitutive relation (2.15) gets more elaborated form [21, 22]

$$\boldsymbol{D} = \varepsilon_0 \varepsilon \boldsymbol{E} + i\, f \cdot [\boldsymbol{E} \times \boldsymbol{H}]\,, \tag{2.39}$$

where ε is electric permittivity of isotropic medium and f is a material factor[4]. Equation (2.39) can be formally rewritten to the compact form

$$\boldsymbol{D} = \varepsilon_0 \boldsymbol{\varepsilon} \boldsymbol{E}\,. \tag{2.40}$$

However, $\boldsymbol{\varepsilon}$ is no more scalar quantity. It becomes a tensor whose diagonal elements are equal to isotropic permittivity ε and antisymmetric off–diagonal elements emerge from vector product of the electric and magnetic fields on the right-hand side of Eq. (2.39). Consider, for comparison, permittivity tensors associated with polar, Eq. (4.11), longitudinal, Eq. (4.19) and transverse, Eq. (4.24), linear magneto–optical effects.

In the general case of magnetically ordered absorbing crystalline solids, permittivity tensor $\boldsymbol{\varepsilon}$ can be decomposed into two contributions,

$$\boldsymbol{\varepsilon} = \boldsymbol{\varepsilon}(\boldsymbol{0}) + \Delta\boldsymbol{\varepsilon}(\boldsymbol{M})\,. \tag{2.41}$$

where the second contribution $\Delta\boldsymbol{\varepsilon}(\boldsymbol{M})$ arises from magnetic ordering and therefore is dependent on magnetization $\boldsymbol{M}$. It can be shown that $\Delta\boldsymbol{\varepsilon}(\boldsymbol{M})$ contains Hermitian (relating to dispersion) and anti–Hermitian (relating to absorption) parts [20]. As it is often encountered in the experiment, the influence of magnetic ordering on permittivity elements is relatively weak. Therefore, it is appropriate to expand them to the McLauren series

$$\varepsilon_{ij} = \varepsilon_{ij}(0) + \left(\frac{\partial \varepsilon_{ij}}{\partial M_k}\right)_{\boldsymbol{M}=0} M_k + \frac{1}{2}\left(\frac{\partial^2 \varepsilon_{ij}}{\partial M_k \partial M_l}\right)_{\boldsymbol{M}=0} M_k M_l + \ldots \tag{2.42}$$

$$= \varepsilon_{ij}(0) + K_{ijk} M_k + G_{ijkl} M_k M_l + \ldots \tag{2.43}$$

$$= \varepsilon_{ij}(0) + \varepsilon_{ij}(1) + \varepsilon_{ij}(2) + \ldots\ , \tag{2.44}$$

where $\varepsilon_{ij}(0)$ stands for permittivity tensor elements without magnetization, K_{ijk} and and G_{ijkl} are components of so called *linear* and *quadratic* magneto–optical tensor, respectively, and $\boldsymbol{M}$ is magnetisation vector. Indices i, j, k, l represent Cartesian's coordinates.

In magneto–optics Onsager's general principle of microscopic reversibility [23] leads to the important relation

$$\varepsilon_{ij}(\boldsymbol{M}) = \varepsilon_{ji}(-\boldsymbol{M})\,, \tag{2.45}$$

[3] Relatively low magnetic field intensity is expected here to meet requirements for linear approximation discussed later in the text.

[4] This constitution relation is formally similar with a chiral medium that manifests optical activity. The imaginary part $f \cdot [\boldsymbol{E} \times \boldsymbol{H}]$ is in the chiral case replaced by $\beta \cdot [\boldsymbol{k} \times \boldsymbol{E}]$.

Onsager principle, structural crystal symmetry, and orientation of magnetization vector determines which of permittivity tensor elements $\varepsilon_{ij}(0)$, K_{ijk}, G_{ijkl} become null [24]. For crystalline medium with cubic symmetry we get

$$\boldsymbol{\varepsilon(0)} = \begin{bmatrix} \varepsilon_1 & 0 & 0 \\ 0 & \varepsilon_1 & 0 \\ 0 & 0 & \varepsilon_1 \end{bmatrix}, \tag{2.46}$$

$$\begin{bmatrix} \varepsilon_{23}(1) \\ \varepsilon_{31}(1) \\ \varepsilon_{12}(1) \end{bmatrix} = \begin{bmatrix} K_{123} & 0 & 0 \\ 0 & K_{123} & 0 \\ 0 & 0 & K_{123} \end{bmatrix} \begin{bmatrix} M_1 \\ M_2 \\ M_3 \end{bmatrix}, \tag{2.47}$$

$$\begin{bmatrix} \varepsilon_{11}(2) \\ \varepsilon_{22}(2) \\ \varepsilon_{33}(2) \\ \varepsilon_{23}(2) \\ \varepsilon_{31}(2) \\ \varepsilon_{12}(2) \end{bmatrix} = \begin{bmatrix} G_{11} & G_{12} & G_{12} & 0 & 0 & 0 \\ G_{12} & G_{11} & G_{12} & 0 & 0 & 0 \\ G_{12} & G_{12} & G_{11} & 0 & 0 & 0 \\ 0 & 0 & 0 & 2G_{44} & 0 & 0 \\ 0 & 0 & 0 & 0 & 2G_{44} & 0 \\ 0 & 0 & 0 & 0 & 0 & 2G_{44} \end{bmatrix} \begin{bmatrix} M_1^2 \\ M_2^2 \\ M_3^2 \\ M_2M_3 \\ M_3M_1 \\ M_1M_2 \end{bmatrix}. \tag{2.48}$$

It can be proved that $\varepsilon_{ij}(1) = -\varepsilon_{ji}(1)$ and $\varepsilon_{ij}(2) = \varepsilon_{ji}(2)$ [25]. The first term in McLauren expansion $\boldsymbol{\varepsilon(0)}$ and lineal magneto–optical tensor of the third rank K_{ijk} is independent on the orientation of crystallographic axes. Nevertheless, the quadratic magneto–optical tensor G_{ijkl} that is of the fourth rank is on this orientation sensitive. That can be taken as an advantage and applying this phenomenon for accurate characterizations of crystals with cubic symmetry (for more detail refer to Section 4.3.3). The present form of the quadratic magneto–optical tensor G_{ijkl} corresponds to the case when the main crystallographic and Cartesian axes coincide. A more detailed discussion of quadratic magneto–optical tensor properties in cubic crystals can be found, for example, in Refs. [26, 27, 28, 29].

Next, we describe light propagation in a cubic crystal that is magnetized either parallel or perpendicular to the wave vector. In the former case, one observes the Faraday rotation, also known as magnetic circular birefringence (MCB), and magnetic circular dichroism (MCD). The latter case refers to the Voigt effect, id est, magnetic linear birefringence (MLB), and magnetic linear dichroism (MLD). Magneto–optical effects in reflection will be treated later in Chapter 4.

Faraday effect - circular magnetic birefringence and dichroism

Let's suppose that both the magnetization vector $\boldsymbol{M}$ and the wave vector $\boldsymbol{k}$ are oriented along z-direction. Then the permittivity tensor $\boldsymbol{\varepsilon}(\boldsymbol{M})$ expanded up to the second order, cf. Eq. (2.42), takes form

$$\boldsymbol{\varepsilon} = \begin{bmatrix} \varepsilon_1 + G_{12}M_3^2 & KM_3 & 0 \\ -KM_3 & \varepsilon_1 + G_{12}M_3^2 & 0 \\ 0 & 0 & \varepsilon_1 + G_{11}M_3^2 \end{bmatrix}, \tag{2.49}$$

$$= \begin{bmatrix} \varepsilon_{11} & \varepsilon_{12} & 0 \\ -\varepsilon_{12} & \varepsilon_{11} & 0 \\ 0 & 0 & \varepsilon_{33} \end{bmatrix}, \tag{2.50}$$

where we have used Eqs. (2.46) – (2.48) and simplified notation of the linear magneto–optical tensor considering $K_{ijk} = K$. Magnetization, in this particular configuration, induce the gyrotropic effect that is manifested by the off–diagonal permittivity tensor elements ε_{12}, ε_{21}, and uniaxial optical anisotropy by means of inequality $\varepsilon_{11} = \varepsilon_{22} \neq \varepsilon_{33}$ of the diagonal tensor elements. The gyrotropic effect is due to linear, whereas the uniaxial anisotropy is due to quadratic magneto–optical tensor. Inserting permittivity tensor (2.50) to the wave equation (2.25) yields

$$(N^2 - \varepsilon_{11})E_{01} - \varepsilon_{12}E_{02} = 0\,, \tag{2.51}$$

$$\varepsilon_{12}E_{01} + (N^2 - \varepsilon_{11})E_{02} = 0\,, \tag{2.52}$$

from which immediately follows

$$N_{\pm}^2 = \varepsilon_{11} \pm i\varepsilon_{12}\,, \tag{2.53}$$

and

$$E_{02} = \pm iE_{01}\,. \tag{2.54}$$

It means that proper modes of light propagation in this configuration are left (–) and right (+) circularly polarised waves with different dispersion and absorption.

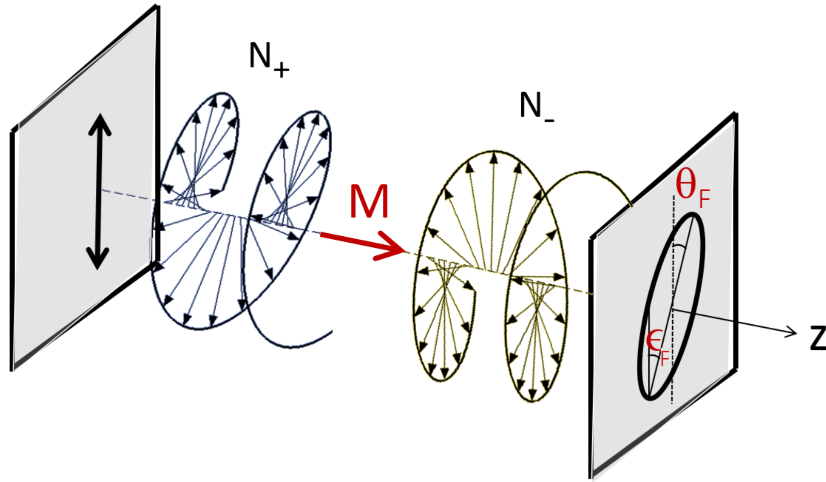

Fig. 2.2: Faraday effect. The proper modes of the left and right circular polarizations are indicated together with Faraday rotation and ellipticity arising from circular magnetic birefringence and dichroism.

A linearly polarised light entering the crystal can be considered as a superposition of left and right circularly polarised contributions as indicated in Fig 2.2. The difference in their dispersion values results in a rotation of the polarisation plane of the linearly polarised wave as it propagates through the crystal. The rotation angle per unit thickness, known as Faraday rotation or MCB, is equal to

$$\theta_F = \frac{\pi}{\lambda}\Re(N_+ - N_-) = \frac{\pi}{\lambda}\frac{K'' M_3}{\bar{N}}\,, \tag{2.55}$$

where $\bar{N} = (N_+ + N_-)/2$ and moderate absorption $\Re\bar{N} \gg \Im\bar{N}$ is assumed. On the other hand, the difference in absorption (MCD) induce an ellipticity in the polarization of the propagating wave that is given per unit thickness as

$$\chi = (\alpha_+ - \alpha_-)/4 = \frac{\pi}{\lambda}\Im(N_+ - N_-) = \frac{\pi}{\lambda}\frac{K'M_3}{\bar{N}}\,, \tag{2.56}$$

where $\alpha_+(\alpha_-)$ is the absorption coefficient for right circularly polarized (left circularly polarized) wave. Faraday ellipticity ϵ_F then relates to MCD by relation [30]

$$\tan\epsilon_F = \mathrm{tgh}\left[\frac{1}{4}(\alpha_+ - \alpha_-)\right]\,. \tag{2.57}$$

It is worth noting the non–reciprocity of the Faraday effect that is due to braking time-reversal symmetry of the system by virtue of magnetic field (cf. note in Section 2.2.2). This non–reciprocity manifests itself when the light travels back in magneto–optical medium, tracking the original path. Then, the Faraday rotation and ellipticity do not compensate but instead continuously increase their values. This phenomenon, fundamentally different from the chiroptical effects of optically active media, finds numerous applications, for example, in optical circulators, isolators, and rotators [21]. The key performance parameter of these devices, so–called figure of merit, is the ratio of the Faraday rotation and optical absorption. Materials possessing high values of the figure of merit in the specific spectral region are constantly searched (refer, for example, to Ref. [31]).

Voigt effect - linear magnetic birefringence and dichroism

Similarly, as it was done in the previous paragraph for the Faraday configuration, we can get proper modes for the light propagating perpendicularly to magnetization vector $\boldsymbol{M}$. These are linearly polarized waves with polarisation parallel or normal to magnetization vector and encountering refractive indices $N_\parallel$ and $N_\perp$, respectively. Therefore, if a linearly polarised wave with polarization vector at 45° to $\boldsymbol{M}$ enters the crystal, it will experience the birefringence and dichroism (cf. Fig 2.3). The former one is due to the difference in their dispersions and is called Voigt or Cotton–Mouton effect or magnetic linear birefringence

$$\beta = \frac{2\pi}{\lambda}\Re(N_\parallel - N_\perp)\,, \tag{2.58}$$

whereas the latter one is due to difference in their absorptions and is called magnetic linear dichroism

$$(\alpha_\parallel - \alpha_\perp) = \frac{4\pi}{\lambda}\Im(N_\parallel - N_\perp)\,. \tag{2.59}$$

In contrast to the Faraday configuration, rotation of the polarization plane, as the wave propagates, relates here to the dichroism and not to the birefringence. For small values of the MLD the rotation of the polarization direction is expressed by an angle

$$\theta = \frac{(\alpha_\parallel - \alpha_\perp)}{4}\,. \tag{2.60}$$

Explicit expressions for MLB and MLD depend on the orientation of magnetization vector $\boldsymbol{M}$ with respect to the crystallographic axis. When $\boldsymbol{M}$ is parallel to [100] direction we get

$$\Re(N_{\|} - N_{\perp}) = (G'_{11} - G'_{12})M^2/2\bar{N}\,, \tag{2.61}$$
$$\Im(N_{\|} - N_{\perp}) = (G''_{11} - G''_{12})M^2/2\bar{N}\,, \tag{2.62}$$

whereas when $\boldsymbol{M}$ is parallel to [111] direction we get

$$\Re(N_{\|} - N_{\perp}) = (G'_{44})M^2/\bar{N}\,, \tag{2.63}$$
$$\Im(N_{\|} - N_{\perp}) = (G''_{44})M^2/\bar{N}\,. \tag{2.64}$$

Here we have set $\bar{N} = (N_{\|} + N_{\perp})/2$. From the above relations it is clear that Voigt effect is quadraticly dependent on magnetisation and also sensitive on direction of vector $\boldsymbol{M}$ with respect to crystallographic axis, contrary to the Faraday effect that is on magnetization dependent linearly with no direction sensitivity in cubic crystals.

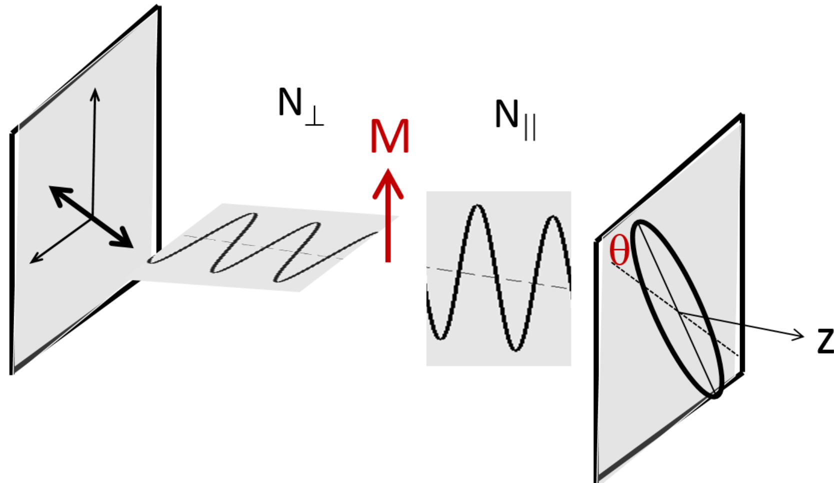

Fig. 2.3: Voigt effect. The proper modes of the mutually orthogonal linear polarizations are indicated together with azimuth rotation and ellipticity arising from linear magnetic dichroism and birefringence.

In the reflection, the analog effect to the Voigt effect is equally observable. Nevertheless, experimentally it is more difficult to access it as the normal incidence is required. More details about quadratic magneto-optical effects in reflection is provided in Section 4.3.3.

2.1.3 Dispersion and Kramers-Kronig relations

Electric displacement $\boldsymbol{D}(\boldsymbol{r}, t)$ at a position $\boldsymbol{r}$ and at a time t that appears in the constitutive relation (2.15) depends, in its general form, on the electric fields $\boldsymbol{E}(\boldsymbol{r'}, t')$

at all times $t' < t$ (temporal dispersion, taking into account the causality), and at any neighboring position $\boldsymbol{r'}$ (spatial dispersion). Considering this, Eq. (2.15) takes an integral form

$$\boldsymbol{D}(\boldsymbol{r},t) = \varepsilon_0 \int\int \varepsilon(\boldsymbol{r}-\boldsymbol{r'},t-t')\boldsymbol{E}(\boldsymbol{r'},t')\mathrm{d}\boldsymbol{r'}\mathrm{d}t' \,, \quad (2.65)$$

where the electric permittivity becomes a response function in space and time .

Fourier transform of Eq. (2.65) yields

$$\boldsymbol{D}(\boldsymbol{k},\omega) = \varepsilon_0\varepsilon(\boldsymbol{k},\omega)\boldsymbol{E}(\boldsymbol{k},\omega) \,, \quad (2.66)$$

where ω and $\boldsymbol{k}$ denote angular frequency and wavevector, respectively, of a monochromatic wave. The non-local behavior in both variables, space and time, manifests here by the permittivity dependence on the frequency ω and wavevector $\boldsymbol{k}$.

In optics, the space non–local response is usually ignored due to the fact that light wavelength is much longer than atomic scale where the optical processes in solids take place. That is also known as *long wavelength limit*. On the other hand, there is a class of solids for which this approximation does not hold. The particular example is an optically active medium that presents space non–local behavior due to the chirality. In this case, the wave vector dependence of the permittivity needs to be taken into account. Other examples are interfaces between different media and metallic objects with a size comparable to mean–free path of electrons [32]. In the long wavelength limit Eq. (2.66) simplifies to

$$\boldsymbol{D}(\omega) = \varepsilon_0\varepsilon(\omega)\boldsymbol{E}(\omega) \,. \quad (2.67)$$

The principle of causality establishes between the real and imaginary parts of the complex electric permittivity $\varepsilon(\omega)$ an inter–relations that are known as the dispersion relations (or Kramers–Kronig relations). In other words, the real and imaginary parts of electric permittivity are not independent, and one can be evaluated by the other. That also holds for other complex optical constants as, for example, electric susceptibility, refractive index, conductivity, etc.

Considering optically anisotropic or magneto–optical media where the electric permittivity has tensorial form, the Kramers–Kronig relations for each tensor element ε_{ij} become [33]

$$\Re\varepsilon_{ij}(\omega) - \delta_{ij} = \frac{2}{\pi}\wp\int_0^\infty \frac{\omega'\Im\varepsilon_{ij}(\omega')}{\omega'^2-\omega^2}d\omega' \,, \quad (2.68)$$

$$\Im\varepsilon_{ij}(\omega) - \frac{\sigma_{ij}(0)}{\varepsilon_0\omega} = -\frac{2\omega}{\pi}\wp\int_0^\infty \frac{\Re\varepsilon_{ij}(\omega')-\delta_{ij}}{\omega'^2-\omega^2}d\omega' \,. \quad (2.69)$$

In case of optically isotropic medium, the real refractive index n and extinction coefficient κ are Kramers-Kronig related by

$$n(\omega) - 1 = \frac{2}{\pi}\wp\int_0^\infty \frac{\omega'\kappa(\omega')}{\omega'^2-\omega^2}d\omega' \,, \quad (2.70)$$

$$\kappa(\omega) = -\frac{2\omega}{\pi}\wp\int_0^\infty \frac{n(\omega')-1}{\omega'^2-\omega^2}d\omega' \,. \quad (2.71)$$

Similar relations can be derived also for differences of refractive indices ($N_+ - N_-$) of left and right circular polarizations in Faraday configuration or for differences of refractive indices ($N_\parallel - N_\perp$) of parallel and perpendicular linear polarizations in Voigt configuration [33] (cf. Section 2.1.2). Kramers–Kronig relations applied to normal reflectivity enables the determination of complex optical constants of bulk samples although only one real quantity (reflectivity) is recorded. This is demonstrated for the case of PZT in Section 3.3.3. It is also worth noting that Kramers–Kronig relations are frequently employed in ellipsometry, where they are used for calculation of real part of permittivity of a given material, for which solely imaginary part was approximated by an analytic function (for example, Tauc–Lorentz parameterization, cf. Section 3.4.1). Last but not least, we note that Kramers-Kronig relations are an important verification of the causality consistency of real and imaginary parts of determined optical or magneto–optical constants.

2.2 Microscopic approach

The macroscopic electric and magnetic fields, together with charge and current densities, treated so far, are averaged quantities of their microscopic counterparts. Averaging is performed over a volume ΔV having linear dimensions of tens of nanometers. Such dimensions are small compared to the light wavelength but sufficiently large with respect to atomic dimensions. For example, the macroscopic charge density ρ is related with microscopic charge density ρ_{micro} by the relation:

$$\rho = \frac{1}{\Delta V} \int_{\Delta V} \rho_{micro}(\boldsymbol{r} + \boldsymbol{r'}) \mathrm{d}^3 \boldsymbol{r'} \,. \tag{2.72}$$

The microscopic quantities ρ_{micro} and $\boldsymbol{j}_{micro}$ are obtained by summing contributions from the individual electrons and atomic nuclei (in classical models) or from the electronic wavefunctions of the system (in quantum mechanical models). The fundamental classical and quantum mechanical microscopic models are outlined in the following sections focusing on optical and magneto–optical properties of solids. The concept of ab–initio calculations is introduced as well.

2.2.1 Optical constants

Lorentz and Drude theoretically predicted spectral dependencies of complex dielectric function $\varepsilon(\omega)$ of different solids including metals, semiconductors, and insulators (for a review refer, for example, to Refs. [18, 34, 19, 35, 36]). These classical theories that provide an insight into the correlation of microscopic behavior of electrons in solids with their optical properties are based on classical mechanics and electrodynamics.

The Lorentz oscillator model [37] of an elastically bound electron in the oscillating electric field is based on the equation of motion

$$m_e \frac{d^2 x}{dt^2} = -m_e \gamma \frac{dx}{dt} - m_e \omega_0^2 x - e E_0 e^{(i\omega t)}, \tag{2.73}$$

where m_e and $-e$ are mass and charge of an electron, respectively. The displacement x of the electron from a nucleus with infinite mass and charge $+e$ is driven by the force $-eE_0e^{(i\omega t)}$ generated by microscopic electric field [5] of an electromagnetic wave with frequency ω. The second term on the right side of Eq. (2.73) is a Hooke restoring force with resonant oscillator frequency ω_0. The first term stands for viscous–like damping with a frictional constant γ representing energy dissipation through interaction with neighboring atoms. Solution of this equation is complex charge displacement $x(\omega)$ that can be correlated with atomic electric dipole moment $\boldsymbol{p}(\omega)$ and further with macroscopic polarization density $\boldsymbol{P}(\omega)$. Finally, the electric permittivity leads to

$$\varepsilon_{Lorentz}(\omega) = 1 + \frac{e^2}{\varepsilon_0 m} \frac{N}{(\omega_0^2 - \omega^2) + i\gamma\omega}\,, \tag{2.74}$$

where N is the number of identical atoms per unit volume (number of oscillators). The Lorentz oscillator model of elastically bound electrons is mainly applicable to inter-band electronic transitions in semiconductors and insulators but it reasonably well describes also excitation of surface plasmons (for example, on metallic discontinuous thin films in an early stage of deposition before the percolation limit is reached [38, 39]). Composite bulk materials consisting of metallic particles embedded within an insulator matrix show Lorentz dispersion and absorption characteristics as well [12]. Moreover, the vibration of ions in ionic crystals, amorphous glasses, and polymers that gives contribution to $\varepsilon(\omega)$ in the infrared range can be also described by the Lorentz oscillators [40].

On the other hand, the Drude model is designed for the free (id est, not bounded) electrons in metals. This yields electric permittivity relation in the form

$$\varepsilon_{Drude}(\omega) = 1 - \frac{Ne^2}{\varepsilon_0 m} \frac{1}{(\omega^2 - i\gamma\omega)}\,, \tag{2.75}$$

with zero resonant frequency ω_0. It is noteworthy that the intra–band transitions, realized by photon absorption by free charge carriers in metals or doped semiconductors, can, thus, indirectly provide the carrier concentration N in a complementary way to electric transport measurements (refer, for example, to [41] or [42]).

But as most metals and equally heavily doped semiconductors or insulators exhibit contributions of both bond and free electrons within the same frequency range, electric permittivity $\varepsilon(\omega)$ contains, in general, Lorentz and Drude terms simultaneously (see for example [43])

$$\varepsilon = \varepsilon_{Drude} + \sum_n \varepsilon_{Lorentz}\,, \tag{2.76}$$

where the summation of the Lorentz contributions is effectuated over all spectrum–relevant bond electrons with different oscillation frequencies. This relation represents the most general form of the dispersion equations presented so far as they can be applied to metallic, semiconductor, and insulating material and are the starting points from which one can model optical spectra of solids.

[5] spatially averaged over the electron cloud

The classical models (Lorentz and Drude) have quantum mechanical analogs that lead to the same mathematical expressions for dielectric functions, but with the reinterpretation of the parameters

$$N \longrightarrow Nf_0, \quad \text{where} \quad f_0 = \frac{2m\omega_0}{\hbar}|x_0|^2 . \tag{2.77}$$

Thus, the concentration of bound electrons N is associated with the product of the atomic concentration and the oscillator strength f_0. The resonance frequency ω_0 simulates the frequency $\omega_0 = \frac{(E_n - E_0)}{\hbar}$ connecting the ground (0) and excited (n) states. The frictional constant γ is inversely proportional to the lifetime of the transition from state ϕ_0 to ϕ_n, and x_0 is the dipole matrix element

$$x_0 = \langle \phi_0 | x | \phi_n \rangle . \tag{2.78}$$

The influence of the optical electric field on the localized electronic wave function ϕ associated with each atom of the solid is treated in frame of first-order time-dependent perturbation theory. The dielectric function is then calculated from the wavefunction characteristics using quantum mechanical expressions for the complex polarization or the complex conduction current.

The Lorentz expression for the dielectric function can be extended to describe delocalized electrons in crystalline solids. Here, delocalized one-electron wave functions, or Bloch wave functions, are used. The dielectric function, in this case, depends explicitly on the joined density of electronic states in the crystal. There are approaches [44, 45], where parameterization of joined density of states, rather than the dielectric function, is employed for optical constants calculation, thus, providing a closer insight into the band structure of solids.

In crystalline solid, direct transitions that conserves the momentum of an electron in a crystal, neglecting the momentum of the absorbed photon, lead to different spectral behavior of absorption with respect to these encountered in indirect semiconductors where indirect electronic transitions are accompanied by the emission or absorption of phonon [46]. Therefore, examination of the onset of the absorption edge reveals not only material bandgap energy E_g but also the nature of the electronic transition (direct or indirect, allowed or forbidden). This knowledge is often important for material opto–electronic applications. The quantum mechanical analogy of the classical Drude free electron model exists, as well, and can be derived regarding light interaction with the free electrons as a quantum mechanical process. Here, intraband transitions involving electrons in the partially filled bands in metals and degenerate semiconductors are considered.

Actually, an accurate determination of materials optical constants is one of the main goals of ellipsometry, with fundamental and practical importance. Optical constants are, as already mentioned, the response function of a material to an electromagnetic wave and, apart from optical properties, they can indirectly reveal information about other (such as for example, mechanical, electrical, and structural) material properties, as well. The wider spectral range of optical constants is available, the deeper knowledge of material properties and their potential application is being gained. Figure 2.4 schematically shows

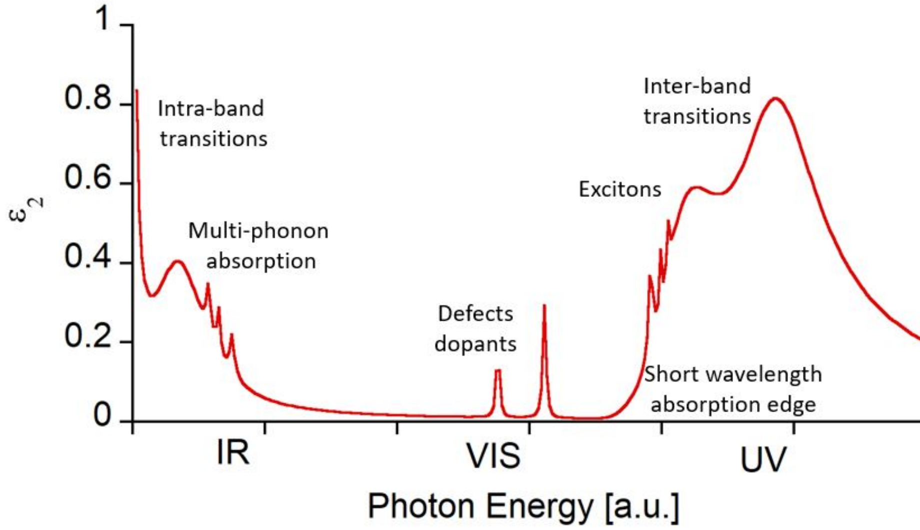

Fig. 2.4: Schematic spectral dependence of the imaginary part of the dielectric function $\varepsilon_2(\omega)$.

spectral dependence of imaginary part of electric permittivity $\varepsilon_2(\omega)$ of a material, where various types of light-matter interactions are indicated.

It is worth noting extrinsic and quantum confinement effects that can modify material optical constants. For example, dependency on temperature due to lattice parameter dilatation and electron—phonon interaction enables contactless optical monitoring of sample surface temperature. Application of this phenomenon is presented in Ref. [47] and later in Section 8.2. Other effects, as for instance, light [48], electron [49] or ion [Jagrova] beam irradiation or induced internal strain in a material [50] influence optical properties as well. In addition, the quantum confinement of materials is nowadays frequently used as an effective way for tuning their optical properties. As an example, we can mention transition metal dichalcogenides which in bulk form manifest behavior of indirect semiconductors but, when deposited or exfoliated in a form of ultrathin two–dimensional film (with a thickness of a few atomic monolayers), their electronic band structure gets modified transforming into direct bandgap material [51].

Last but not least, we should note the effect of external electric and magnetic fields (or magnetic ordering). The latter one has been already examined by introduction of the macroscopic magneto–optical constants. Its microscopic origin is briefly discussed in the following section.

2.2.2 Magneto-optical constants

The classical Lorentz model can be extended even for magneto-optical medium. That is done by taking into account an additional effect of the static magnetic field $\boldsymbol{B}$ on the electrons. In other words, by introducing additional force, magnetic Lorentz force $\boldsymbol{F} = e\boldsymbol{v} \times \boldsymbol{B}$, $\boldsymbol{v}$ being electron velocity, into the equation of electron motion (2.73).

Let's consider the Lorentz picture in Faraday experimental configuration where linearly polarised light propagates along a static magnetic field. In this case, induced electric polarization $\boldsymbol{P}$ is no more oscillating co-linearly with the light electric field, as is the case for optically isotropic medium, but, instead, contains an orthogonal component as well that is due to the magnetic Lorentz force. This is macroscopically manifested by the appearance of the off-diagonal permittivity tensor elements ε_{12} and ε_{21} (cf. Eq. (2.50)) and by rotation of light polarization as the wave propagates through the material. This was discussed in more detail earlier in this Section. Furthermore, since a magnetic field is involved, time–reversal symmetry must be treated with particular care. The reason is that the Lorentz force, which is involved in the interaction, is a vector product of particle velocity and the magnetic field, and therefore, one must reverse both particle velocities and the magnetic field to ensure the particles retrace their paths [33]. The consequence of this is already mentioned as the non-reciprocity of magneto–optical effect.

It can be shown that in the frame of the classical Lorentz model, the diagonal and off-diagonal permittivity tensor elements get the following spectral dependencies [33]

$$\varepsilon_{11} = \varepsilon_{22} = 1 + \frac{Ne^2}{m\varepsilon_0} \frac{\omega_0^2 - \omega^2 + i\gamma\omega}{(\omega_0^2 - \omega^2 + i\gamma\omega)^2 - \omega_c^2\omega^2}\,, \tag{2.79}$$

$$\varepsilon_{33} = 1 + \frac{Ne^2}{m\varepsilon_0} \frac{1}{\omega_0^2 - \omega^2 + i\gamma\omega}\,, \tag{2.80}$$

$$\varepsilon_{12} = -\varepsilon_{12} = \frac{Ne^2}{m\varepsilon_0} \frac{i\omega\omega_c}{(\omega_0^2 - \omega^2 + i\gamma\omega)^2 - \omega_c^2\omega^2}\,. \tag{2.81}$$

Note that ε_{33} is not affected by a magnetic field and is equal to the permittivity of optically isotropic medium (Eq. (2.74)). Nevertheless, other terms ε_{11}, ε_{22}, ε_{12} and ε_{21} depend on magnetic field through cyclotron frequency $\omega_c = -eB/m$. When magnetic fields disappear, the off–diagonal terms disappear as well, and the diagonal ones get identical and equal to the isotropic material. Although some authors (see, for example, Refs. [52, 53]) used the classical Lorenz model for estimation of magneto–optical constants of selected materials, generally, application of the quantum mechanical approach is necessary.

Quantum models relating interband electronic transitions with the magneto–optical effects were gradually developed from the 1930s. In 1932 Hulme [54] showed that the origin of significant magneto-optical activity in ferromagnetic materials is spin-orbit interaction. This interaction indirectly couples electron spins with light wave through electron orbital momentum. Later, Kittel [55] pointed out that the modification of electron wave functions due to spin-orbit interaction plays an important role as well. Afterward, Argyres [56] derived in 1955 relation of magneto-optical effects working on the perturbation theory and current density calculations. An alternative approach that stems from an elaboration of electron transition probabilities when magnetized matter interacts with circularly polarized light was done by Bennett and Stern [57], Pershan [15] and Kahn [58]. In this concept, right or left circularly polarised waves excite electrons which, in accordance with the law of angular momentum conservation, change the projection of their angular momentum by $\Delta m = \pm 1$. Off-diagonal elements of the dielectric permittivity in the electric

dipole approximation and consequently the Faraday effect is defined by the difference between the contributions of the 'right' and 'left' transitions (id. est., the transitions with $\Delta m = +1$ and $\Delta m = -1$). In non-magnetic materials at $H = 0$, these processes have become equalized, and therefore, no magneto-optical effects take place. In a magnetic field and magnetically ordered materials, the balance between the total contributions of the right and left processes to the permittivity is broken; this results in a rotation of the plane of polarization of light or in a difference between the absorption coefficients of the light with different circular polarizations.

Kahn showed that the off-diagonal tensor element ε_{12}, which is responsible for Faraday rotation and MCD, can be expressed in terms of the difference of right circular polarized (rcp) and left circular polarized (lcp) transition matrix elements. For an electronic dipole transition between a ground state and excited states, ε_{12} is given by

$$\varepsilon_{12} = \frac{2\pi N e^2}{m} \sum_{e,v} \frac{f_{+e(v)} - f_{-e(v)}}{\omega^2 - \omega_{e(v)}^2 - \gamma_{e(v)}^2 - i\gamma_{e(v)}} \frac{\omega - i\gamma_{e(v)}}{\omega_{e(v)}}, \tag{2.82}$$

where

$$f_{\pm e(v)} = \frac{m\omega_{e(v)}}{\hbar} \langle g | x \pm \mathrm{i} y | e(v) \rangle^2$$

are the oscillator strengths for rcp and lcp transitions, resp., N is the number of spins, $\omega_{e(v)}$ is the transition frequency to the excited state $|e(v)\rangle$, where v numbers the sublevels of $|e\rangle$ which are split by spin-orbit coupling and exchange.

As mentioned above, the dominant contribution to the Faraday rotation results from spin-orbit splitting of excited states. In a magnetic crystal, the exchange splitting far exceeds the Zeeman splitting of the energy levels. However, the exchange acts only on the spin levels, not on the orbitals, and therefore, cannot give rise to magneto–optical effects. It is only the spin-orbit coupling that allows the orbitals to sense the polarization of rcp and lcp waves via the selection rules for electronic transitions [20].

Analogously to the optical constants, also in a static magnetic field, the classical Lorenz model of the elastically bound electron, Eqs. (2.79)–(2.81), transforms to the Drude formula of free electrons when the resonant frequency gets zero value. It can be shown that quantum mechanical calculations of the light interacting with the free electrons yield in the high frequency limit the same dispersion relation as its classical counterpart, except for non-classical spin–orbit–induced polarization [59].

2.3 Ab-initio calculations

Complex electric permittivity, $\varepsilon(\omega)$, characterizing optical and magneto-optical interactions in solids can be calculated also from the first principles, id est, ab–initio. The Schrodinger equation with many–electron Hamiltonian of interacting electrons moving in the field of the nucleus and external magnetic field cannot be solved exactly to get closed–form expression for energy eigenvalues and eigenvectors. However, two relatively simple approximations exist for obtaining a qualitative picture of the multielectron wavefunctions: Hartree–Fock method [60] and Thomas Fermi theory [61, 62]. The latter, an

approximate method for finding the electronic structure of complex systems (including solids) using the one–electron ground state density, $\rho(\boldsymbol{r})$, is much easier to implement and therefore was intensively developed. The modern version of this approach is Kohn-Sham density functional theory, which defines self-consistent equations that must be solved for a set of orbitals whose density, $\rho(\boldsymbol{r})$, is defined to be exactly that of the real system. The simplest approximation of the exchange correlation energy (given in terms of $\rho(\boldsymbol{r})$) is the local density approximation (LDA) [63] which became the popular standard in calculation on solids in the 1970s and 1980s.

To study magnetic effects including magneto–optical phenomena, one needs access to quantities such as spin and orbital moments. The most suitable for these calculations turned out to be the spin density functional theory [64, 65] combined with relativistic Kohn-Sham equations, so–called local spin density approximation (LSDA). Macroscopic conductivity, $\sigma(\omega)$, that is the preferred quantity with respect to dielectric permittivity, in the theoretical calculations is derived from Kubo formula [66]. It is worth mentioning here that for the successful calculation of optical and magneto-optical effects one needs a precise solution of not only the ground state of the system that is usually well described, but also of the excited states, that were a long time, and still remains, a challenge for calculation.

The first success in ab-initio calculation can be considered the determination of the conductivity tensor of ferromagnetic Ni by Wang and Callaway in 1974 [67]. Other works followed with increasing theoretical reliability with respect to experimentally obtained data (see, for example, Oppeneer [68], and Kunes [69, 70]). Ab-initio calculations can

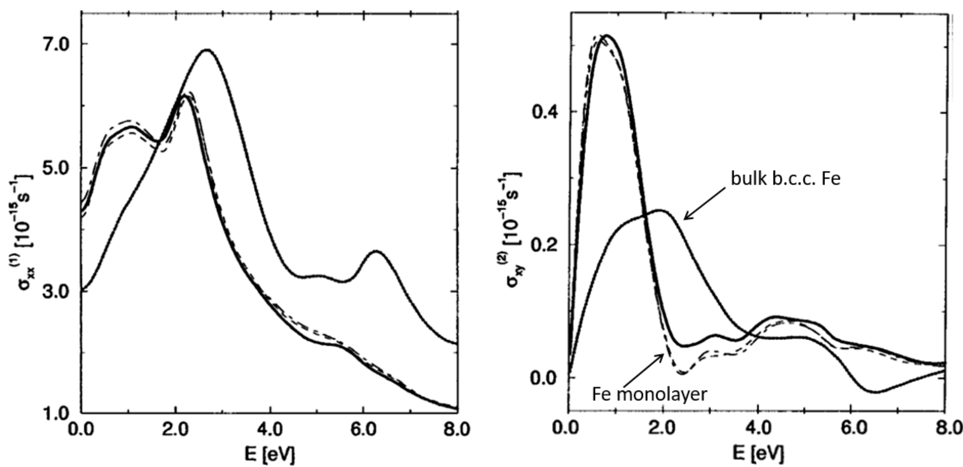

Fig. 2.5: Real part of the diagonal (left) and imaginary part of off–diagonam (right) element of the conductivity tensor calculated for bulk Fe (solid line) and Fe monolayer (broken line). Modified from Kuneš and Mistrík [71].

be relatively easily extended also for low dimensional systems, which are promising in modern applications. As an example, we refer to Fig. 2.5 and paper by Kunes and Mistrik [71] where optical and magneto-optical constants are calculated for mono-atomic Fe and compared with bulk b.c.c. Fe.

Chapter 3

Ellipsometry

3.1 Measurable quantities

Ellipsometry measures the polarization change in light induced by its non–normal reflection from a sample surface. This change is often expressed as the ratio of the reflection coefficients. For oblique incidence, we distinguish s– and p– waves. The s–wave is linearly polarized with the vector of the electric field $\boldsymbol{E}$ perpendicular to the plane of incidence, whereas the p– wave is linearly polarized with the vector $\boldsymbol{E}$ parallel to the plane of incidence. Measurable quantities for isotropic and anisotropic samples will be treated separately.

3.1.1 Isotropic case

When the s– and p– waves are reflected from an optically isotropic sample, they remain s– and p–polarized, respectively, but their amplitude and phase are changed due to light interaction with the sample (cf. Figure 3.1). These changes are expressed by the reflection coefficients r_s and r_p, which are defined as the ratio of the complex amplitudes of the reflected $\hat{E}^r$ and incident $\hat{E}^i$ waves at the same point on the sample surface. For p– and s– waves we get

$$r_p \equiv \frac{\hat{E}_p^r}{\hat{E}_p^i} = \frac{E_{0p}^r \, e^{i\delta_p^r}}{E_{0p}^i \, e^{i\delta_p^i}} , \tag{3.1}$$

$$r_s \equiv \frac{\hat{E}_s^r}{\hat{E}_s^i} = \frac{E_{0s}^r \, e^{i\delta_s^r}}{E_{0s}^i \, e^{i\delta_s^i}} . \tag{3.2}$$

Change of the polarization is in isotropic case conveniently expressed by the ratio of the reflection coefficients r_p and r_s. This complex number is usually further rewritten in terms of ellipsometric parameters Ψ and Δ

$$\frac{r_p}{r_s} \equiv \tan \Psi e^{i\Delta} . \tag{3.3}$$

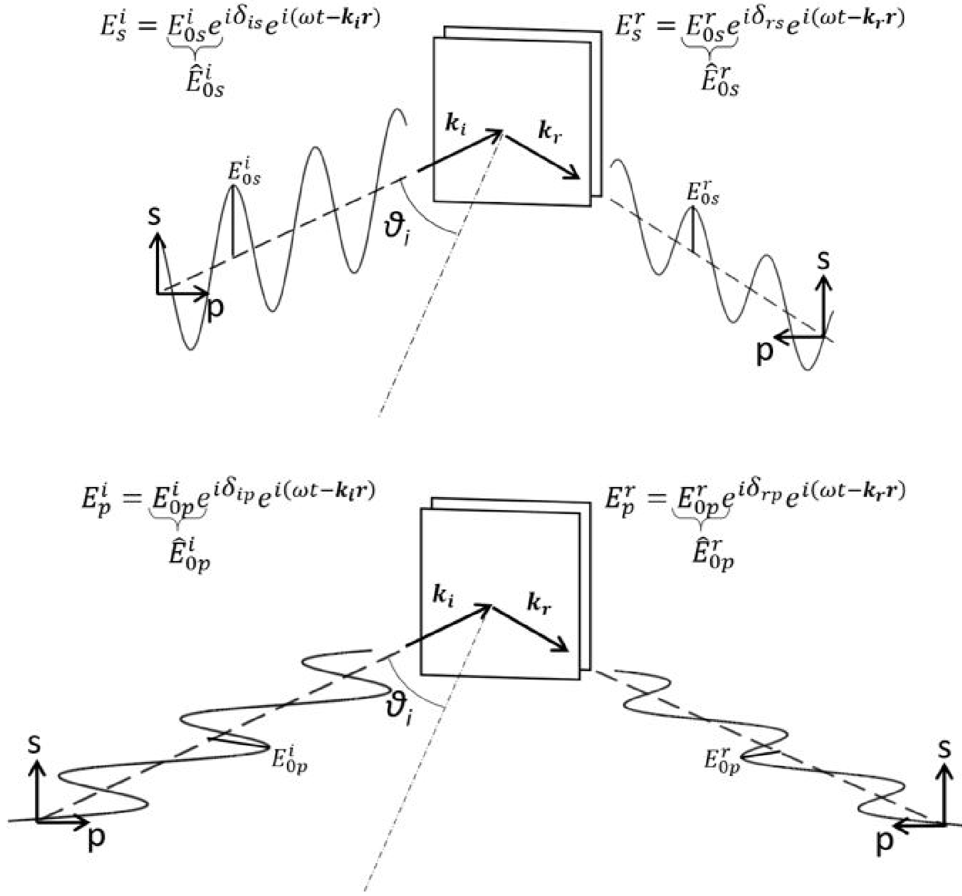

Fig. 3.1: S– and p–polarised waves reflected from an optically isotropic sample.

The geometric meaning of the introduced ellipsometric angles Ψ and Δ is worth discussing. Consider an incident light with equal components of s– and p– waves that are in phase. In other words, the incident light is linearly polarized with the electric vector $\boldsymbol{E}$ oscillating at an angle 45° to the incidence plane (cf. Figure 3.2). When the light gets reflected from the sample surface, the s– and p– components change their amplitudes and phases, and, as a result, the reflected wave becomes elliptically polarized, in general. It can be shown that parameters of this elliptical polarization[1] relates to the ratio $\frac{r_p}{r_s}$ because

$$\frac{r_p}{r_s} = \frac{\frac{E_{0p}^r \, e^{i\delta_p^r}}{E_{0p}^i \, e^{i\delta_p^i}}}{\frac{E_{0s}^r \, e^{i\delta_s^r}}{E_{0s}^i \, e^{i\delta_s^i}}} = \frac{E_{0p}^r}{E_{0s}^r} e^{i(\delta_p^r - \delta_s^r)} \, . \tag{3.4}$$

[1]Parameters α and δ defined in Tab. 1.1.

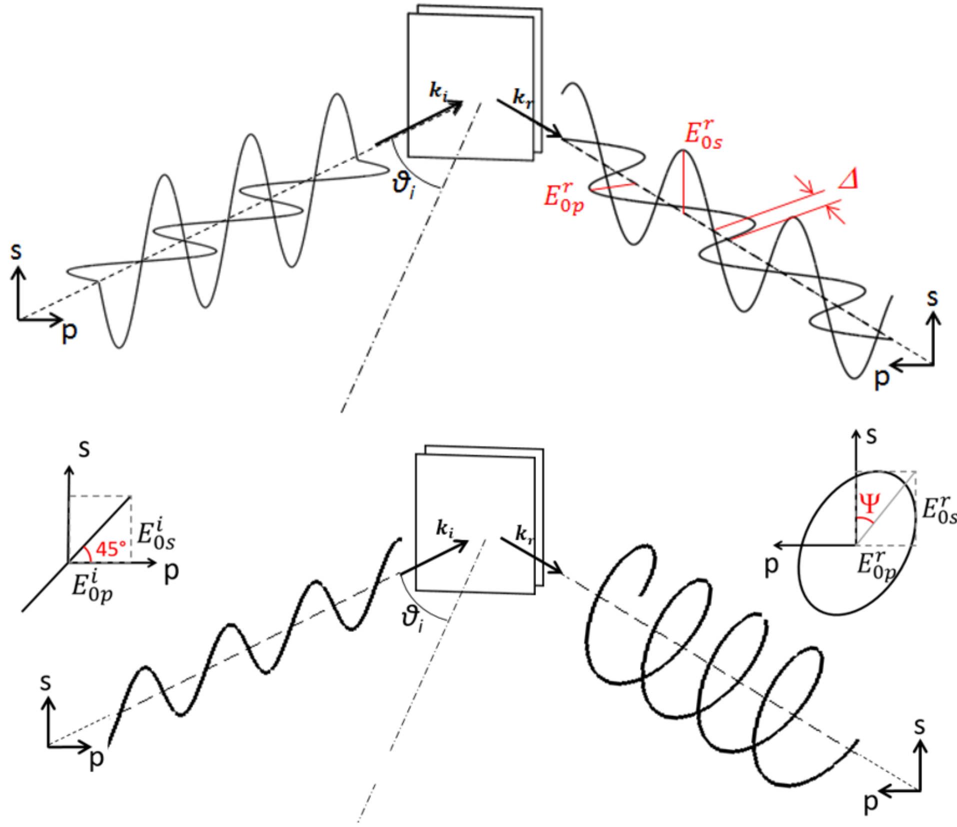

Fig. 3.2: Geometrical meaning of the ellipsometric parameters Ψ and Δ.

And with help of Eq. (3.3) we get ellipsometric relations

$$\tan\Psi = \frac{E^r_{0p}}{E^r_{0s}}, \tag{3.5}$$

$$\Delta = \delta^r_p - \delta^r_s . \tag{3.6}$$

Accordingly, Eq. (3.3) determines, through the ellipsometric parameters Ψ and Δ, changes in amplitudes and phases of the s– and p– waves in their reflection from the sample surface (cf. Figure 3.2). It is noteworthy that the phase change of the reflected p– or s– wave is, in general, difficult to measure independently, but its relative change $\delta_p - \delta_s$ is accessible when polarization measurements are considered. Therefore, ellipsometry belongs to the group of phase–sensitive techniques, which is rather susceptible to surface properties. On the other hand, photometric measurements such as, for example, reflectance measurement[2] (which is usually easy to perform), access only the absolute value of the reflection coefficient as

$$R_{s,p} = |r_{s,p}|^2 , \tag{3.7}$$

but one cannot detect its phase. Reflection coefficients r_p and r_s can be theoretically calculated for various samples, including bulks, single and multilayers, linear gratings, or

[2]Defined as the ratio of reflected I^r and incident I^i light intensities $R \equiv \frac{I^r}{I^i}$.

photonic crystals. It is evident that both the sample inner structure (to the depth that light reaches by its penetration under the surface) and the optical constants of materials involved in the interaction influence the reflection coefficients. Therefore, experimentally determined ellipsometric parameters can provide information on sample geometry and its optical properties in the spectral range under consideration. In fact, this is the general goal of ellipsometric characterization.

3.1.2 Anisotropic case

So far, we have discussed optically isotropic samples, where the s– and p– polarizations are proper modes, and they do not mutually interchange when reflecting from a sample surface. However, the situation is more complex when reflection from optically anisotropic samples are considered. In this case, not only the r_{ss} and r_{pp} reflection coefficients [3] but also r_{sp} and r_{ps} (that represent mixing of s– and p– waves) have to be taken into account. These are defined as follows

$$r_{ss} \equiv \left(\frac{\hat{E}_s^r}{\hat{E}_s^i}\right)_{\hat{E}_p^i=0} = \frac{E_{0s}^r\, e^{i\delta_s^r}}{E_{0s}^i\, e^{i\delta_s^i}}\,, \tag{3.8}$$

$$r_{pp} \equiv \left(\frac{\hat{E}_p^r}{\hat{E}_p^i}\right)_{\hat{E}_s^i=0} = \frac{E_{0p}^r\, e^{i\delta_p^r}}{E_{0p}^i\, e^{i\delta_p^i}}\,, \tag{3.9}$$

$$r_{sp} \equiv \left(\frac{\hat{E}_s^r}{\hat{E}_p^i}\right)_{\hat{E}_s^i=0} = \frac{E_{0s}^r\, e^{i\delta_s^r}}{E_{0p}^i\, e^{i\delta_p^i}}\,, \tag{3.10}$$

$$r_{ps} \equiv \left(\frac{\hat{E}_p^r}{\hat{E}_s^i}\right)_{\hat{E}_p^i=0} = \frac{E_{0p}^r\, e^{i\delta_p^r}}{E_{0s}^i\, e^{i\delta_s^i}}\,. \tag{3.11}$$

In the frame of the Jones formalism, reflection from a sample is described by Fresnel reflection matrix R [1]. For optically isotropic samples it takes the diagonal form (with r_s and r_p on the diagonal) whereas, in the case of anisotropic samples, all its elements are generally non-zero

$$R = \begin{bmatrix} r_{ss} & r_{sp} \\ r_{ps} & r_{pp} \end{bmatrix}\,. \tag{3.12}$$

Polarisation states of the reflected wave (expressed in the form of Jones vector[4]) is then calculated by multiplication of the reflection matrix with the Jones vector of the incident wave

$$\begin{bmatrix} \hat{E}_s^r \\ \hat{E}_p^r \end{bmatrix} = \begin{bmatrix} r_{ss} & r_{sp} \\ r_{ps} & r_{pp} \end{bmatrix} \begin{bmatrix} \hat{E}_s^i \\ \hat{E}_p^i \end{bmatrix}\,. \tag{3.13}$$

[3] In isotropic case r_{ss} (r_{pp}) was referred as r_s (r_p).

[4] Column vector of wave complex amplitudes in the base of s– and p– polarizations with its magnitude normalized to unity [1].

As the Jones vectors are normalized, it is convenient to normalize reflectin matrix R as well. That is usually done by division of all its elements by r_{ss} coefficient. Hence, for anisotropic samples, we define six independent ellipsometric parameters $[\Psi_{pp}, \Delta_{pp}]$, $[\Psi_{ps}, \Delta_{ps}]$ and $[\Psi_{sp}, \Delta_{sp}]$ defined by the following relations

$$\frac{r_{pp}}{r_{ss}} \equiv \tan \Psi_{pp} e^{i\Delta_{pp}} , \quad (3.14)$$

$$\frac{r_{ps}}{r_{ss}} \equiv \tan \Psi_{ps} e^{i\Delta_{ps}} , \quad (3.15)$$

$$\frac{r_{sp}}{r_{ss}} \equiv \tan \Psi_{sp} e^{i\Delta_{sp}} . \quad (3.16)$$

Some authors prefer to replace relation (3.16) by

$$\frac{r_{sp}}{r_{pp}} \equiv \tan \Psi_{sp} e^{i\Delta_{sp}} , \quad (3.17)$$

because it is more convenient for description of rotating analyser ellipsometrers [72]. Furthermore, as we will see in Section 4.1, relation (3.17) is consistent with definition of magneto–optical parameters that will be introduced later in the next Chapter. Ellipsometric characterization of anisotropic samples is also known as *generalised ellipsometry* (for more details refer for example to [73] and references therein).

Geometrical meaning of the angles $[\Psi_{ps}, \Delta_{ps}]$ arise from the definition relations Eqs. (3.8, 3.11, and 3.15)

$$\frac{r_{ps}}{r_{ss}} = \frac{\frac{E^r_{0p}\, e^{i\delta^r_p}}{E^i_{0s}\, e^{i\delta^i_s}}}{\frac{E^r_{0s}\, e^{i\delta^r_s}}{E^i_{0s}\, e^{i\delta^i_s}}} = \frac{E^r_{0p}}{E^r_{0s}} e^{i(\delta^r_p - \delta^r_s)} = \tan \Psi_{ps} e^{i\Delta_{ps}} . \quad (3.18)$$

Therefore, if s–polarised light is incident the reflected wave becomes elliptically polarised with parameters $\alpha = \Psi_{ps}$ and $\delta = \Delta_{ps}$. Analogously, for p–polarised incident wave and considering relation (3.17), parameters Ψ_{sp} and Δ_{sp} can be regarded as α and δ parameters of reflected wave, respectively. On the other hand, in case of weak optical anisotropy, it is advantageous to express the reflection ratios $\frac{r_{ps}}{r_{ss}}$ and $\frac{r_{ps}}{r_{pp}}$ by the azimuth θ and the angle of ellipticity ϵ of the reflected wave as it is common in magneto–optics, Eqs. (4.3)–(4.5), or in chiroptical spectroscopy. To provide an example, refer to an optical anisotropy study of $YAlO_3 : Nd$ [74].

3.2 Instrumentation

Various aspects of instrumentation in ellipsometry are discussed in detail in monographs and handbooks (see, e.g., Refs. [75, 35, 76]). Historically, the first developed ellipsometers were null ellipsometers, where light first propagates through a polarizer and compensator and then gets reflected from the sample toward the analyzer and detector

as schematically shown in Figure 3.3. In this experimental configuration, the orientation of the polarizer and compensator is adjusted in such a way that light reflected from the sample is linearly polarized. The analyzer is then rotated to the position where the light intensity on the detector gets extinguished or "nulled."

The schematic experimental setup of null ellipsometry is shown in Figure 3.3, where the polarizer and analyzer can be rotated. The compensator is a quarter-wave plate with fast and slow axes oriented $\pm 45°$ with respect to the plane of incidence. It can be shown that when the light wave, transmitted through the polarizer and compensator, is incident on the sample surface, it has both s– and p– components of equal amplitudes but mutually shifted in phase by an angle $2P$ (P being the angle of polarizer, indicated in red in Figure 3.3). Hence, when the phase shift of the s– and p– components of the wave incident on the sample is compensated by the reflection, then the reflected wave is linearly polarized and can be extinguished by the analyzer (A being the angle of the analyzer). From the positions of the polarizer and the analyzer, the ellipsometric angles Ψ and Δ can be calculated by [77]

$$\Psi = A\,, \tag{3.19}$$

$$\Delta = 2\left(P - \frac{\pi}{4}\right)\,. \tag{3.20}$$

This configuration in Figure 3.3, if performed in four equivalent quadrants, is very accurate due to the compensation of systematic errors. However, even when automated, this approach is relatively slow, and measurements are time-consuming.

In order to speed up the measurements, ellipsometers with rotating analyzer, polarizer, or compensator were developed. In these systems, either the analyzer, polarizer,

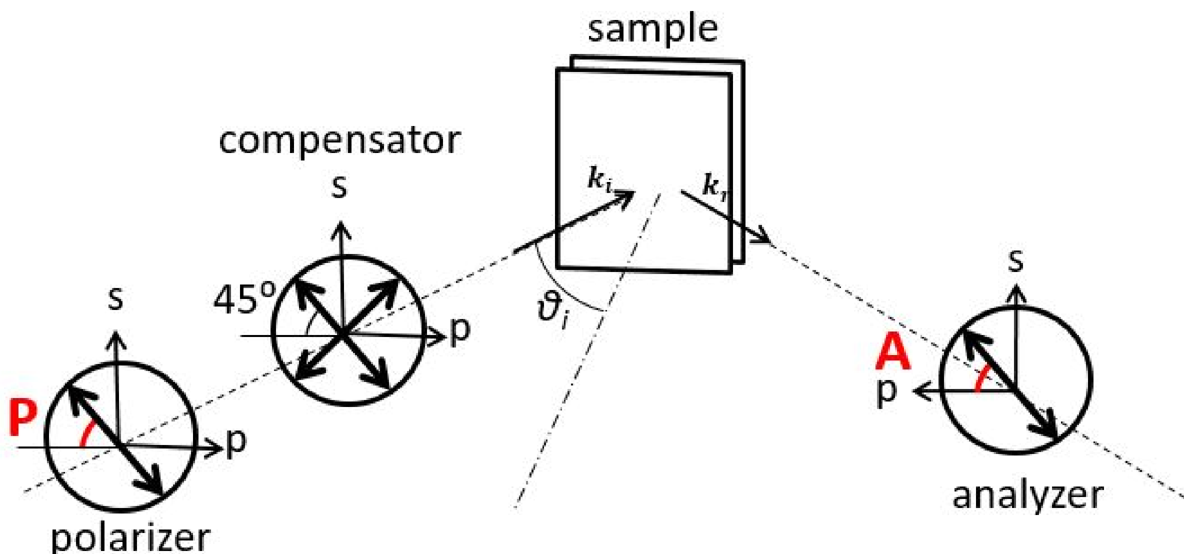

Fig. 3.3: Schematic experimental setup of null ellipsometry.

or compensator is continuously rotated at a constant angular velocity (typically about 10–100 Hz) to modulate the light polarization state. Alternatively, one can also use a photoelastic modulator, which generates a periodically changing light intensity in the detector. Fourier analysis of the corresponding detector signal then provides the ellipsometric values Ψ and Δ. Such systems can ensure high–speed and accurate measurements. Nevertheless, it is noteworthy that each of the above–mentioned ellipsometers has both strengths and weaknesses depending on its specific configuration [73].

Further significant improvements in ellipsometers have extended the concepts developed for measurements at a single wavelength to measurements at multiple wavelengths. Spectroscopic ellipsometers capable of measuring the ellipsometric angles Ψ and Δ as a function of the wavelength have added another dimension to the analysis, permitting more reliable determination of material and structural parameters. Presently, a broad spectral range spanning the terahertz, far infrared, mid-infrared, near-infrared, visible, ultraviolet (UV, DUV, and VUV) can be by parts covered by various commercial ellipsometers. Furthermore, fast in-situ ellipsometers with charged coupled device detectors and imaging ellipsometers with a lateral resolution of about 1.0 μm are also commercially available.

3.3 Single interface

Here, we use the term single interface for a sharp and plane interface between two homogeneous media with different refractive indices. When an optical experiment is carried out, usually the ambient medium (with the incident and reflected beams) is air, and the other medium is the sample to be studied. The sample surface is then identical with the interface itself, as shown in Figure 3.4. Under real conditions, such a sample surface is never perfectly sharp and plane, but it can be often approximated by a single interface. The limitation of this approximation will be discussed later in this section.

We start the discussion with the optically isotropic samples and then proceed with anisotropic samples. Reflection coefficients and ellipsometric parameters can be in both cases derived by application of Maxwell's equations, where in the first step solution of the wave equation is searched in the ambient and sample material independently (as if they were infinite media). Subsequently, applying the boundary conditions of continuity of the tangential components of the electric and magnetic fields at the interface the reflection coefficients are obtained.

Further, we show how the ellipsometric parameters recorded on a single interface are employed to determine sample optical constants. Case studies with real samples are provided as well. The section is closed by spectro–photometric (non–ellipsometric) experimental techniques that are used for optical characterization of the single interface as well.

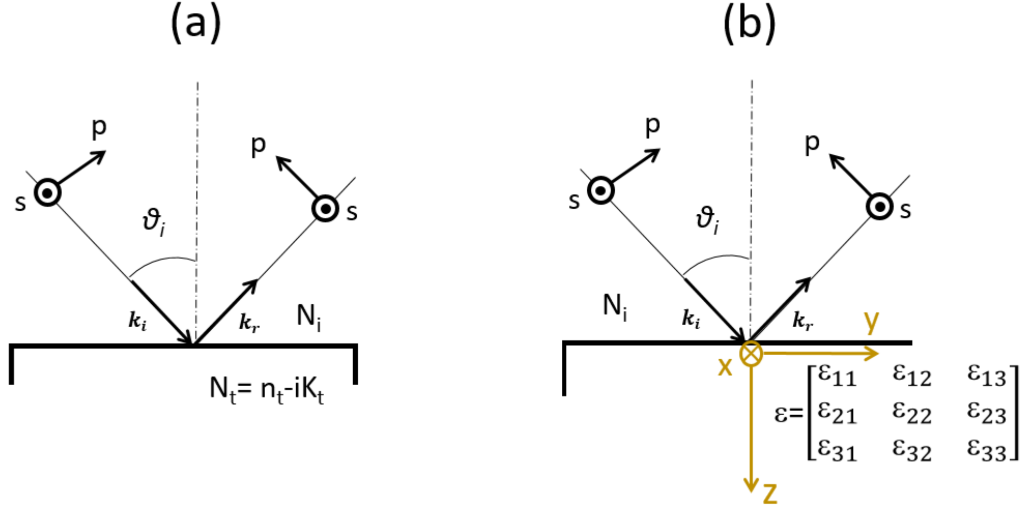

Fig. 3.4: Cartesian coordinate systems defined by the base vectors s and p of the incident and reflected waves. Optical properties of a sample are expressed for isotropic case by refractive index N_t, (a), and for anisotropic case by electric permittivity tensor ε, (b). Ambient refractive index is N_i.

3.3.1 Optically isotropic sample

Fresnel equations

In case of light reflection from an isotropic sample (cf. Fig. 3.4a) the reflection matrix is diagonal and only two reflection coefficients r_s and r_p are to be determined. These are given by the well–known Fresnel relations [16]

$$r_s = \frac{N_i \cos\theta_i - N_t \cos\theta_t}{N_i \cos\theta_i + N_t \cos\theta_t}, \tag{3.21}$$

$$r_p = \frac{N_t \cos\theta_i - N_i \cos\theta_t}{N_t \cos\theta_i + N_i \cos\theta_t}, \tag{3.22}$$

where N_i and N_t are complex refractive indices of the ambient and sample, respectively. The incidence and refraction angles, which are related by Snell's law, are denoted by θ_i and θ_t, respectively.

For further use, we provide here also the normal incidence Fresnel formula for the transmission coefficient (the ratio of the complex amplitudes of the transmitted and incident waves):

$$t = \frac{\hat{E}^t}{\hat{E}^i} = \frac{2N_i}{N_i + N_t}. \tag{3.23}$$

In the derivation of the Fresnel Eqs. (3.21) and (3.22), care should be exercised with respect to the coordinate system that one selects. In fact, this selection may influence the sign of the r_p coefficient [35]. Here, we consider two coordinate systems assigned to the

incident and reflected waves as indicated in Figure 3.4a. For normal incidence, the s base vectors of the incident and reflected waves coincide with each other, whereas the p base vectors are opposite in direction.

Brewster and Principal angles

Values of Fresnel reflection coefficients and ellipsometric parameters as well are dependent on the incidence angle. Given the forthcoming discussion of ellipsometric measurement strategy, it is useful to discuss it briefly and identify so-called Brewster and Principal angles. For this reason, it is convenient to express reflection coefficients in the form of their absolute values and their phases:

$$r_p = |r_p|e^{i\phi_p}\,, \tag{3.24}$$

$$r_s = |r_s|e^{i\phi_s}\,. \tag{3.25}$$

The definition of the ellipsometric angles Ψ and Δ by Eq. (3.3) can then be rewritten as

$$\frac{r_p}{r_s} = \left|\frac{r_p}{r_s}\right| e^{i(\phi_p-\phi_s)} = \tan\Psi e^{i\Delta} \tag{3.26}$$

and hence

$$\Psi = \arctan\left|\frac{r_p}{r_s}\right|, \tag{3.27}$$

$$\Delta = \phi_p - \phi_s\,. \tag{3.28}$$

Dependence of the Fresnel reflection coefficients r_s and r_p in Eqs. (3.21) and (3.22) on the angle of incidence is presented in Figure 3.5, where we have considered that the ambient is air (as it is often the case in a real experiment, therefore $N_i = 1$). Transparent sample with refractive index $n_t = 2.0$ and other three absorbing samples with same n_t but non–zero extinction coefficients: $\kappa_t = 0.2$, 0.8, and 1.5 are used in the modeling. The absolute value of the r_s coefficient, plotted in blue in Figure 3.5a, monotonously increases from normal incidence value (equal to $|r_p|$) up to incidence angle of 90°, where it reaches unity (together with $|r_p|$). However, the incidence angle dependence of the p reflection coefficient is not monotonous. Angle of incidence where r_p coefficient becomes zero is called the *Brewster angle* and is denoted by θ_B. Complete disappearance of p–polarized reflected beam occurs only in case of a transparent sample and can be explained by the radiation diagram of the electric dipole [35]. Accordingly, the Brewster angle is related to the ambient and sample refractive indices by relation

$$\theta_B = \arctan\frac{N_t}{N_i}\,. \tag{3.29}$$

Using Eq. (3.29) we obtain in our case $\theta_B = 63.4°$. For absorbing samples, the absolute value of the r_p coefficient, plotted in Figure 3.5a in red, does not reach a zero value. Instead, its angle dependence gives a non–zero minimum that shifts toward higher incidence

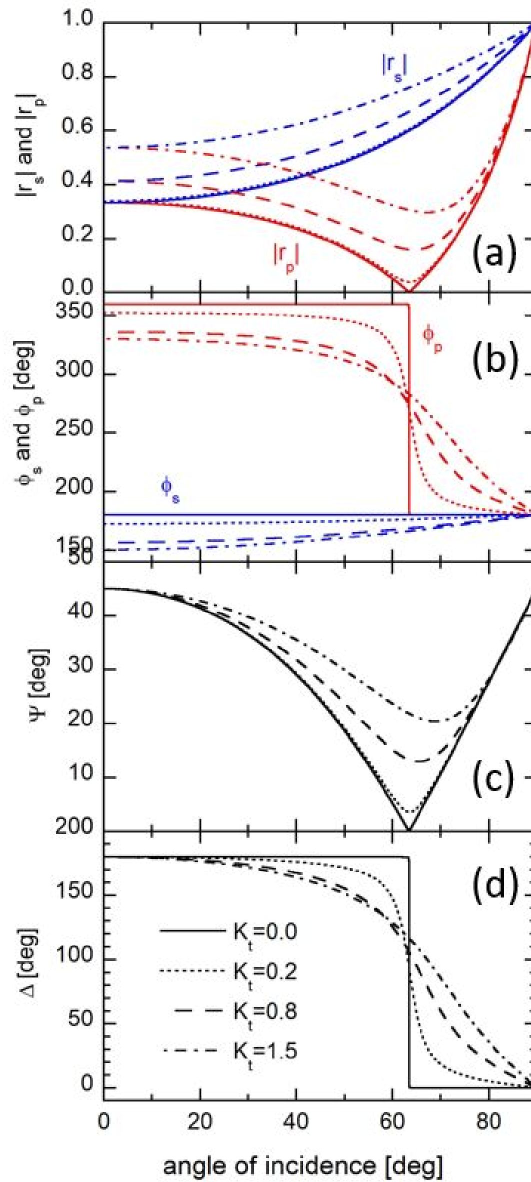

Fig. 3.5: Absolute values (a) and phases (b) of reflection coefficients together with ellipsometric parameters (c and d) as a function of the angle of incidence and extinction coefficient of the sample.

angles with increasing extinction. The position of this minimum is called *the Principal angle*.

The phase of the s–reflection coefficient (in blue in Figure 3.5b) is, for a transparent sample, the incident angle independent with a constant value of 180°. On the other hand, the phase of the p–reflection coefficient as shown in Figure 3.5b in red manifests an abrupt change (from 360° to 180°) when crossing the Brewster angle. The phase dependence on sample absorption is also presented in Figure 3.5b for the selected extinction coefficients.

Corresponding angle dependence of ellipsometry parameters Ψ and Δ are calculated from Eqs. (3.27) and (3.28) and plotted in Figure 3.5c,d, respectively. The signature of the Brewster (Principal) angle is manifested by a minimum in the Ψ parameter and by a step-like change in the Δ parameter.

Inverse analytical formula

It is worth noting that from the ellipsometric parameters Ψ and Δ, that are recorded on a single interface, we can directly calculate the optical constants n (real part of refractive index) and κ (extinction coefficient) of any sample by using

$$n - i\kappa = \sqrt{\sin^2\theta_i \left(1 + \tan^2\theta_i \left(\frac{1-\rho}{1+\rho}\right)^2\right)}\,, \tag{3.30}$$

where

$$\rho = \frac{r_p}{r_s} = \tan\Psi e^{i\Delta}\,. \tag{3.31}$$

The relation in Eqs. (3.30) is derived from Eqs. (3.3), (3.21), and (3.22) [77] under assumption that the ambient is air ($N_i = 1.0$). Since the angle of incidence θ_i can be fixed in an experiment, the measured parameters Ψ and Δ for a given wavelength can be used to deduce the complex parameters ρ, and consequently, real parameters n and κ. The single interface is the only case where the inverse relation given in Eq. (3.30) can be derived in an analytical form. For other structures such as thin films, multilayers, etc. we have to use numerical methods for determining material complex refractive index from experimentally recorded ellipsometric angles. Even if the incidence angle θ_i appears explicitly in Eq. (3.30), the value of the complex refractive index does not depend on its selection. However, most accurate results are obtained when θ_i is set close to the Principal or Brewster angle, where r_p (≈ 0) has a significantly different value with respect to r_s (see Figure 3.5 a,b).

Often, it is useful to express the optical properties of a sample by its relative complex dielectric permittivity $\varepsilon = \varepsilon_r - i\varepsilon_i$. In this case it can be shown that

$$\varepsilon_r = n^2 - \kappa^2 = \sin^2\theta_i \left[1 + \tan^2\theta_i \frac{\cos^2 2\Psi - \sin^2 2\Psi \sin^2\Delta}{(1 - \sin 2\Psi\cos\Delta)^2}\right]\,, \tag{3.32}$$

$$\varepsilon_i = 2n\kappa = -\frac{\sin^2\theta_i \tan^2\theta_i \sin 4\Psi \sin\Delta}{(1 - \sin 2\Psi\cos\Delta)^2}\,. \tag{3.33}$$

Determination of optical constants of bulk nickel ferrite

To give an example of application of the inverse relation, Eq. (3.30), we present determination of the refractive index of $NiFe_2O_4$ bulk single crystal in the spectral range covering the visible and ultraviolet regions [78]. Figure 3.6a shows spectrally dependent parameters Ψ and Δ recorded on the single-crystal (111) facet for two incidence angles 40°

and 60°. The refractive index n and extinction coefficient κ calculated from experimental ellipsometric spectra using the inverse relation in Eq. (3.30) are plotted in Fig. 3.6b. It is clear from Figure 3.6a that Ψ and Δ parameters depend on the angle of incidence. However, this is not the case for the optical constants n and κ shown in Figure 3.6b that are on the angle of incidence independent, as pointed out earlier in the text below Eq. (3.31).

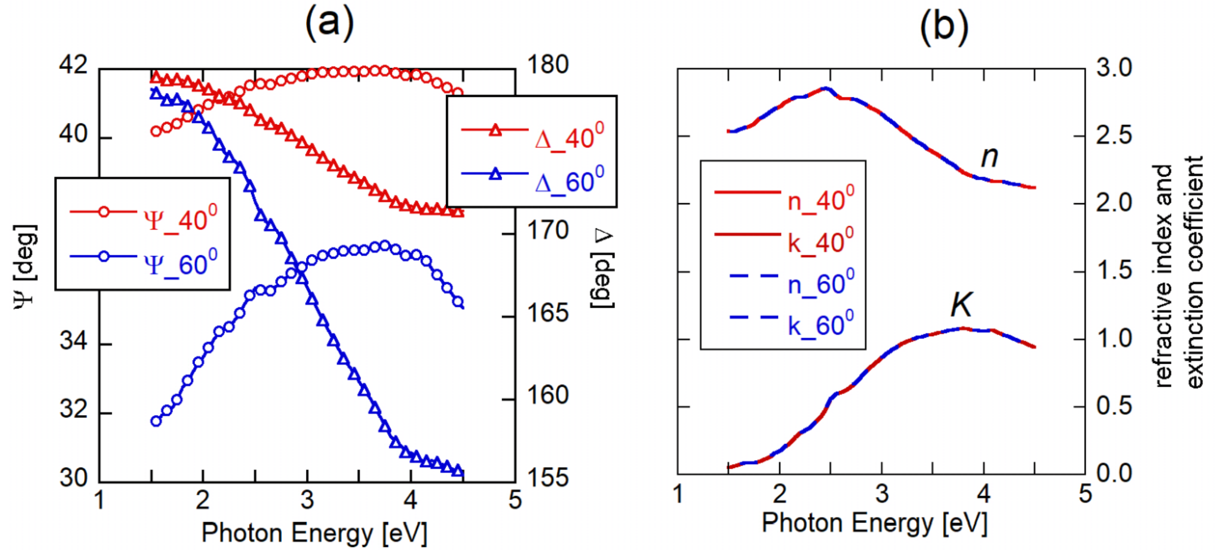

Fig. 3.6: Recorded ellipsometry parameters on $NiFe_2O_4$ single crystal (a) and its optical constants determined by the inverse formula, Eq. (3.30), (b).

Beilby overlayer - limitation of single interface approximation

Precautions must be taken when approximating the surface of a bulk material with a single interface. A single interface is an ideal structure that presents an abrupt and sharp change in refractive index across a planar interface between two semi-infinitive media, the ambient, and sample. In practice, it is rather difficult to prepare such surfaces. Mechanical polishing usually causes a so–called Beilby overlayer that accumulates various defects due to the mechanism of polishing [79, 80]. This damaged layer can be reduced in thickness if a proper polishing process is selected or removed by electropolishing. Alternatively, sample cutting or monocrystal cleaving in vacuum or the deposition of an optically thick film may be used. The Beilby overlayer may present different optical properties than the bulk, and if not carefully considered, erroneous optical constants are determined.

Actually, when the determined n and κ are found to be incidence angle dependent, the approximation of a single interface is no longer valid. It is often because the sample surface exhibits a more complex structure (for example, an overlayer or roughness) or due to the optical anisotropy of a sample. In this case, the inverse relation, Eq. 3.30, may still be used, but the determined n and κ values are called *pseudo-optical constants* rather than optical constants of a material.

Ellipsometry as a phase–sensitive method is extremely sensitive to the sample surface and subsurface down to the level where the light can penetrate, i.e., approximately to the thickness of the penetration depth d_p. As the penetration depth is defined by the inverse of the absorption coefficient α, its value is wavelength dependent and this should be taken into account during the analyses.

3.3.2 Optically anisotropic sample

Let us consider light reflection from an optically anisotropic sample (cf. Fig. 3.4b). The reflection matrix is no more diagonal as it was in the case of the isotropic sample, but instead, its off–diagonal elements become non–zero indicating mixing of s– and p–waves upon reflection. Compete optical characterization of the sample requires the determination of refractive indices (electric permittivities) along the principal axes as well as the orientation of principal axes themselves with respect to sample surface and the incidence plane (through so–called *Euler angles* [35]). Ellipsometric parameters $[\Psi, \Delta]_{pp}$,

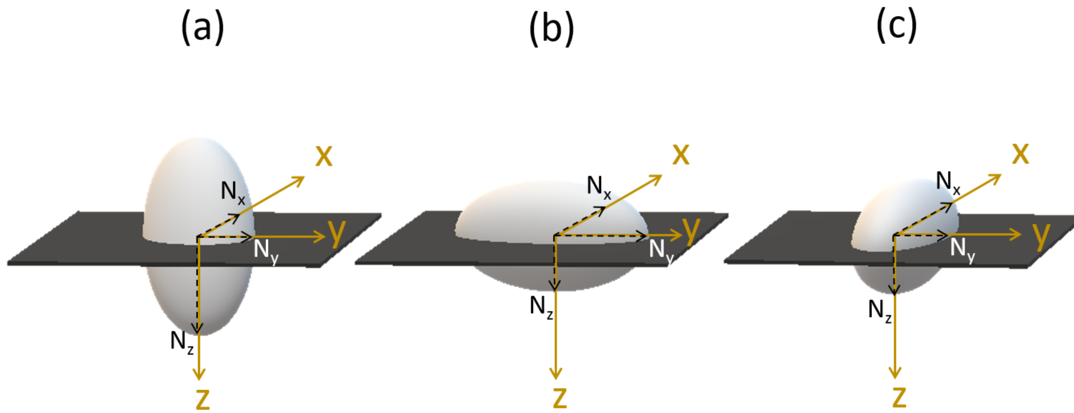

Fig. 3.7: Particular orientations of Fresnel indicatrix for which the reflection matrix gets a diagonal form even for optically anisotropic samples.

$[\Psi, \Delta]_{ps}$, and $[\Psi, \Delta]_{sp}$, Eq. (3.14-3.16), are, if recorded only for one sample orientation, in general, insufficient to provide complete optical characterisation of a sample with bi–axial optical anisotropy. Therefore, measurements on various sample crystallographic facets, while orientating incidence plane along different directions, is usually necessary.

However, there are special cases for which the reflection matrix gets a diagonal form, even for optically anisotropic samples. It corresponds to orientations of the indicatrix indicated in Fig. 3.7 with the principal axes co-linear with the sample related Cartesian system (x, y, z). For these special cases, and with an assumption that the incidence plane is $x = 0$, the off-diagonal elements of the reflection matrix are null, and the diagonal ones

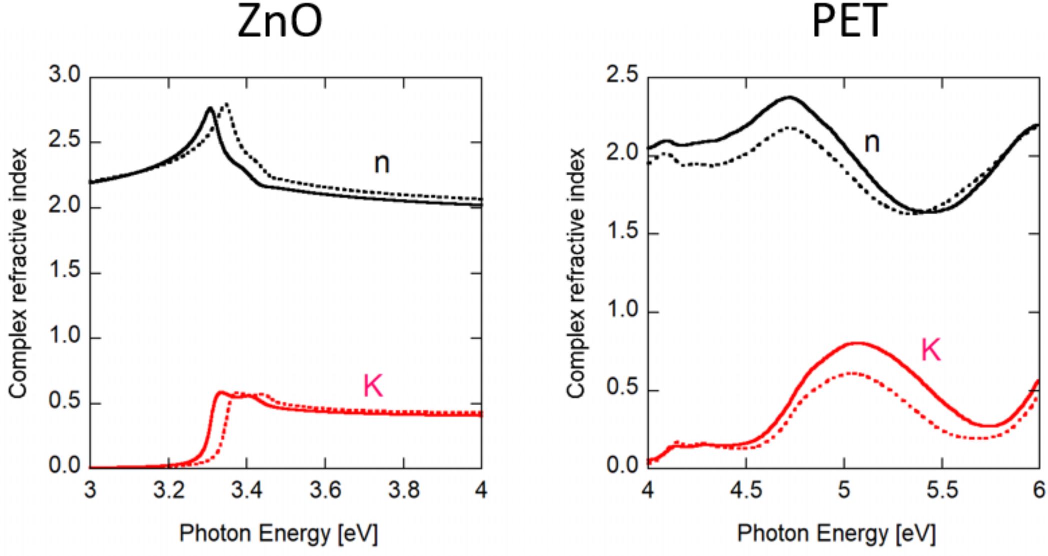

Fig. 3.8: Determined ordinary (solid lines) and extraordinary (broken lines) refractive indices of uni–axial anisotropic ZnO monocrystal (left) and PET foil (right).

get form [35]

$$r_{ss} = \frac{N_i \cos\theta_i - \sqrt{N_x^2 - N_i^2 \sin^2\theta_i}}{N_i \cos\theta_i + \sqrt{N_x^2 - N_i^2 \sin^2\theta_i}}, \quad , \tag{3.34}$$

$$r_{pp} = \frac{N_y N_z \cos\theta_i - N_i \sqrt{N_z^2 - N_i^2 \sin^2\theta_i}}{N_y N_z \cos\theta_i + N_i \sqrt{N_z^2 - N_i^2 \sin^2\theta_i}}, \quad , \tag{3.35}$$

where N_i is ambient refractive index and N_x, N_y and N_z represent refractive indices along the principal axes.

Determination of ordinary and extraordinary refractive index of ZnO and PET

Next, we will consider the determination of ordinary (N_o) and extraordinary (N_e) refractive indices of two uni–axial samples (ZnO monocrystal and PET foil). Measured ellipsometric parameters Ψ_{pp} and Δ_{pp} in experimental configuration indicated in Fig. 3.7a, where optical axis is perpendicular to sample surface, are influenced by optical constants with the dominant contribution of ordinary (in–plane) but also non–negligible contribution of extraordinary (out–of–plane) refractive index (the ratio of which depends on incidence angle). Nevertheless, both ordinary and extraordinary refractive indices can be easily distinguished when the optical axis lies in the sample surface and two measurements, with the optical axis parallel and perpendicular to the incidence plane, are carried out (cf. Fig. 3.7b,c). Ratios of diagonal elements of reflection matrix (off–diagonal are zeros) take form:

- Case where optical axis is parallel to incidence plane, Fig. 3.7b

$$\frac{r_{pp}}{r_{ss}} = \left(\frac{N_e N_o \cos\theta_i - \sqrt{N_o^2 - \sin^2\theta_i}}{N_e N_o \cos\theta_i + \sqrt{N_o^2 - \sin^2\theta_i}}\right)\left(\frac{\cos\theta_i - \sqrt{N_o^2 - \sin^2\theta_i}}{\cos\theta_i + \sqrt{N_o^2 - \sin^2\theta_i}}\right)^{-1}. \tag{3.36}$$

- Case where optical axis is perpendicular to incidence plane, Fig. 3.7c

$$\frac{r_{pp}}{r_{ss}} = \left(\frac{N_o^2 \cos\theta_i - \sqrt{N_o^2 - \sin^2\theta_i}}{N_o^2 \cos\theta_i + \sqrt{N_o^2 - \sin^2\theta_i}}\right)\left(\frac{\cos\theta_i - \sqrt{N_e^2 - \sin^2\theta_i}}{\cos\theta_i + \sqrt{N_e^2 - \sin^2\theta_i}}\right)^{-1}. \tag{3.37}$$

In both cases, the ambient refractive index was assumed to be $N_i = 1$. Solution of these coupled nonlinear equations (3.36) and (3.37) provide ordinary and extraordinary complex refractive indices. A wide incidence angle scan is usually recommended to obtain reliable results. This above mentioned approach was used for optical characterization of ZnO monocrystals and PET foils. Determined refractive indices are presented in Fig. 3.8.

3.3.3 Normal reflectivity and Kramers-Kronig analyses

For normal incidence, p– and s– polarization cannot be distinguished. The reflection coefficient is then polarization-independent, and if the air is considered as an ambient, we get

$$r = \frac{1 - n + i\kappa}{1 + n - i\kappa}. \tag{3.38}$$

Hence, determination of refractive index n and extinction coefficient κ of studied material requires knowledge of both absolute value and phase ϕ of the normal incidence reflection coefficient

$$r = |r|e^{i\phi} = \sqrt{R}e^{i\phi}.$$

Experimentally accessible normal-incidence reflectivity, R, provides only absolute value of the reflection coefficient. However, when reflectivity is known, in the whole spectral range, then the phase of the reflection coefficient can be calculated with the help of Kramers–Kronig relation [18]

$$\phi(\omega) = \frac{-2\omega}{\pi}\int_0^\infty \frac{\ln\sqrt{R(\omega')}}{\omega'^2 - \omega^2} d\omega' \tag{3.39}$$

and refractive index and extinction coefficient of probed material are obtained from

$$n = \frac{1 - R}{1 + R + 2\sqrt{R}\cos\phi}, \tag{3.40}$$

$$\kappa = \frac{2\sqrt{R}\sin\phi}{1 + R + 2\sqrt{R}\cos\phi}. \tag{3.41}$$

Nevertheless, in reality, the reflectivity cannot be measured in the *whole* spectral range

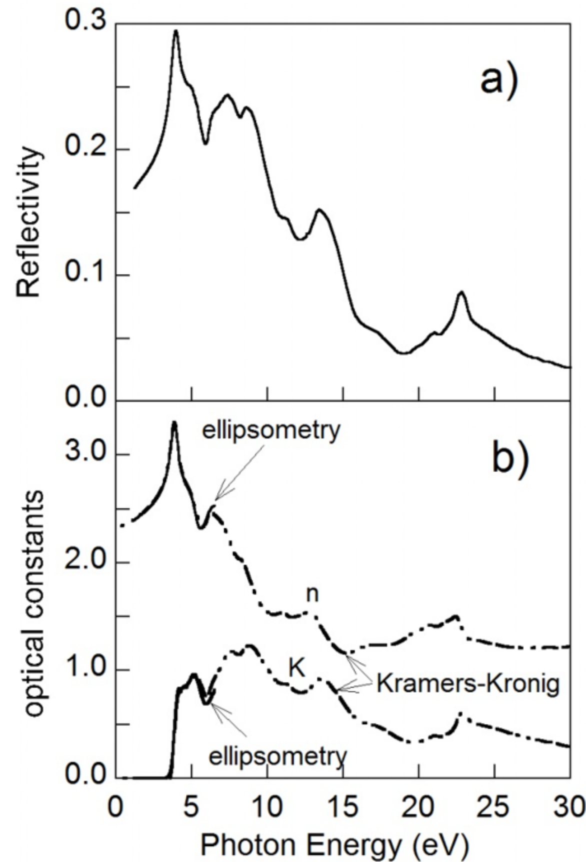

Fig. 3.9: Normal-incidence reflectivity of PZT a) and its complex refractive index b) determined by Kramers – Kronig relations [81]. Experimental data were recorded on a synchrotron facility UVSOR, Japan. Comparison with ellipsometry is also presented (solid line) [82]. Modified from Mistrík et al. [83].

covering all frequencies. Fortunately, Kramers - Kronig relation (Eq. (3.39)) can still be used when extrapolation of the experimentally available spectrum of reflectivity is carefully done in both spectral limits. Often, this method combines visible, ultraviolet, and vacuum ultraviolet spectrophotometry or synchrotron facility to cover as wide spectral range as possible. For high energy of photons, the surface quality (mainly surface roughness) becomes extremely important, and for non–negligible roughness, correction on light scattering lost in reflected beam must be considered [84].

Determination of optical constants of $PbZr_{1/2}Ti_{1/2}O_3$

As an example of normal reflectivity measurements combined with Kramers–Kronig analyses, we provide experimental broadband reflectivity spectrum recorded on optically opaque $PbZr_{1/2}Ti_{1/2}O_3$ (PZT) film at synchrotron facility and corresponding calculated spectra of PZT refractive index and extinction coefficient in Figure 3.9.

Other non-ellipsometric techniques for the determination of optical constants of bulk samples, for instance, examination of oblique incidence reflectivity R_p and R_s, method of minimal deviation, or critical angle, are treated, for example, in [36].

3.4 Single layer

A single layer can be regarded as a plane–parallel layer sandwiched between two semi–infinitive media, the ambient, and the substrate. Optical spectra recorded of a single layer often contain interference fringes due to multiple internal reflections. As an example, we present in Figure 3.10 an optical reflectance spectrum of a chalcogenide amorphous thin film. The interference fringes, which appear very clearly in the VIS range, weaken as the thin film starts to absorb and completely disappear in the UV range because of high light absorption in the layer. Derivation of the reflection coefficients of a single layer is

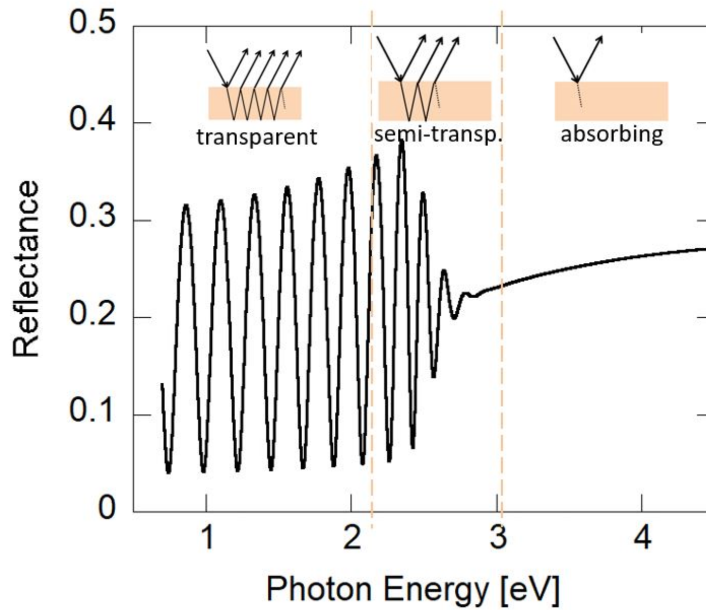

Fig. 3.10: Typical reflectance spectrum of an amorphous chalcogenide thin film.

presented in numerous textbooks on optics (see, e.g., [2]). One possible way, solution of Maxwell's equations with the appropriate boundary condition on the two interfaces, is an extension of that already mentioned for a single interface in Section 3.3. Alternatively, we can consider multiple internal reflections in a film and calculate the complex amplitude of the reflected beam as a coherent superposition (summation) of their infinite contributions. For s– and p– polarizations, respectively, we get

$$r_s = \frac{r_{1s} + r_{2s} e^{-i2\phi}}{1 + r_{1s} r_{2s} e^{-i2\phi}}, \tag{3.42}$$

$$r_p = \frac{r_{1p} + r_{2p} e^{-i2\phi}}{1 + r_{1p} r_{2p} e^{-i2\phi}}, \tag{3.43}$$

where r_1 and r_2 are the reflection coefficients for the upper (ambient-layer) and lower (layer-substrate) single interface, respectively (see Eqs. (3.21) and (3.21)). The angle ϕ is given by

$$\phi = \frac{2\pi d}{\lambda}\sqrt{N_1^2 - N_0^2 \sin^2\theta_0}\,, \tag{3.44}$$

which represents the phase change of a wave propagating through the film with thickness d and refractive index N_1. θ_0 is the angle of incidence, and N_0 is the refractive index of the ambient. Using Eqs. (3.42)–(3.44), we can easily calculate the reflectance for a single film as shown in Eq. (3.7) and the ellipsometry parameters from Eq. (3.3). However, it should be noted that relations in Eqs. (3.42)–(3.44) are valid only for sufficiently thin layers with a thickness smaller than the coherence length of the interacting (probe) light. In a region with strong absorption (penetration depth being much smaller than the layer thickness), light senses only the layer surface (upper interface) and may not reach the substrate. In this case, the single–layer reflection coefficients reduce to the simpler Fresnel formulas given in Eqs. (3.21) and (3.22) derived for a single interface. In this absorbing spectral range, the reflected light does not carry any information on the sample thickness.

In general, ellipsometric spectra provide useful information on the geometrical (film thickness) and optical (film complex refractive index) properties of a sample. However, the desired optical and geometrical parameters cannot be expressed analytically as explicit functions of experimental Ψ and Δ angles as it was done previously in Eqs. (3.30) and (3.31) for bulk samples. On the contrary, the solution of this inverse problem for a thin film requires the construction of a so–called sample model that consists of the optical constants of the substrate, layer, and ambient together with the layer thickness. Selected parameters (refractive indices and the layer thickness) are then adjusted by a numerical procedure where the differences between theoretically calculated and experimental Ψ and Δ data are iteratively minimized by nonlinear fitting procedures. For the calculation of fitting errors, χ, various figure of merit functions have been designed. We mention here one given by [85]

$$\chi = \frac{1}{\sqrt{M-P-1}}\sqrt{\sum_{j=1}^{M}\left[\left(\frac{\Psi_{exp}(\lambda_j) - \Psi_{teo}(\lambda_j)}{\delta\Psi(\lambda_j)}\right)^2 + \left(\frac{\Delta_{exp}(\lambda_j) - \Delta_{teo}(\lambda_j)}{\delta\Delta(\lambda_j)}\right)^2\right]}\,, \tag{3.45}$$

where ($\delta\Psi$, $\delta\Delta$) are measurement errors of (Ψ, Δ). M and P give number of measured spectral points and adjusted parameters, respectively.

For each measured wavelength, ellipsometry provides only two recorded angles Ψ and Δ. That limits the number of searched (adjusted) parameters of the sample model that can be independently and uniquely determined. Nevertheless, this number may be increased by the following approaches:

1. Parameterization of optical constants by appropriate analytic formulas.

2. Requirement of Kramers–Kronig consistency between the real and imaginary parts of optical constants.

3. Measurement of Ψ and Δ for different angles of incidence.

4. Application of appropriate strategies that can simplify data treatment as, for example, determination of layer thickness from the transparent part of the spectra.

5. Adding transmittance and reflectance spectra for simultaneous data treatment.

6. Multiple sample method.

Considering some of the above suggestions enables one to increase the number of adjusted parameters to about 12 and to reduce their mutual correlations within the tolerable limits.

3.4.1 Ideal $As_{50}Se_{50}$ chalcogenide film

As an example of optical characterization of a single layer, we present in Figures 3.11a–c experimental ellipsometric, transmittance, and reflectance spectra of chalcogenide $As_{50}Se_{50}$ amorphous film deposited on a float glass substrate. The backside of the substrate was grounded before recording the ellipsometry and reflectance data to suppress spurious reflections from the interface. The single–layer sample model (see Figure 3.11d) was then designed as a homogenous thin film sandwiched between two semi–infinitive media: the ambient and substrate. The transmittance spectrum for normal incidence was calculated by

$$T = n_2|t|^2 \,, \tag{3.46}$$

where n_2 is the refractive index of the substrate and

$$t = \frac{t_1 t_2 e^{-i\phi}}{1 + r_1 r_2 e^{-i2\phi}} \,, \tag{3.47}$$

is a single–layer transmission coefficient. The phase change ϕ is defined by Eq. (3.44), r_1 and r_2 are reflection coefficients of the upper and lower interfaces, respectively (see Eqs. (3.21)–(3.22)) and, analogously, t_1 and t_2 are the transmission coefficients for the upper and lower interfaces, respectively (see Eq. (3.23)).

The refractive index of float glass was determined formerly by spectroscopic ellipsometry carried out on a naked substrate considering it as a bulk material (see Section 15.5, Eqs. (3.30) and (3.31)). The optical constants (electric permittivity) of the chalcogenide film were parameterized by a Tauc–Lorentz formula (a combination of the Lorentz oscillator and Tauc absorption edge), which was developed for amorphous semiconductors [86]. The imaginary part of the Tauc–Lorentz electric permittivity ε_2 at photon energy E is then given by

$$\varepsilon_2 = \frac{A E_0 C (E - E_g)^2}{(E^2 - E_0^2)^2 + C E^2} \frac{1}{E} \qquad E > E_g \,, \tag{3.48}$$

$$\varepsilon_2 = 0 \qquad E \leq E_g \,, \tag{3.49}$$

and the real part ε_1 is calculated with the help of the Kramers–Kronig relations given in Eq. (2.69) or by an analytic expression [86]. Parameters of the Tauc–Lorentz formula together with the film thickness were the free parameters adjusted by the fitting procedure. Figure 3.11e presents determined spectral dependence of $As_{50}Se_{50}$ electric permittivity. In addition, Figure 3.11f shows the absorption coefficient α and penetration depth d_p of

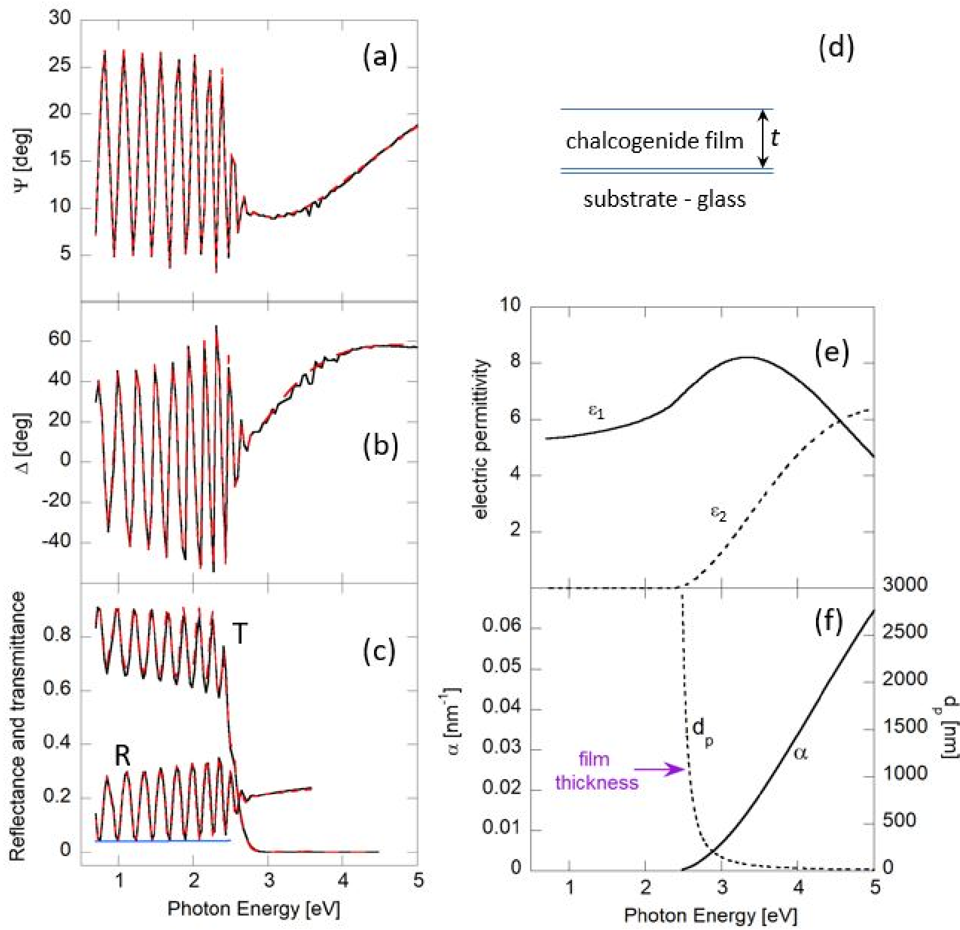

Fig. 3.11: Ellipsometry and spectrophotometry measurements of a thin film of $As_{50}Se_{50}$ as a function of photon energy. The best-fit ellipsometry parameters Ψ and Δ are plotted in (a) and (b), respectively, spectrophotometry transmittance and reflectance in (c), the sample model in (d), the determined electric permittivity ε_1 and ε_2 of $As_{50}Se_{50}$ in (e), and its absorption coefficient α and penetration depth d_p in (f).

$As_{50}Se_{50}$, and indicates its thickness as well for comparison. The adjusted values of all searched parameters are listed in Table 3.1.

Ellipsometry is a precise and sensitive spectroscopic tool, but when operating solely in the reflection configuration, its sensitivity for low absorption coefficient is limited. That is because reflected light senses only the sample surface and its close vicinity. It

Parameter	value
t [nm]	$1085,5 \pm 1.1$
A [eV]	155.16 ± 1.39
E_0 [eV]	4.55 ± 0.03
C [eV]	6.09 ± 0.09
E_g [eV]	2.351 ± 0.001
ε_∞	1.05 ± 0.01

Tab. 3.1: Adjusted values of $As_{50}Se_{50}$ film thickness and parameters of Tauc-Lorentz formula (Eg.(3.48)).

is commonly agreed that ellipsometry can provide reliable results for absorption coefficients $\alpha > 10^5\,\mathrm{cm}^{-1}$ [34]. If α is in the range $10^3 - -10^5\,\mathrm{cm}^{-1}$, usually the transmittance spectrum is required to be treated simultaneously with ellipsometry data to ensure accurate determination of the absorption coefficient. In the region of low absorption, $\alpha < 10^3\,\mathrm{cm}^{-1}$, other techniques such as photocurrent measurement or photothermal deflection spectroscopy are more appropriate [87].

It is worth noting that thin-film optical characterization can also be performed by analyzing the sole transmittance spectrum. This approach was developed by Swanepole [88]. Generally speaking, the thickness of the film is determined by the density of the interference fringes, whereas its refractive index is calculated from the difference between their maxima and minima. The absorption coefficient in the semi–transparent and absorbing regions can also be estimated by its parameterization and subsequent fitting. Nevertheless, ellipsometry, which for each wavelength records two parameters instead of only one, gives more accurate results due to its phase-sensitive nature.

Real thin films often show various kinds of non–idealities, for example, nonuniform thickness, surface roughness, internal non-homogeneity, refractive index gradient, etc. In these cases, a more sophisticated treatment surpassing single layer approximation is to be applied [89].

3.4.2 Assessment of defects in SiO_2 films

A relatively easy examination of defects and non–idealities in a thin film can be done by comparing its reflectivity spectrum with that of the bare substrate. Theoretical considerations predict that the reflectance spectrum of the uncoated substrate coincides with the upper or lower (depending on the refractive index difference between the substrate and the film) envelope of the film reflectance interference fringes[5]. This situation is shown in Figure 3.11c, where the homogenous chalcogenide thin film reflectance spectrum is plotted together with the reflectance of its bare glass substrate (in blue). If such a coincidence is not found, then the film cannot be regarded as a homogeneous single layer, or substrate refractive index changed near the film/substrate interface due to deposition.

[5]This holds for an ideal film and in the spectral range of its transparency.

To demonstrate the latter case, we will consider a study of SiO_2 thin film deposited by high-density reactive ion plating on a glass substrate [90]. Figure 3.12(left) compares the reflectance spectrum of the thin film (in black) with the reflectance spectrum of the uncoated substrate (in pink). As one can see, the maxima of the film interference fringes do not coincide with the reflectance spectrum of the uncoated substrate. Therefore, the model of a single homogeneous SiO_2 layer on an unmodified glass substrate cannot be correct. Consequently, three different sample models consistent with the experimental findings were considered (see Figure 3.12 right and middle parts).

The first model, drawn on the top of the right-hand side of Figure 3.12, describes the formation of a thin transition layer (TL) between the SiO_2 layer and the glass substrate with a parabolic refractive index profile. In this model, it is assumed that the refractive index of the bottom part of the TL, which is in contact with the substrate, has the same value as that of the glass substrate. The second model, in the middle, assumes that the SiO_2 film is a single layer with a linear profile of its refractive index. In the third model, at the bottom, a change in the glass refractive index close to the SiO_2/glass boundary is assumed.

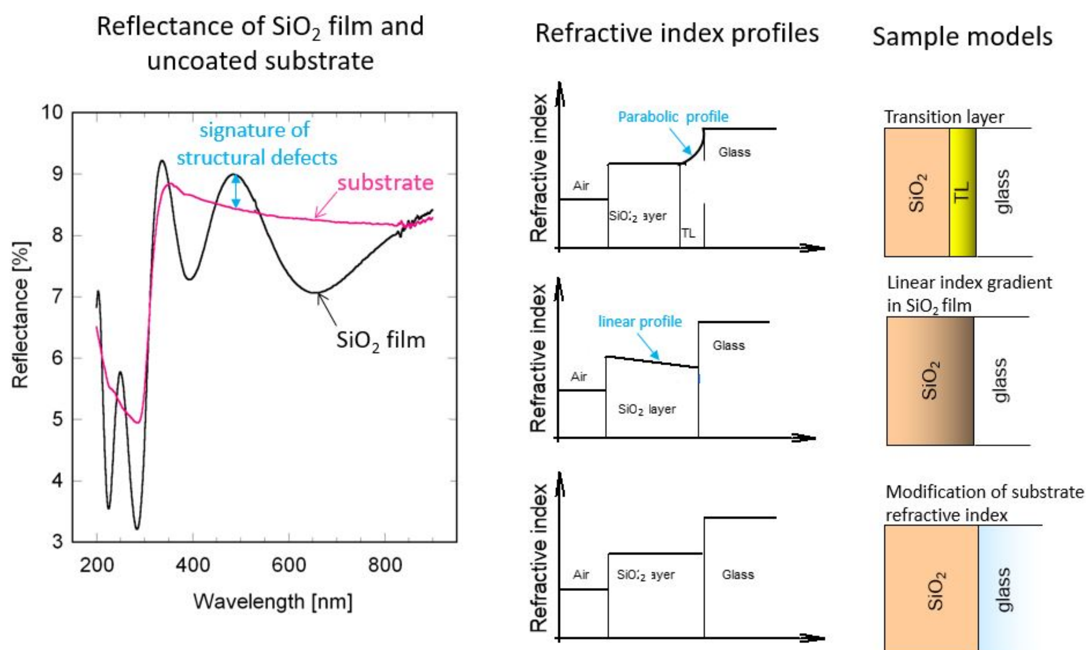

Fig. 3.12: Signature of structural defects in the SiO_2 layer presented in the reflectance spectra (left, modified from Mistrík et al. [90]), considered sample models for ellipsometry and reflectance spectra interpretation (right), and refractive index profile of each designed sample model (middle).

It is worth mentioning here that the proposal of different sample models that are acceptable from the technological point of view is essential to ensure correct interpretation of the recorded optical spectra. That helps in selecting the most reliable sample model while evaluating the fitting errors in the simultaneous treatment of the ellipso-

metric, reflectance, and transmittance spectra together with results of complementary characterization methods. In the case of the study of the SiO_2 thin film, it was the third model (a change in the glass refractive index) that was recognized as the most reliable [90]. Theoretical approaches developed to account for thin-film defects are presented in monographs focused on spectroscopic ellipsometry, e.g., Refs. [2, 73, 35] or in selected review chapters, e.g., [89].

3.5 Multilayer

Continuous demand for better–performing optical elements requires surface structuring or functionalization, which is more complex than depositing a single layer. The concept of multilayers has proved to find broad applications, e.g., as antireflection coatings, omnidirectional mirrors, and optical filters [91]. On the other hand, a single layer considered above in Section 3.4 often manifest in real conditions a complex inner structure due to, for example, specific modes of growth during deposition. That can be usually satisfactorily approximated by a multilayered structure. Therefore, understanding optical interactions in a multilayer becomes very useful from both application and characterization points of view.

Reflection and transmission coefficients for bi–layers and tri–layers have been derived in analytical form and can be found in a few textbooks or review papers (see, e.g., Refs. [1, 92, 93]. A more general approach of treating the light interaction within a stratified medium involves recursion or matrix calculations (see, e.g., Refs. [1, 2, 84]). The matrix calculation expands and generalizes treatment discussed already in Section 3.4. Here again, one has to solve the wave equation in each layer independently, and then the solutions are subjected to the boundary conditions at the interfaces enforcing the requirement of continuity of tangential electric and magnetic field components. The light interaction with the whole multilayer structure is then obtained by subsequent matrix multiplication of 2×2 matrices developed for each layer and interface, which finally reveal the reflection and transmission coefficients or ellipsometry parameters of the multilayer.

3.5.1 Inner structure and quality of nanocrystalline diamond films

This section aims to present a case study where a nanocrystalline diamond (NCD) film's inner structure was approximated by a multilayer [94]. Another objective is to emphasize the potentiality and complementarity of spectroscopic ellipsometry as a characterization tool of nanostructures. The structure of NCD films deposited by microwave–plasma–enhanced chemical vapor deposition on a substrate pre–seeded by nano–diamond (ND) particles is schematically shown in Figure 3.13. Diamond growth starts on seeded ND particles in the form of small crystallites or grains, which increase in volume and then coalesce at a certain distance from the substrate. When the film is completely closed, the grains continue to increase in volume following van der Drift growth, where the larger

grains suppress the growth of their smaller neighbors. This type of growth typically results in the columnar film structure. The size of the grains increases with the film thickness (together with the surface roughness), and when its average diameter surpasses about 100 nm, the film becomes microcrystalline rather than nanocrystalline.

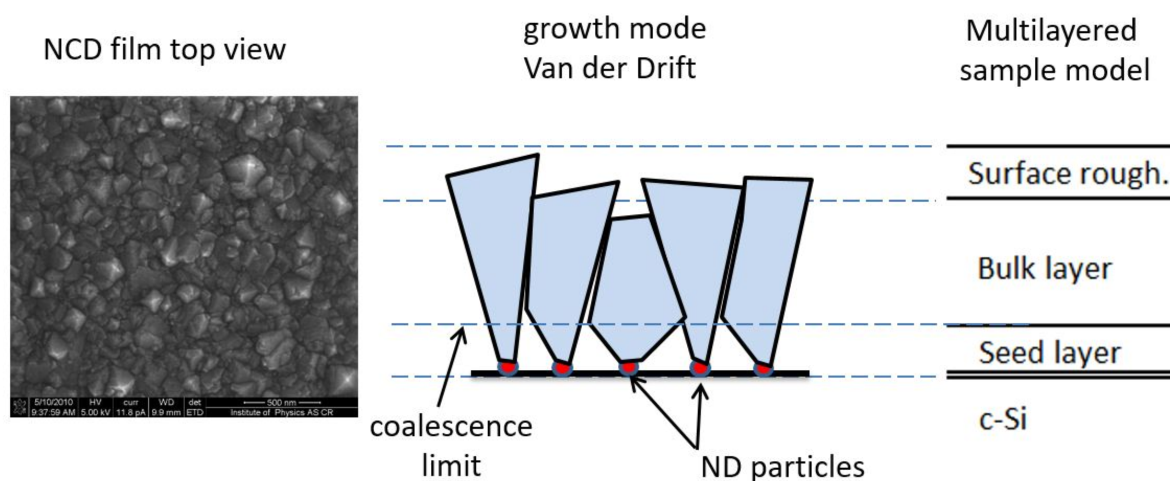

Fig. 3.13: SEM top view picture of NCD film (left). Schematic drawing of van der Drift growth mode (middle). Sample model structure for ellipsometry data analyzes (right).

To be able to analyze recorded ellipsometric spectra, first, a sample model structure has to be designed. A good strategy is to start with a sample model that is rather simple (a single layer in our case) and then gradually refine it with respect to the expected growth mode of the layer and/or with respect to the knowledge provided by complementary characterization tools if they are available. The refined sample model structure is presented in Figure 3.13 (middle) and (right) and consists of a substrate that is a naturally oxidized crystalline Si wafer. The substrate is then covered by a seed layer (a layer grown from seeded ND particles, dots in red, up to a coalescence limit), bulk layer (dense columnar part in blue), and surface roughness layer on the top. Optical constants of NCD were parameterized by the Tauc—Lorentz formula [86] given in Eqs. (3.48) and (3.49). The optical constants of seed and surface layers, where voids are expected, were parameterized by the effective medium approximation (EMA), which is treated in more detail later in the text. This multilayer system has been used to fit experimentally recorded ellipsometry spectra. The best–fit results are presented in Figure 3.14a and have revealed both the optical constants of NCD and the inner structure of NCD film of appropriate thicknesses of seed, bulk, and surface sublayers (see Figure 3.14c,d).

It is often advisable, especially when a large number of adjusted parameters is searched by the fitting procedure (9 in our case), to compare the determined sample structure with complementary characterization techniques. These are usually scanning probe methods such as atomic force microscopy (AFM), scanning electron microscopy (SEM), or transmission electron microscopy (TEM). Figure 3.14b presents SEM picture of the NCD film

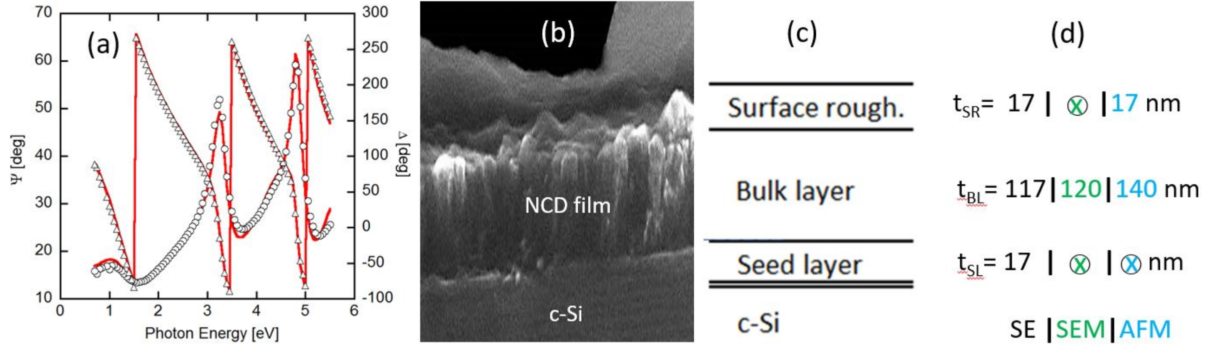

Fig. 3.14: Best fit ellisometry spectra for selected incidence angle of 65° (a). SEM picture of NCD film cross section (b). Sample model structure for ellipsometry data analyzes (c). Determined inner structure by spectroscopic ellipsometry, scanning electron microscopy and atomic force microscopy in (d).

cross-section, and Figure 3.14d compares values of the film surface roughness and bulk and seed layer thicknesses determined independently by spectroscopic ellipsometry, SEM, and AFM. It is worth mentioning that spectroscopic ellipsometry provides most details of the NCD film inner structure and that the obtained values of the searched parameters are rather close to these determined by other characterization techniques.

Besides determining the inner structure, we can further assess the "diamond quality" of NCD films. NCD consists mainly of sp^3 hybridized carbon atoms arranged in grains with a diamond crystalline structure. Apart from this dominant phase, all possible hybridizations (sp^3, sp^2, and sp^1) might be present at defect sites and are localized mainly in the grain joints and seed layer where the coalescence is reached. The optical constants of a material composed of a host medium filled with different types of inclusions can be approximated by the EMA [95] that takes into account the host and inclusion material optical properties and their corresponding filling factors. Therefore, considering EMA with the diamond phase as the host and non-diamond phases as the inclusions, the "diamond quality" could be estimated from the spectro–ellipsometric analyses by assessing the filling factors ratios.

EMAs are based on the well-known Clausius–Mossotti relation given by [2]:

$$\frac{\varepsilon_1 - 1}{\varepsilon_2 + 2} = \frac{Na}{3\varepsilon_0}\,, \tag{3.50}$$

which relates the macroscopic electric permittivity ε of a medium with its polarizability α of N electric dipoles. When the medium consists of two components a and b with different polarizabilities α_a and α_b, we can rewrite Eq. (3.50) as

$$\frac{\varepsilon_1 - 1}{\varepsilon_2 + 2} = \frac{1}{3\varepsilon_0}(N_a\alpha_a + N_b\alpha_b)\,. \tag{3.51}$$

Combining Eqs. (3.50) and (3.51), we get the so–called Lorentz—Lorenz formula given

by

$$\frac{\varepsilon_1 - 1}{\varepsilon_2 + 2} = f_a \frac{\varepsilon_a - 1}{\varepsilon_a + 2} + (1 - f_a) \frac{\varepsilon_b - 1}{\varepsilon_b + 2}\,, \tag{3.52}$$

where f_a and $f_b = (1 - f_a)$ are the filling factors of component a and b, respectively. This relation is valid for a medium consisting of spheres placed in a vacuum. If the vacuum is replaced by a host medium with electric permittivity ε_h we get

$$\frac{\varepsilon_1 - \varepsilon_h}{\varepsilon_2 + 2\varepsilon_h} = f_a \frac{\varepsilon_a - \varepsilon_h}{\varepsilon_a + 2\varepsilon_h} + (1 - f_a) \frac{\varepsilon_b - \varepsilon_h}{\varepsilon_b + 2\varepsilon_h}\,, \tag{3.53}$$

Several variations of this relation can be found in the literature. One of them, also known as the Bruggeman approximation, is based on the assumption that $\varepsilon = \varepsilon_h$ [96]. Then Eq. (3.53) becomes

$$0 = f_a \frac{\varepsilon_a - \varepsilon}{\varepsilon_a + 2\varepsilon} + (1 - f_a) \frac{\varepsilon_b - \varepsilon}{\varepsilon_b + 2\varepsilon}\,, \tag{3.54}$$

and can be further extended for more phases. Bruggeman EMA is often used in ellipsometry for modeling the surface roughness formed by a mixture of air and top layer material with a filling factor, typically 50%. Further, Bruggeman EMA has found broader use in the determination of optical constants of composite materials containing two or more phases as well, and, in this form, it has also been applied for estimation of NCD film "diamond quality."

The diamond and non-diamond phases were represented by the optical constants of bulk diamond [97] and amorphous carbon [98], respectively. Numerical treatments of experimental ellipsometric spectra then yielded the filling factors of both the diamond and non-diamond phases. That analysis was applied for NCD films deposited under different deposition conditions (substrate deposition temperature and frequency of pulsed microwave plasma). The obtained results are summarized in the form of a graph shown in Figure 3.15(left), where we indicate the area of the deposition parameters that provide high-diamond-quality NCD films. A complementary technique to assess the diamond quality of the NCD films is Raman spectroscopy. Raman spectra, consistently with ellipsometry, clearly show the improvement of the diamond quality of the NCD films with increasing pulsed plasma frequency. That is demonstrated in Figure 3.15(right) for NCD films deposited with a different pulsed plasma frequency and at a fixed substrate temperature of 550 °C. The presented spectra were normalized to the amplitude of the sharp diamond peak of 1332 cm^{-1} to create direct evidence of the non-diamond contribution dependence of the pulsed plasma frequency. The D (1340 cm^{-1}) and G (1600 cm^{-1}) bands that relate to disordered carbon and graphite, respectively, are clearly visible for all samples and were found to decrease in amplitude as the pulsed plasma frequency increased.

Raman spectra deconvolution can be used for carbon sp^3/sp^2 ratio estimation, but significantly different cross-sections of diamond and non–diamond phases must be considered. The diamond quality of the NCD films determined from the Raman spectroscopy was found to be in the range 92–97%, and similar values of 84–93% were obtained by spectroscopic ellipsometry. It is worth noting that this reasonable agreement was reached

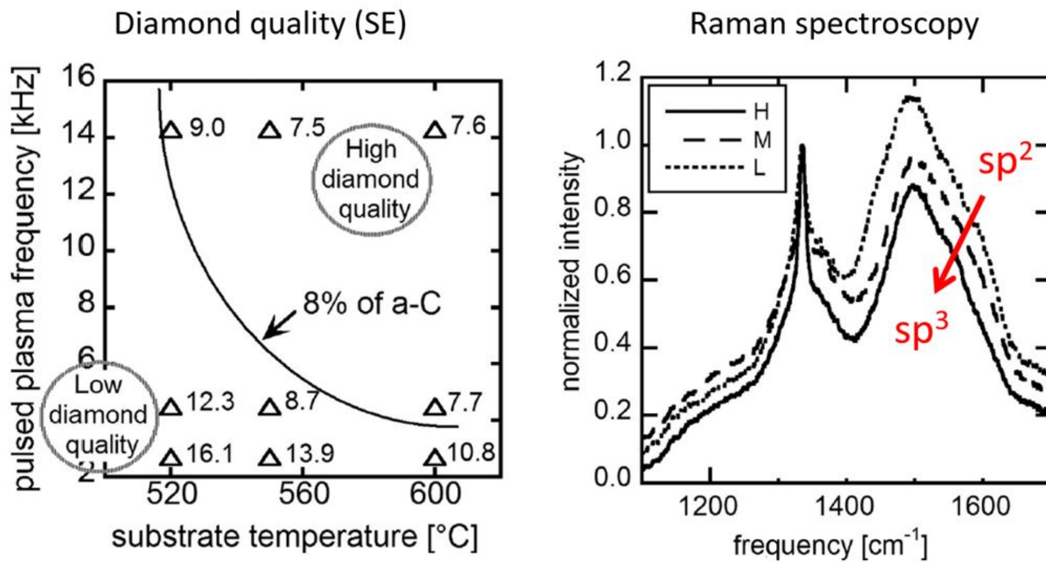

Fig. 3.15: Diamond quality of NCD films deposited with different pulsed MW plasma frequency and substrate deposition temperature as determined by spectroscopic ellipsometry. Indicated are filling factors of the non-diamond amorphous carbon phase and the estimated line of constant a-C filling factor of 8% (left). Raman spectra of NCD films deposited for 550 °C for different frequencies of pulsed plasma (High 14.3 kHz, Middle 4.5 kHz, and Low 2.7 kHz) (right). Modified from Mistrík et al. [94].

in spite of the fact that the exact structure and ratio of sp^1, sp^2, and sp^3 hybridized carbon in defect sites of NCD are not known; therefore, the approximation of the non–diamond phase by amorphous carbon is rather rough (for a more detailed discussion, see [94]).

3.6 Linear grating

As discussed in the preceding sections, ellipsometry is a characterization technique that is routinely used for the characterization of bulks, single layers, and multilayers. In the last three decades, advanced knowledge of electromagnetic field interaction with nanostructured solids together with the enhanced power of personal computers made it possible to apply ellipsometry for the characterization of laterally structured samples as well. That includes, for example, linear gratings or other, even more complex, nanostructures, such as photonic crystals, with periodicity in both lateral and perpendicular directions with respect to the sample surface [99, 100, 101, 102, 103]. In this case, instead of ellipsometry, we refer to scatterometry to distinguish its employment for structured surfaces or photonic crystals. In recent years, scatterometry has gained increased attention also due to its application in on–line control of critical dimensions of nanostructures fabricated in the semiconductor industry.

Calculations of the reflection coefficients of photonic crystals require a more sophisticated mathematical approach with respect to that presented previously for a single interface and single or multilayers. Due to the lateral periodicity of a sample's optical properties or surface profile, it is convenient to expand the interacting electromagnetic field and the sample electric permittivity into Floquet and Fourier series, respectively. The wave equation with suitable boundary conditions is then solved for these expanded fields in the truncated series. This analytical calculation method, known as Fourier modal formalism, treats the Fraunhofer diffraction in general photonic crystal (for more details, see, for example, Refs. [104, 105, 106] and the references therein). Ar the same time, special care has to be taken for the correct implementation of this method, including the control of the convergence of the solution with respect to the truncation of the series. Alternative numerical approaches are available as well, for example, that proposed by Yee, which is based on the finite difference time domain [107]. Because of their extended computational demands, the current commercial ellipsometry software generally does not support this kind of calculation, although some stand-alone routines are available (see, e.g., [108]).

Ellipsometric parameters of light diffracted from gratings or photonic crystals are most convenient to measure in the 0th diffracted order because the angle of diffraction for higher orders is spectrally dependent. Moreover, the 0th diffracted order includes all needed information on both the sample structure (for example, grating profile) and the optical properties of grating materials.

The aim of this section is a brief presentation of scatterometry and its advantages and disadvantages with respect to the conventional characterization techniques. For this purpose, characterization of a sine-like surface relief Ni grating [109] was selected.

3.6.1 Sinusoidal linear Ni grating

A linear Ni grating was fabricated by holographic lithography. Its surface was covered by a native oxide. The grating cross-section is schematically depicted in Figure 3.16

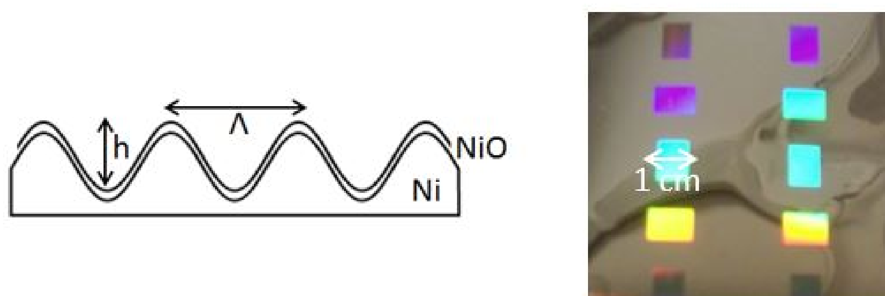

Fig. 3.16: Grating cross-section (left) and top-view photo of a set of holographic gratings (right).

together with the top view of a set of gratings. Besides scatterometry, complementary measurements of the grating profile were performed by conventional techniques: SEM, AFM, and optical microscopy. Corresponding pictures are shown in Figure 3.17. All these tools provided the value of the grating period Λ. Nevertheless, the grating profile depth was determined only by AFM. The obtained results are summarized in Table 3.2. Scanning probe methods (SEM and AFM), including optical microscopy, are relatively fast and flexible. SEM and AFM provide a high-resolution examination of the nanoscale features of the studied samples. Moreover, AFM has also access to the real surface topography. Despite these advantages, there are some drawbacks as well in the use of these tools. For example, SEM requires surface metallization and has only limited access to the surface profile. AFM scans only a small surface area, and therefore, several scans are required to obtain statistically reliable results. In addition, the tip deconvolution artifacts often make precise surface topography evaluation difficult. And optical microscopy suffers from the low resolution with lack of access to the depth profile.

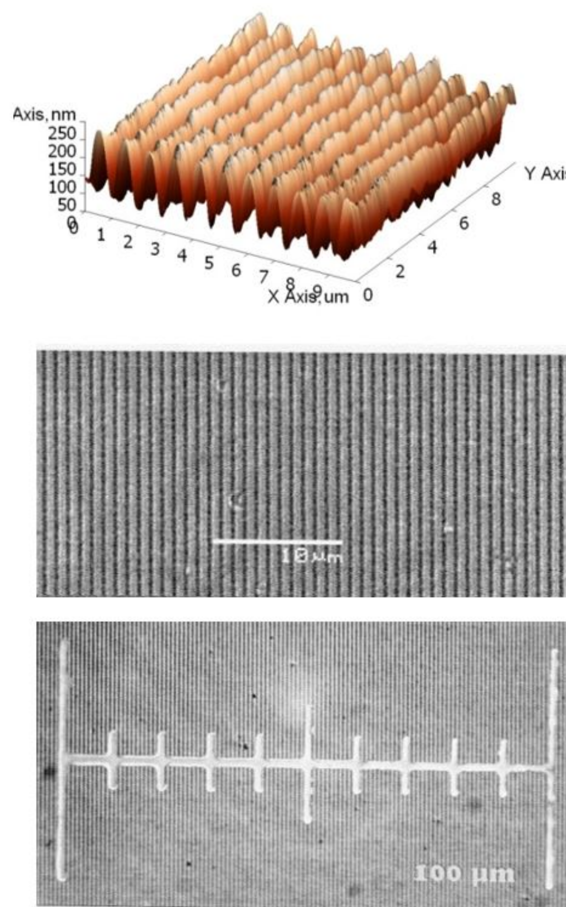

Fig. 3.17: Grating surface recorded by the atomic force microscopy (top), scanning electron microscopy (middle), and optical microscopy (bottom). Reprinted from Mistrík et al. [109].

The ellipsometric parameters Ψ and Δ were recorded for three angles of incidence: 20°, 30°, and 40° in the spectral range from 300 to 1200 nm. The plane of incidence was set perpendicular to the grating lines. Only the 0th order of diffraction (specular reflection) was measured and analyzed. Due to the non–ideal fabrication process, the Ni grating surface relief was not considered perfectly sinusoidal. Therefore, not only the period and depth of the grooves were taken into account in the theoretical calculations, but an additional parameter describing the surface profile non–ideality was considered as well. The thickness of the NiO surface overlayer was evaluated by standard ellipsometry measurement of a nonpatterned part of the sample ($t_{\mathrm{NiO}} = 3.5$ nm). The non–ideality in the grating profile shape was approximated by function

$$z = \frac{h}{2}\left(1 - \cos P(y)\right) , \tag{3.55}$$

where

$$P(y) = \frac{2\pi}{\Lambda}\left(Ay + \frac{2}{\Lambda}(1-A)y^2\right) . \tag{3.56}$$

The parameter A characterizes the shape profile ($A = 0$ corresponds to the ideal sinusoidal case) and y, and z are the Cartesian axes. Extensive theoretical modeling[6] of ellipsometry response of gratings with various profile shapes and depths yielded the following: (1) grating period $\Lambda = 917$ nm, (2) profile depth $h = 205$ nm, and (3) shape profile parameter $A = 0.52$. The best-fit spectrum of the Ψ parameter is presented in Figure 3.18, where we also compare the final grating profile determined by scatterometry with respect to that measured by AFM. The achieved high level of agreement between both profiles is worth noting. The grating period and its depth thus obtained are added in Table 3.2.

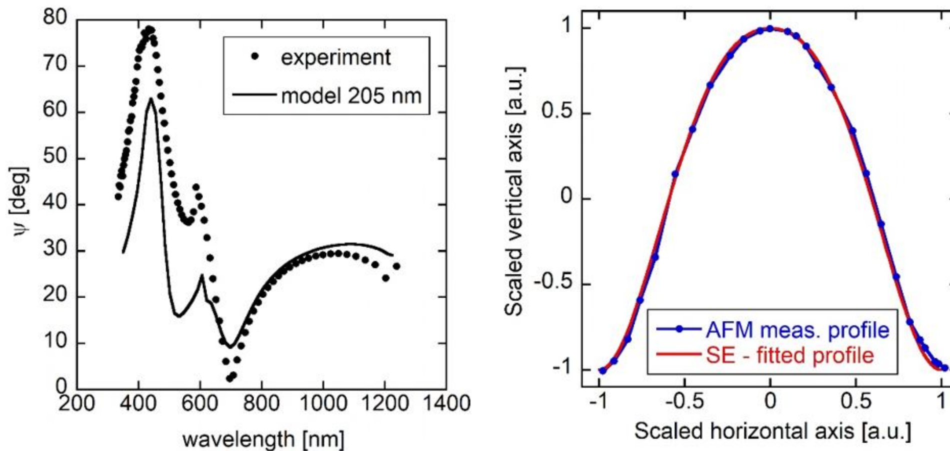

Fig. 3.18: Best fit scaterometry spectra (left) and grating profile determined by scatterometry compared with that measured by AFM (right). Reprinted from Mistrík et al. [109].

[6]Performed in the analytical framework of rigorous coupled-wave analyses [110].

A grating period of about 917 nm is identically obtained by all the applied methods. However, there is a discrepancy between the profile depths determined by AFM (170 nm) and spectroscopic ellipsometry (205 nm). The possible reasons for this discrepancy are AFM tip deconvolution artifacts or ellipsometry sensitivity on grating surface micro-roughness, which was not considered in the sample model. Moreover, the optical constants of Ni and NiO determined on the non–patterned part of the sample may be slightly different from those of the grating. The sensitivity of scatterometry on an overlayer and surface roughness can be considered as an advantage or, contrary, as a disadvantage depending on how precise theoretical analyses are performed. An evident advantage of scatterometry is its noninvasive nature and access to the real profile geometry of the grating surface. Nevertheless, the cumbersome and time-consuming calculations still limit the applications of scatterometry to a relatively small community of researchers.

Grating structural parameters	**Methods**			
	SEM	AFM	Optical microscopy	Spectroscopic ellipsometry
Grating period [nm]	916.7	917.2	918.6	917.0
Profile depth [nm]	x	170	x	205

Tab. 3.2: Determined grating period and profile depth.

Despite the above mentioned disadvantage, scatterometry has proved to be a highly efficient tool for noninvasive characterization of laterally periodical patterned nanostructures. In the case of linear Ni grating, this has been demonstrated by the determination of the grating geometrical parameters (period, depth, and profile shape non–ideality) and also by identification of the NiO surface overlayer. Obviously, all the characterization techniques presented here show comparative advantages and disadvantages, the most evident being listed in Table 3.3.

Method	Advantage	Disadvantage
SEM	Fast and flexible, high resolution	Limited access to surface profile, surface matallization reqired
AFM	Real surface topography	Small surface area scan, tip deconvolution artefacts
Optical microscopy	Fast and flexible inspection	Low resolution, no access to depth profile
Spectroscopic ellipsometry	Sensitive on NiO overlayer and surface profile nonideality, noninvasive	Cumbersome and time expensive calculations

Tab. 3.3: Advantages and disadvantages of applied methods.

3.7 Conclusions

Spectroscopic ellipsometry is a phase-sensitive optical tool employing light polarization (more precisely, its change under light reflection) for surface characterization. It provides surface geometry such as, for example, the overlayer thickness, the inner structure of a film or surface profile of a grating, and also the optical constants of materials that the light senses by its penetration beneath the surface. This technique is not direct in the sense that ellipsometry data treatment usually requires the design of a sample model and subsequent fitting of experimental ellipsometric spectra. An appropriate combination of SE with complementary surface characterization tools guarantees precise and accurate results. The field of ellipsometry is growing continuously, and its potential is expanding towards the characterization of advanced functionalized surfaces and nanomaterials.

Chapter 4

Magneto–optics

Magneto–optical effects in transmission, Faraday and Voigt, were already introduced in Section 2.1.2. The present chapter deals with magneto–optical effects observed upon light reflection from a magnetized sample. For the sake of simplicity, unless otherwise stated, we limit our treatment to samples that are in non–magnetized state optically isotropic.

4.1 Measurable quantities

Net magnetization reduces the symmetry of a sample. Optical effects that originate from this induced anisotropy in reflected light are called the Kerr effects, in honor of their discoverer. It is common to distinguish the polar, longitudinal, and transverse Kerr effects according to the mutual orientation of sample magnetization vector $\boldsymbol{M}$, the plane of incidence, and the sample surface. This is schematically presented in Table 4.1. The

Kerr effect	Polar	Longitudinal	Transversal
Exp. config.			
Reflection matrix	$\begin{bmatrix} r_{ss} & r_{sp} \\ r_{sp} & r_{pp} \end{bmatrix}$	$\begin{bmatrix} r_{ss} & r_{sp} \\ -r_{sp} & r_{pp} \end{bmatrix}$	$\begin{bmatrix} r_{ss} & 0 \\ 0 & r_{pp} \end{bmatrix}$
Symmetry consideration	$r_{ps} = r_{sp}$	$r_{ps} = -r_{ps}$	$r_{ps} = r_{sp} = 0$

Tab. 4.1: Kerr magneto–optical effects in reflection: polar, longitudinal and transverse. Corresponding reflection matrices and the symmetry properties of their off–diagonal elements.

Polar Kerr effect refers to the case when the magnetization vector is perpendicular to the sample surface. In the longitudinal and transverse geometry, the magnetization vector lies in the sample surface and is either parallel (longitudinal effect) or perpendicular (transverse effect) to the incidence plane. The symmetry considerations yield a particular form of corresponding Fresnel reflection matrices. These are provided in Table 4.1 as well.

Incident p– and s– linearly polarized waves reflected from a magnetized sample do not, in general, maintain their polarization state, as it was the case for optically isotropic samples, but instead becomes elliptically polarized (as indicated in Fig. 4.1). The transverse configuration is an exception. Here, the magnetization influences only the r_{pp} coefficient, leaving the off-diagonal elements null. The change of polarization of incident p– or s– linearly polarised waves upon reflection is, for most magneto-optical materials, relatively small and manifests itself by a rotation of the polarization plane and also by an appearance of nonzero ellipticity (cf. Fig. 4.1).

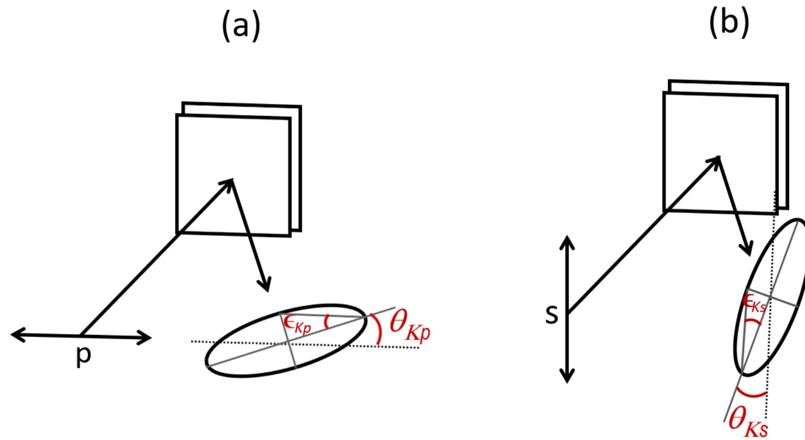

Fig. 4.1: P- (a) and s- (b) linearly polarised waves reflected from a magnetized sample. Kerr rotation θ_K and Kerr ellipticity ϵ_K as the azimuth and the angle of ellipticity of the reflected wave.

Kerr effect Φ_K is defined as the ratio of off-diagonal and diagonal elements of the reflection matrix. For p– and s– incident wave we get[1]

$$\Phi_{Kp} \equiv \frac{r_{sp}}{r_{pp}}, \qquad (4.1) \qquad\qquad \Phi_{Ks} \equiv -\frac{r_{ps}}{r_{ss}}. \qquad (4.2)$$

Geometrical interpretation of these relations can be performed similarly to the case of generalized ellipsometry (cf. Eq. (3.18) and related discussion). However, in the magneto–optics we do not employ ellipsometric angles Ψ and Δ, Eqs. (3.16-3.17). Instead, the ratio

[1]The minus sign in relation (4.2) comes from requirement $\Phi_{Kp} = \Phi_{Ks}$ that should be satisfied for the normal incidence. Refer also to the note of coordinate systems of the incident and reflected waves in Section 3.3.1.

of reflection coefficients is expressed as a function of the azimuth, Kerr rotation θ_K, and angle of ellipticity, Kerr ellipticity ϵ_K, of the reflected wave[2]. The Kerr rotation and ellipticity of p– and s– incident waves are indicated in Fig. 4.1. For example, for p–incident wave we get [1]

$$\frac{r_{sp}}{r_{pp}} = \frac{\tan\theta_{Kp} + i\tan\epsilon_{Kp}}{1 - i\tan\theta_{Kp}\tan\epsilon_{Kp}} . \tag{4.3}$$

Furthermore, in an approximation of small azimuth and ellipticity angles, that is justified for most magneto-optic materials, and with attention to the sign convention of Kerr rotation θ_K and Kerr ellipticity ϵ_K [111] we get final relations

$$\Phi_{Kp} \equiv \frac{r_{sp}}{r_{pp}} \approx \theta_{Kp} - i\epsilon_{Kp} , \tag{4.4}$$

$$\Phi_{Ks} \equiv -\frac{r_{ps}}{r_{ss}} \approx \theta_{Ks} - i\epsilon_{Ks} . \tag{4.5}$$

Formally, we can expand the Kerr rotation θ_K and Kerr ellipticity ϵ_K to the McLauren series with respect to the magnetization vector $\boldsymbol{M}$. Doing so, we can associate magneto-optical effects linear in magnetization (linear magneto–optical effects) with the second term and magneto-optical effects quadratic in magnetization (quadratic magneto–optical effects) with the third term of the expansions:

$$\theta_K(\boldsymbol{M}) = \theta_K(0) + \left(\frac{\partial\theta}{\partial M_k}\right)_{\boldsymbol{M}=0} M_k + \frac{1}{2}\left(\frac{\partial^2\theta_K}{\partial M_k \partial M_l}\right)_{\boldsymbol{M}=0} M_k M_l + \cdots \tag{4.6}$$

$$\epsilon_K(\boldsymbol{M}) = \epsilon_K(0) + \left(\frac{\partial\epsilon_K}{\partial M_k}\right)_{\boldsymbol{M}=0} M_k + \frac{1}{2}\left(\frac{\partial^2\epsilon_K}{\partial M_k \partial M_l}\right)_{\boldsymbol{M}=0} M_k M_l + \cdots \tag{4.7}$$

Faraday rotation and magnetic circular dichroism, treated in Section 2.1.2, represent linear magneto–optical effects, whereas magnetic linear birefringence and magnetic linear dichroism (Voigt effect) belong to quadratic magneto–optical effects. These effects are observed as the light propagates through a magneto–optical medium. The linear and quadratic magneto–optical effects in reflection will be discussed in the forthcoming Sections. The first terms of expansion, $\theta_K(0)$ and $\epsilon_K(0)$, vanish for optically isotropic samples. If the sample is optically anisotropic crystal, evaluation of magneto–optical effects requires rather complicated calculus (refer, for example, to magneto–optical study of single–crystal orthoferrites and hexagonal ferrites by Kahn, Pershan and Remika [58]).

4.2 Instrumentation

Magneto-optical angles, rotation θ_K and ellipticity ϵ_K, observed in reflection are relatively small compared to parameters Ψ and Δ encountered in optical ellipsometry. Often, they get values of the order of $0.1°$ or lower. Therefore, modulation experimental

[2]The same approach is employed for chiroptical effects where we introduce the the azimuth (optical rotation) and angle of ellipticity (circular dichroism).

techniques coupled with synchronous detection are usually used for their measurements. These were already mentioned in Section 3.2 and are based on modulation of the light polarization state. Modulation of ellipticity with use of photo-elastic modulator [112] or of azimuth using Faraday cells [113, 114, 115, 116] or Pockels cells [117, 118, 119] are common. External magnetic fields with induction up to several Teslas required for saturation of sample magnetization are provided by an electromagnet or by superconducting magnets. Optical cryostats for low-temperature magneto–optical measurements are commercially available as well.

Magneto-optical spectra presented in this work were recorded at room temperature with customized azimuth modulated null ellipsometer[3]. As it was demonstrated by Aspnes [120] the improvement in precision by which the null settings of polarizer and analyzer can be determined using Faraday cell azimuth modulation reaches an order of magnitude to 0.001°. Moreover, by applying a DC current to the Faraday cells, a non-zero average rotation of the plane of polarization can also be obtained [116]. Since a change in the DC current is equivalent to a mechanical rotation of the polarizer element, a null ellipsometer can be constructed without moving parts. In our case, two Faraday cells, one with ac current for modulation and the other with dc signal for nulling, were employed [121].

Provided that the modulation amplitude or the source intensity can be made sufficiently large to ensure shot-noise limited operation, the Faraday-cell-modulated ellipsometer is capable of obtaining the highest precision of any present configurations [120]. Null systems are also inherently insensitive to source and detector characteristics, and therefore, can also achieve high accuracy. The principal disadvantage is the sensitivity of attainable precision to even a small amount of stray light or detector dark current, a consequence of operation at low light levels.

Technical details, as well as measurement procedures of the customized azimuth-modulated null ellipsometer used in this study, are available in [122]. For other sources covering alternative instrumentations in magneto-optics refer, for example, to Refs. [123, 17].

4.3 Single interface

Let us consider the most simple case of light reflection from a magnetized optically opaque sample, theoretically treated as a reflection from a single interface ambient/sample between two semi-infinitive homogeneous media. Derivation of the reflection matrix coefficients r_{pp}, r_{ss}, r_{ps}, and r_{sp} requires the knowledge of the proper modes in both media. These are then connected through the field boundary conditions on the interface.

In optically isotropic ambient (usually air), the proper polarization of the incident and reflected waves can be selected arbitrarily. We choose s– and p– linearly polarized waves (cf. Fig. 3.4b). On the other hand, proper modes propagating in a magnetized sample depend on its electric permittivity ε and are solutions of the wave equation (2.25).

[3]For the principle of nulling ellipsometry refer to Section 3.2.

Visnovsky solved this equation for the general form of the electric permittivity tensor

$$\varepsilon = \begin{bmatrix} \varepsilon_{11} & \varepsilon_{12} & \varepsilon_{13} \\ \varepsilon_{21} & \varepsilon_{22} & \varepsilon_{23} \\ \varepsilon_{31} & \varepsilon_{32} & \varepsilon_{33} \end{bmatrix}, \tag{4.8}$$

thus, accounting for an arbitrary orientation of magnetization vector $\boldsymbol{M}$ [124].

Considering the Cartesian axes oriented in a manner to null $\bar{N}_x$ component of the reduced refractive index $\bar{\boldsymbol{N}}$, defined by Eq. (2.36), which is equivalent with setting the plane of incidence into the yz-plane[4], the wave equation becomes

$$\begin{bmatrix} \varepsilon_{11} - \bar{N}_y^2 - \bar{N}_z^2 & \varepsilon_{12} & \varepsilon_{13} \\ \varepsilon_{21} & \varepsilon_{22} - \bar{N}_z^2 & \varepsilon_{23} + \bar{N}_y \bar{N}_z \\ \varepsilon_{31} & \varepsilon_{zy} + \bar{N}_y \bar{N}_z & \varepsilon_{33} - \bar{N}_y^2 \end{bmatrix} \begin{bmatrix} E_{0x} \\ E_{0y} \\ E_{0z} \end{bmatrix} = 0, \tag{4.9}$$

or more concisely $\boldsymbol{Z} \cdot \boldsymbol{E_0} = 0$. The proper numbers, $\bar{N}_z$ components of the reduced refraction index $\bar{\boldsymbol{N}}$, are the solutions of the characteristic equation, $\det \boldsymbol{Z} = 0$, that is

$$\begin{aligned} & \varepsilon_{33}\bar{N}_z^4 + (\varepsilon_{23} + \varepsilon_{32})\bar{N}_y \bar{N}_z^3 \\ - & [\varepsilon_{22}(\varepsilon_{33} - \bar{N}_y^2) + \varepsilon_{33}(\varepsilon_{11} - \bar{N}_y^2) - \varepsilon_{13}\varepsilon_{31} - \varepsilon_{23}\varepsilon_{32}]\bar{N}_z^2 \\ - & [(\varepsilon_{11} - \bar{N}_y^2)(\varepsilon_{23} + \varepsilon_{32}) - \varepsilon_{12}\varepsilon_{31} - \varepsilon_{21}\varepsilon_{13}]\bar{N}_y \bar{N}_z \\ + & \varepsilon_{22}[(\varepsilon_{11} - \bar{N}_y^2)(\varepsilon_{33} - \bar{N}_y^2) - \varepsilon_{13}\varepsilon_{31}] - \varepsilon_{12}\varepsilon_{21}(\varepsilon_{33} - \bar{N}_y^2) \\ - & \varepsilon_{23}\varepsilon_{32}(\varepsilon_{11} - \bar{N}_y^2) + \varepsilon_{12}\varepsilon_{23}\varepsilon_{31} + \varepsilon_{13}\varepsilon_{21}\varepsilon_{32} = 0\,. \end{aligned} \tag{4.10}$$

When the determined proper numbers $\bar{N}_z$ are inserted back into Eq. (4.9) the proper polarizations are eventually identified[5]. Final analytical expressions of diagonal and off–diagonal elements of Jones reflection matrix, derived by Visnovsky [124], are presented in Appendix A.

This general treatment of light reflection from the single interface covers (i) oblique and normal incidence (ii) arbitrary orientation of magnetization vector with respect to the plane of incidence and sample surface (iii) magneto–optical effects of linear and higher orders in magnetization, and (iv) optically isotropic and anisotropic samples. In particular, linear magneto–optical effects in the polar and longitudinal configurations together with the quadratic magneto–optical effects in reflection are introduced in more detail in the following sections.

4.3.1 Polar Kerr configuration

The optically isotropic sample that is magnetized perpendicularly to the sample surface, along z–axis of the coordinate system, as indicated in Tab. 4.1 (the polar configu-

[4]This can be done without loss of generality because the permittivity tensor is considered in its general form.

[5]The component $\bar{N}_y$ is a real parameter that relates to the incident angle φ by the Snell's law, $\bar{N}_y = N_0 \sin\varphi$, where N_z is refractive index of an ambient.

ration) is described by electric permittivity tensor

$$\boldsymbol{\varepsilon_p} = \begin{bmatrix} \varepsilon_1 & -i\varepsilon_2 & 0 \\ i\varepsilon_2 & \varepsilon_1 & 0 \\ 0 & 0 & \varepsilon_1 \end{bmatrix} . \tag{4.11}$$

It is worth mentioning that this corresponds to the relation (2.50) of permittivity tensor in the Faraday configuration. However, here only terms linear in magnetization are considered. Hence, all diagonal elements, $\varepsilon_1 = \varepsilon_1' - i\varepsilon_1''$, equal each other. Moreover, we applied so-called Krinchik notation [125] for off–diagonal tensor elements setting $\varepsilon_{12} = -i\varepsilon_2$, where $\varepsilon_2 = \varepsilon_2' - i\varepsilon_2''$. This notation points out the fact that light absorption, that is expressed by *imaginary* part of diagonal elements, is, in the case of off-diagonal elements, expressed by its *real* part. On the other hand, the real part of diagonal and the imaginary part of off–diagonal elements relate to the dispersion of a material (for more details refer to Section 2.1.2). Hence, considering the Krinchik notation we conveniently associate the real parts ε_1' and ε_2' with light dispersion and the imaginary parts ε_1'' and ε_2'' with light absorption in a magnetized material.

Solution of characteristic equation (4.10) yields in the particular case of polar configuration two refractive indices (proper numbers)

$$\bar{N}_z^{\pm} = \sqrt{\varepsilon_1 - \bar{N}_y^2}\sqrt{1 \pm \frac{\varepsilon_2}{\sqrt{\varepsilon_1(\varepsilon_1 - \bar{N}_y^2)}}} . \tag{4.12}$$

These inserted into the wave equation (4.9) give proper polarizations

$$\boldsymbol{e}_{\pm} = \begin{bmatrix} -\mathrm{i}\varepsilon_2(\varepsilon_1 - \bar{N}_y^2) \\ -(\varepsilon_1 - \bar{N}_y^2)(\varepsilon_1 - \bar{N}_y^2 - \bar{N}_z^{\pm 2}) \\ \bar{N}_y \bar{N}_z^{\pm}(\varepsilon_1 - \bar{N}_y^2 - \bar{N}_z^{\pm 2}) \end{bmatrix} , \tag{4.13}$$

that are for oblique incidence elliptical.

In the linear approximation the diagonal elements r_{pp} and r_{ss} of the reflection matrix get the same form as obtained by Fresnel for an optically isotropic sample (Eqs. (3.21) and (3.22)). Nevertheless, the off–diagonal elements becomes non–null and are expressed by (cf. Appendix A)

$$r_{sp} = r_{ps} = \frac{-i\varepsilon_2 N_0 \cos\varphi}{\sqrt{\varepsilon_1}(N_0\cos\varphi + \sqrt{\varepsilon_1}\cos\varphi_t)(N_0\cos\varphi_t + \sqrt{\varepsilon_1}\cos\varphi)} , \tag{4.14}$$

where

$$\cos\varphi_t = \sqrt{1 - \frac{\bar{N}_y^2}{\varepsilon_1}} . \tag{4.15}$$

Knowing reflection matrix, the polar Kerr effect Φ_K for p– and s– incident waves can be calculated by the relations (4.1) and (4.2).

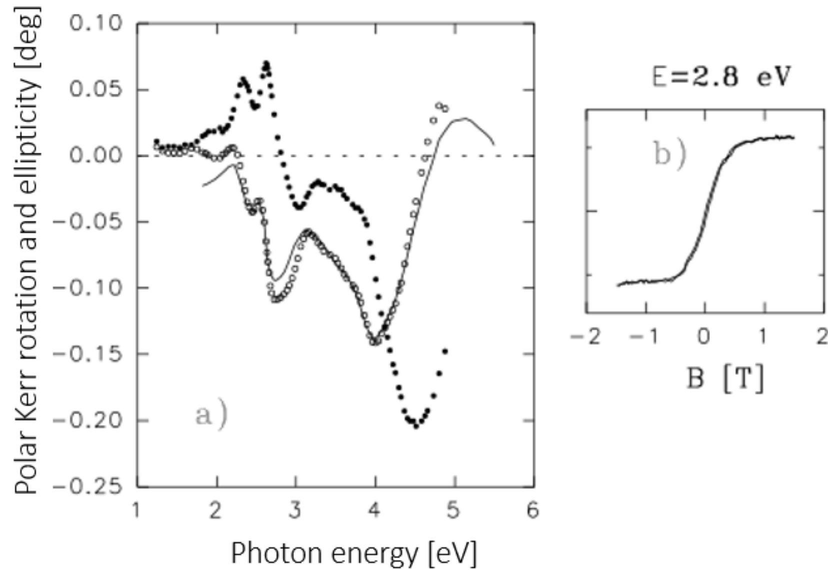

Fig. 4.2: Polar Kerr rotation (open circles) and ellipticity (full circles) measured on (111) facet of $NiFe_2O_4$ monocrystal. Polar Kerr rotation (solid line) reported by Kahn [58] is indicated as well (a). Magnetic hysteresis loop of the monocrystal recorded by the polar Kerr rotation. Monochromatic incident light with photon energy of 2.8 eV was employed (b). Modified from Mistrík [126].

In the case of the normal incidence, the proper modes become left and right circularly polarized waves, identically as in the Faraday configuration (cf. Section 2.1.2). It can be further shown (see, for example, [20]) that the normal–incidence polar Kerr effect get a simple form

$$\Phi_K = \theta_K - i\epsilon_K = \frac{i\varepsilon_2}{\sqrt{\varepsilon_1}(\varepsilon_1 - 1)} \,. \tag{4.16}$$

Comparing this relation to Eqs. (2.55) and (2.56) we see that for moderate absorption the Kerr rotation θ_K corresponds to MCD and the Kerr ellipticity ϵ_K to the Faraday rotation. The value of the Kerr effect in reflection compared to the corresponding Faraday effect in the transmission is smaller. Nevertheless, the Kerr effect serves as a powerful tool for the investigation of opaque samples. As an example, we present in Fig. 4.2 the nearly–normal incidence spectra of polar Kerr rotation and ellipticity measured on (111) facet of $NiFe_2O_4$ monocrystal together with polar Kerr rotation hysteresis loop recorded with a photon energy of 2.8 eV.

It is worthy of notice that the polar Kerr effect can be enhanced when the ambient (air) is replaced by a transparent medium with a higher refractive index. This is, for example, the case when an opaque magneto–optical film is measured from the side of a transparent substrate with refractive index n_s. Then polar Kerr rotation and ellipticity in the relation (4.16) are to be multiplied by the value of n_s [17].

Magneto–optical constants of nickel ferrite determined by analytic formula

Experimental spectra of normal–incidence[6] polar Kerr rotation θ_K and ellipticity ϵ_K recorded on a single interface can be conveniently employed for determination of magneto–optical constants of a material. Considering $\sqrt{\varepsilon_1} = n - i\kappa$ and assuming that refractive index n and extinction coefficient κ of the material are already known (for example from ellipsometry measurements), relation (4.16) can be inverted to get an analytical expression of real and imaginary parts of ε_2 as a function of optical constants and experimental values of θ_K and ϵ_K

$$\varepsilon_2' = -(D\theta_K + C\epsilon_K)\,, \tag{4.17}$$
$$\varepsilon_2'' = -(D\epsilon_K - C\theta_K)\,, \tag{4.18}$$

where

$$C = n(n^2 - 3k^2 - 1)\,, \qquad \text{and} \qquad D = k(3n^2 - k^2 - 1)\,.$$

This analytical approach is available only for the single interface, and we demonstrate its application to the case of bulk Ni ferrite single crystal. Its optical constants were obtained by spectroscopic ellipsometry (cf. Section 3.3.1) and experimental magneto–optical polar Kerr spectra are presented in Fig. 4.2. Employing Eqs. (4.17) and (4.18) we easily

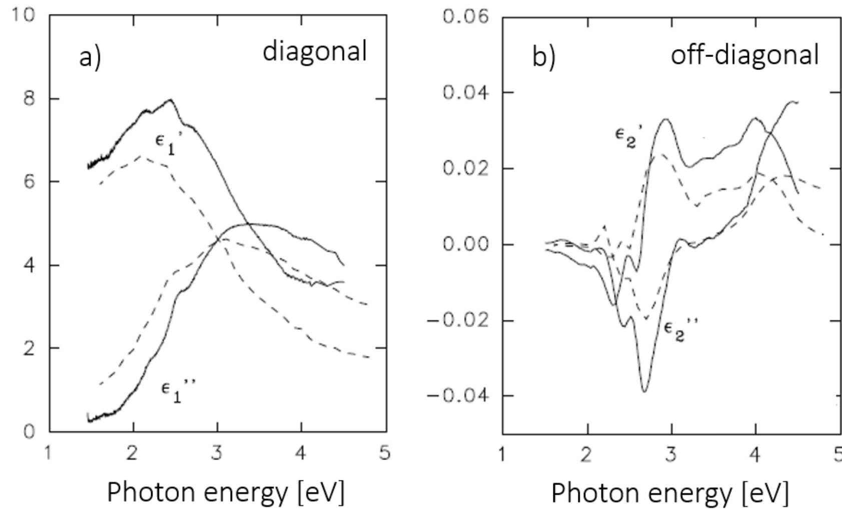

Fig. 4.3: Spectra of optical constants, in terms of real and imaginary parts of diagonal permittivity element ε_1, a), and magneto–optical constants, in terms of real and imaginary parts of off-diagonal permittivity element ε_2, b), of bulk monocrystalline $NiFe_2O_4$. Spectroscopic ellipsometry complemented with complex polar Kerr effect and single interface analytic formula was employed. Broken lines correspond to the data obtained by Krinchik et al. [127] on a $NiFe_2O_4$ polycrystalline sample. Modified from Mistrík [126].

[6]Experimentally feasible is nearly–normal incidence with an incidence angle of about 5°.

get real and imaginary parts of off–diagonal tensor element ε_2. Spectra of the real and imaginary parts of optical (in terms of ε_1) and magneto–optical (in terms of ε_2) constants of Ni ferrite are presented in Fig. 4.3.

Precise determination and knowledge of materials optical and magneto–optical constants is one of the important requirements for modeling and design of new high–performance magneto–optical devices. Nevertheless, it should be noted that the interpretation of observed experimental magneto–optical spectral features by microscopic models is, in many cases, uneasy [21, 20]. For example, in the case of ferrites, the assignment of electron transitions by calculated molecular orbital spectra is often ambiguous, also due to uncertain line shape analysis. Even though great progress has been made since the pioneering works of Clogston[128] and Wood [129]. On the other hand, magneto–optical constants determined from experimental spectra on high-quality samples give the possibility to tune ab–initio theoretical calculations and ultimately facilitate prediction of new materials with high magneto–optical response.

Beilby overlayer and its curing

Bulk samples that were intentionally surface treated (for example, by polishing) to achieve optical surface quality often manifest surface damaged layer accumulating structural and other defects. This was already mentioned previously, pointing out the limitation of the single interface approximation in the characterization of bulk samples by ellipsometry (cf. Section 3.3.1). A similar manifestation of the so-called Beilby overlayer can be encountered also in magneto–optics, and here we demonstrate its particular case. Bulk polycrystalline Ni ferrite sample was sintered from a powder mixture of high purity

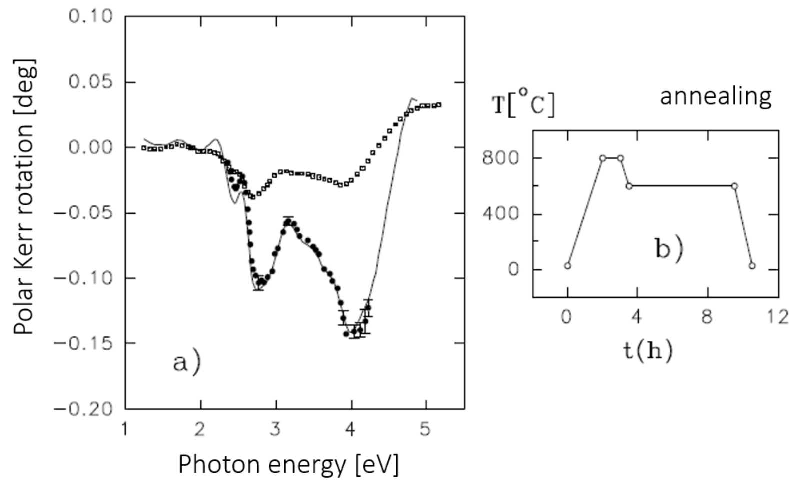

Fig. 4.4: Polar Kerr rotation spectra measured on polycrystalline $NiFe_2O_4$ sample with mechanically polished surface before (open circles) and after (full circles) annealing a). Spectra recorded on native (111) facet of monocrystalline $NiFe_2O_4$ is provided as well (solid line) a). Temporal profile of annealing temperature b). Modified from Mistrík [126].

oxides. Its surface was afterward mechanically polished to optical quality. Polar Kerr rotation spectrum recorded on this surface is compared with that of $NiFe_2O_4$ monocrystalline (111) native facet in Fig. 4.4a). Clear diminution of polar Kerr rotation amplitude of polycrystalline with respect to monocrystalline sample is to be attributed to their different surface quality. Surface damaged layer of polycrystalline sample due to the polishing displays modified optical and magneto–optical constants in several tents of micrometers in depth beneath the surface. Furthermore, closer examination of the polar Kerr rotation difference can be correlated with the spectral dependency of light penetration depth of Ni ferrite cf. Fig. 4.10. This damaged overlayer can be removed by chemical etching or by thermal annealing and, the latter was applied to the studied sample. The sample was thermally treated in an oxygen atmosphere with the temperature cycle presented in 4.4b). Remeasured polar Kerr rotation on so cured sample surface is for comparison added to the plot in Fig. 4.4b), as well. Process of annealing recovered polar Kerr rotation values to nearly identical to those recorded on the monocrystalline sample surface.

4.3.2 Longitudinal and transverse Kerr configurations

In the longitudinal configuration magnetization vector $\boldsymbol{M}$ lies along intersection of sample surface and incidence plane (cf. Tab. 4.1). Electric permittivity tensor gets, in this case, form

$$\boldsymbol{\varepsilon_l} = \begin{bmatrix} \varepsilon_1 & 0 & -i\varepsilon_2 \\ 0 & \varepsilon_1 & 0 \\ i\varepsilon_2 & 0 & \varepsilon_1 \end{bmatrix} . \tag{4.19}$$

Here, only optically isotropic samples and terms independent, ε_1, or linearly dependent, ε_2, on magnetization were considered. Solution of the characteristic equation (4.10) gives two refractive indices

$$\bar{N}_z^{\pm 2} = \varepsilon_1 - \bar{N}_y^2 - \frac{\varepsilon_2}{2\varepsilon_1}\left[\pm\sqrt{4\varepsilon_1\bar{N}_y^2 + \varepsilon_2^2} - \varepsilon_2\right], \tag{4.20}$$

and, when solely linear magneto-optical effect are to be regarded, we can make simplification

$$\bar{N}_z^{\pm 2} = \varepsilon_1 - \bar{N}_y^2 \pm \frac{\varepsilon_2}{2\varepsilon_1}\sqrt{4\varepsilon_1\bar{N}_y^2}\,. \tag{4.21}$$

Proper elliptical polarizations are then expressed by

$$\boldsymbol{e}_j = \begin{bmatrix} -\mathrm{i}\varepsilon_2\bar{N}_y\bar{N}_z^{\pm} \\ (\varepsilon_1 - \bar{N}_y^2)(\varepsilon_1 - \bar{N}_y^2 - \bar{N}_z^{\pm 2}) - \varepsilon_2^2 \\ -\bar{N}_y\bar{N}_z^{\pm}(\varepsilon_1 - \bar{N}_y^2 - \bar{N}_z^{\pm 2}) \end{bmatrix} . \tag{4.22}$$

Inserting $\bar{N}_z^{\pm}$ into (A.7) and (A.8) we get off–diagonal elements of reflection matrix

$$r_{sp} = -r_{ps} = \frac{-i\varepsilon_2 N_0^2 \sin\varphi\cos\varphi}{\varepsilon_1\cos\varphi_t(N_0\cos\varphi + \sqrt{\varepsilon_1}\cos\varphi_t)(N_0\cos\varphi_t + \sqrt{\varepsilon_1}\cos\varphi)}. \tag{4.23}$$

Diagonal elements are identical with the Fresnel relations (3.21) and (3.22) of a single interface between two media with refractive indices N_0 and $\sqrt{\varepsilon_1}$. The off-diagonal elements (4.23) vanish for normal incidence, and therefore, the linear longitudinal effect also disappears. This is demonstrated in Fig. 4.5a, where the longitudinal Kerr rotation θ_K and ellipticity ϵ_K for both polarizations s– and p– are calculated for a single interface air/Fe as a function of incidence angle. Spectral dependence of these variables together with theoretical predictions are presented in Fig. 4.5b for incidence angle 65°.

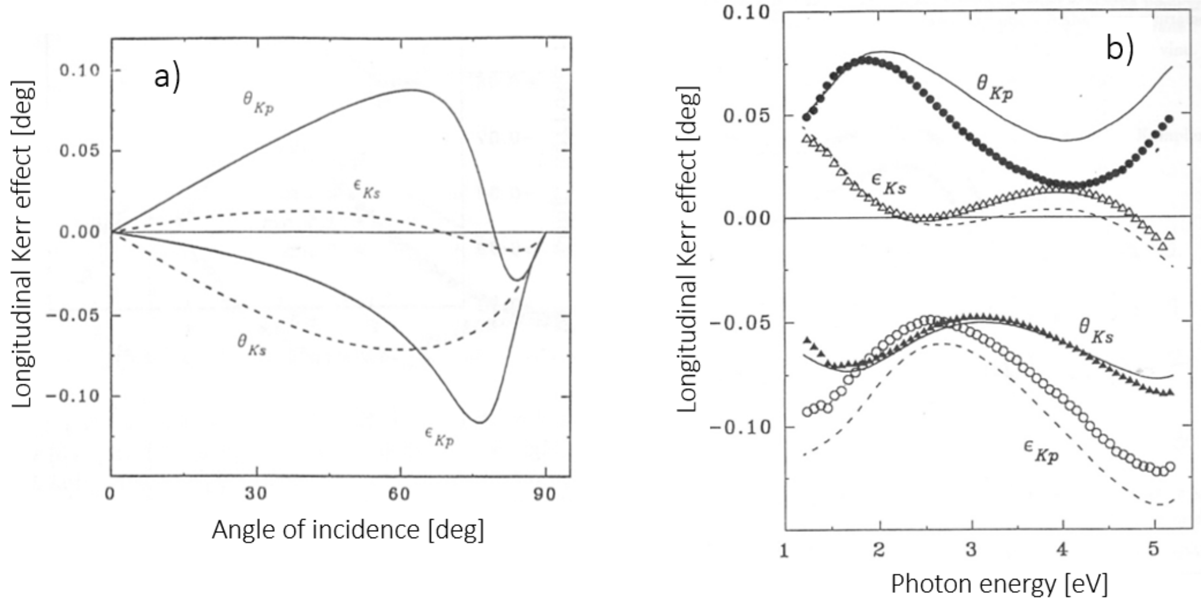

Fig. 4.5: Complex longitudinal Kerr effect calculated for single interface air/Fe and photon energy of 1.96 eV as a function of incidence angle a). Optical and magneto–optical constants are taken from [130]. Spectral dependence of complex longitudinal Kerr effect (symbols) recorded on bulk monocrystalline Fe with the angle of incidence of 65°. Theoretical predictions (solid and broken lines) are provided as well b). Modified from Mistrík [111].

It is worth mentioning that, although the linear longitudinal effect disappears for normal incidence, it is not the case for the quadratic magneto–optical effect. This can be anticipated from the discussion of the quadratic Voigt effect observed in transmission (cf. Section 2.1.2). Phenomenon analogous with the Voigt effect, but in reflected light, is treated in the next Section.

In the transverse configuration, the magnetization vector lies in the sample surface perpendicularly oriented with respect to the incidence plane (cf. Tab. 4.1). Corresponding permittivity tensor gets the form

$$\boldsymbol{\varepsilon_t} = \begin{bmatrix} \varepsilon_1 & 0 & 0 \\ 0 & \varepsilon_1 & -i\varepsilon_2 \\ 0 & i\varepsilon_2 & \varepsilon_1 \end{bmatrix} . \tag{4.24}$$

Here, the magnetization vector $\boldsymbol{M}$ influences only r_{pp} element. The off-diagonal elements are null. Hence, the reflection matrix is diagonal and linearly polarised s– and p– waves are proper modes. Transverse linear magneto–optical effects disappear for normal incidence as well. For more details, we refer the reader to [131].

4.3.3 Quadratic magneto-optical effects in reflection

Phenomenological description of quadratic magneto–optical effects in crystals with cubic symmetry requires considering the McLauren expansion of the electric permittivity (cf. Eq. 2.44)) up to its third term, including the quadratic magneto–optical tensor G_{ijkl}. This was already mentioned in the case of Voigt effect in Section 2.1.2. Quadratic magneto–optical effects in reflection were treated by Visnovsky [124] and Postava [132, 123], and we follow their approach here.

Let's consider simplified form of electric permittivity tensor for polar configuration

$$\boldsymbol{\varepsilon} = \begin{bmatrix} \varepsilon_1 + \varepsilon_1 f Q^2 & -\mathrm{i}\varepsilon_1 Q & 0 \\ \mathrm{i}\varepsilon_1 Q & \varepsilon_1 + \varepsilon_1 f Q^2 & 0 \\ 0 & 0 & \varepsilon_1 \end{bmatrix}, \tag{4.25}$$

where linear, Q, and quadratic, f, magneto–optical constant are introduced [133]. These are related to the magneto–optical tensors K_{ijk} and G_{ijkl} by relations

$$K_{123} M = -\mathrm{i} Q \varepsilon_1 \,, \tag{4.26}$$

$$(G_{12} - G_{11}) M^2 = f Q^2 \varepsilon_1 \,. \tag{4.27}$$

From equations (4.27) it is evident that two complex parameters G_{12} and G_{11} are replaced with one complex parameter f. Furthermore, the parameter G_{44} does not manifest in the polar configuration, and therefore, is not covered by the parameter f. General treatment of quadratic magneto–optical effects with arbitrary orientation of magnetization vector $\boldsymbol{M}$ is algebraically cumbersome. Therefore, we will limit ourselves to the case of the in-plane magnetization (magnetization vector lies in the sample surface).
Permittivity tensor gets in this case the form

$$\boldsymbol{\varepsilon} = \varepsilon_1 \begin{bmatrix} 1 + f Q_L^2 & -f Q_L Q_T & \mathrm{i} Q_L \\ -f Q_L Q_T & 1 + f Q_T^2 & -\mathrm{i} Q_L \\ -\mathrm{i} Q_L & \mathrm{i} Q_T & 1 + f Q_L^2 + f Q_T^2 \end{bmatrix}, \tag{4.28}$$

where linear longitudinal Q_L and transverzal Q_T magneto–optical constants are defined by

$$Q_L = Q \cos\psi \,, \tag{4.29}$$

$$Q_T = Q \sin\psi \,, \tag{4.30}$$

and meaning of the angle ψ follows from Fig 4.6. The longitudinal magneto–optical constant Q_L is then related to the magnetization component $M_L = M \cos\psi$ and the

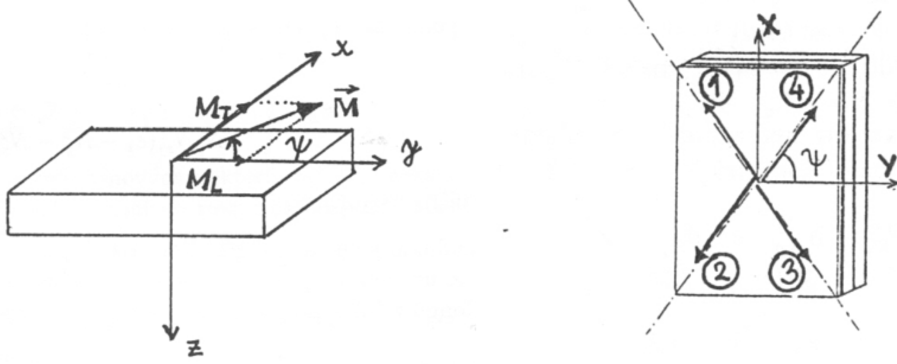

Fig. 4.6: In–plane magnetization $\boldsymbol{M}$ and its longitudinal M_L and transversal M_T component (left). Four distinct orientations of the magnetization vector $\boldsymbol{M}$ that enable separation of linear and quadratic magneto–optical contributions (right).

transversal magneto–optical constant Q_T to the component $M_T = M \sin\psi$. Inserting tensor elements (4.28) into Eqs. (A.1-A.8) and considering only small angle of incidence (where $\sin\varphi \approx \varphi$ is valid) we get for reflection matrix elements relations

$$r_{ss} = \frac{\sqrt{\varepsilon_0}-\sqrt{\varepsilon_1}}{\sqrt{\varepsilon_0}+\sqrt{\varepsilon_1}} + Q_L^2 \frac{\sqrt{\varepsilon_0}\sqrt{\varepsilon_1}(1-f)}{\left(\sqrt{\varepsilon_0}+\sqrt{\varepsilon_1}\right)^2}\,, \tag{4.31}$$

$$r_{pp} = \frac{\sqrt{\varepsilon_1}-\sqrt{\varepsilon_0}}{\sqrt{\varepsilon_0}+\sqrt{\varepsilon_1}} + 2\mathrm{i}Q_T \frac{\varepsilon_0\varphi}{\left(\sqrt{\varepsilon_0}+\sqrt{\varepsilon_1}\right)^2} - Q_T^2 \frac{\sqrt{\varepsilon_0}\sqrt{\varepsilon_1}(1-f)}{\left(\sqrt{\varepsilon_0}+\sqrt{\varepsilon_1}\right)^2}\,, \tag{4.32}$$

$$r_{sp} = -r_{ps} = \mathrm{i}Q_L \frac{\varepsilon_0\varphi}{\left(\sqrt{\varepsilon_0}+\sqrt{\varepsilon_1}\right)^2} - Q_L Q_T \frac{\sqrt{\varepsilon_0}\sqrt{\varepsilon_1}(1-f)}{\left(\sqrt{\varepsilon_0}+\sqrt{\varepsilon_1}\right)^2}\,, \tag{4.33}$$

where $\sqrt{\varepsilon_0}$ is refractive index of ambient medium. The reflection matrix is expressed to the second order in magnetization.

In the first term of r_{ss}, Eq. (4.31), and r_{pp}, Eq. (4.32), we recognize the Fresnel relations for nearly normal incidence. For longitudinal configuration $Q_L = Q = -\frac{\varepsilon_2}{\varepsilon_1}$ and it is straightforward to verify that the first term in r_{ps}, Eq. (4.33), is identical with off-diagonal longitudinal reflection matrix element (4.23) calculated in linear approximation for nearly normal incidence.

From definition of magneto–optical effects Eqs. (4.1, 4.2) we get complex magneto–optical angles

$$\Phi_{Kp} = -\Phi_{Ks} = -\mathrm{i}Q_L \frac{\varepsilon_0\varphi}{\varepsilon_0-\varepsilon_1} + Q_L Q_T \frac{\sqrt{\varepsilon_0}\sqrt{\varepsilon_1}(1-f)}{\varepsilon_0-\varepsilon_1}\,, \tag{4.34}$$

that can be split into linear and quadratic contributions

$$\Phi_K = (\theta_K - \mathrm{i}\epsilon_K) + \left(\hat{\theta}_K - \mathrm{i}\hat{\epsilon}_K\right)\,, \tag{4.35}$$

where

$$\theta_K - \mathrm{i}\epsilon_K = \pm \mathrm{i} Q_L \frac{\varepsilon_1 \varphi}{\varepsilon_1 - \varepsilon_2}\,, \tag{4.36}$$

$$\hat{\theta}_K - \mathrm{i}\hat{\epsilon}_K = \pm Q_L Q_T \frac{\sqrt{\varepsilon_1}\sqrt{\varepsilon_2}(1-f)}{\varepsilon_1 - \varepsilon_2}\,. \tag{4.37}$$

The terms $(\theta_K - \mathrm{i}\epsilon_K)$ present linear and $\left(\hat{\theta}_K - \mathrm{i}\hat{\epsilon}_K\right)$ quadratic contribution to the Kerr rotation and ellipticity. Positive sign on the right hand side of the equations (4.36) and (4.37) belongs to p–polarised and negative sign to s–polarised incident wave. This yields following relations

$$\theta_{Ks} = -\theta_{Kp}\,, \tag{4.38}$$

$$\epsilon_{Ks} = -\epsilon_{Kp}\,, \tag{4.39}$$

$$\hat{\theta}_{Ks} = -\hat{\theta}_{Kp}\,, \tag{4.40}$$

$$\hat{\epsilon}_{Ks} = -\hat{\epsilon}_{Kp}\,. \tag{4.41}$$

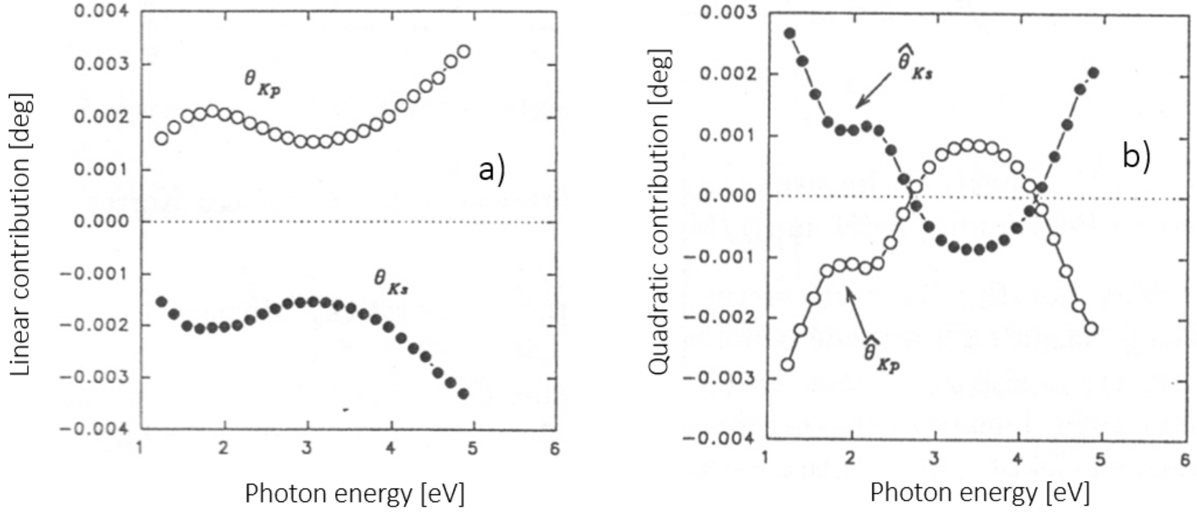

Fig. 4.7: Linear a) and quadratic b) contributions to the Kerr rotation and ellipticity determined from nearly–normal incidence measurements performed on bulk monocrystalline Fe sample. Modified from Mistrík [111].

Linear and quadratic contributions can be obtained experimentally when magneto–optical effect is recorded in four selected orientations of magnetization vector as indicated in Fig4.6b. Following this approach, Mistrik [111] obtained spectra of linear and quadratic magneto–optical contributions on bulk monocrystalline Fe sample. These are presented in Fig. 4.7.

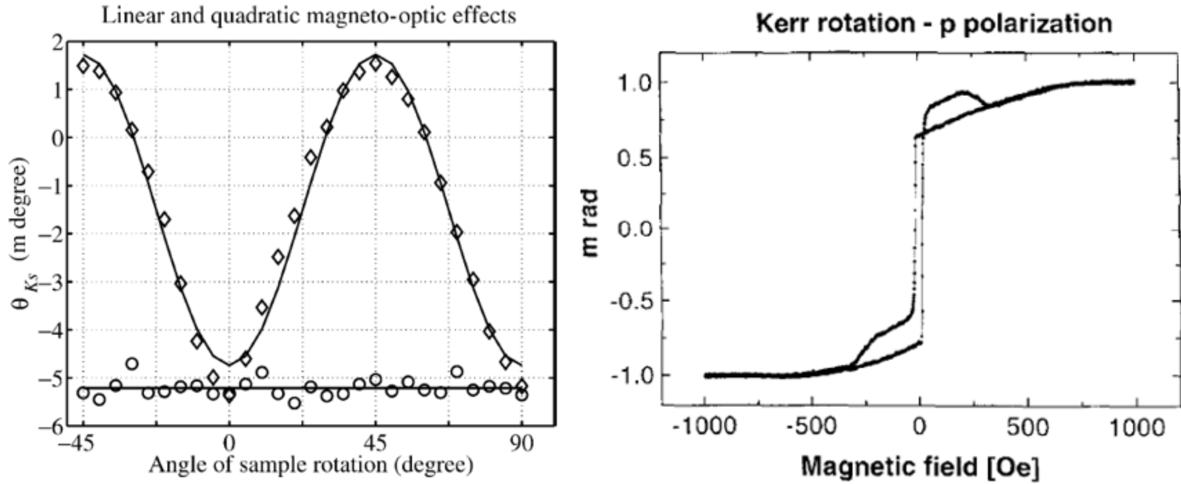

Fig. 4.8: Linear (circles) and quadratic (diamonds) magneto-optic effects measured at a Fe layer as a function of crystal rotation at nearly–normal incidence and in–plane magnetization (left, reprinted from [134]). Magnetic hysteresis loop observed for in–plane magnetic field along Fe [110] hard axis demonstrating influence of quadratic contributions in magneto–optical magnetometry (right, reprinted from [123]).

Further investigations of quadratic magneto–optical effects in cubic crystals were carried out for example by Postava et al. [28, 135, 29, 26] and Hamrle et al. [27, 136, 137] where in the latter case ab–initio calculations were presented as well. Considering all parameters of quadratic magneto–optical tensor of a cubic crystal (G_{11}, G_{22} and G_{44}), description of anisotropy of quadratic magneto–optical effect in reflection and with in-plane magnetization can be done analogously with the Voigt effect in transmission (cf. Eqs. (2.61-2.64)). Therefore, when the sample is rotating with a fixed direction of an external magnetic field, the quadratic magneto–optical contribution oscillates, while the linear contribution is constant (cf. Fig. 4.8a). This enhanced sensitivity of quadratic MO effects can be used for the crystallographic characterization of cubic crystals. On the other hand, as pointed out by Postava[123], quadratic effects encountered in magneto–optical magnetometry may lead to misinterpretation of hysteresis loops because of their quadratic (even) dependence on the magnetization (cf. Fig. 4.8b).

4.4 Single layer

Magneto–optical effect of a thin magnetized layer sandwiched between two semi-infinite media (ambient and substrate) can be expressed analytically for various magneto–optical configurations in both reflection and transmission geometries (see, for example, [138]). Solutions of the wave equation derived for all three media (ambient, layer, and substrate) independently are matched up by boundary conditions. That leads to reflection

or transmission coefficients and further to magneto-optical quantities.

Here we discuss in more detail the normal incidence polar Kerr effect on Ni ferrite single layers. This magnetic oxide is transparent in the NIR and absorbing in the UV making it an appropriate candidate for examination of so-called propagation and interface contributions of magneto–optical effect. Later in this section, we demonstrate the strength and advantages of magneto–optics as a complementary characterization tool in the quality assessment of pulsed laser deposited Sm orthoferrites films.

4.4.1 Propagation and interface contributions

Normal incidence polar Kerr effect of a single layer sandwiched between ambient and nonmagnetic substrate is derived in [139] and take form

$$\Phi_K = \theta_K - i\epsilon_K = \frac{-i\varepsilon_2(1-r_{01}^2)\left[(1+r_{12}^2e^{-2i\beta_1})(1-e^{-2i\beta_1})+4i\beta_1 r_{12}e^{-2i\beta_1})\right]}{4\varepsilon_1(1+r_{01}r_{12}e^{-2i\beta_1})(r_{01}+r_{12}e^{-2i\beta_1})}\,. \quad (4.42)$$

where $\beta_1 = N_1\frac{\omega}{c}t_1$. Reflection coefficients r_{01} and r_{12} belong to ambient/layer and layer/substrate interfaces, respectively. Thickness of the layer is t_1. N_1 is its complex refractive index ($N_1 = \sqrt{\varepsilon_1}$) and ε_2 stands for off–diagonal element of layer permittivity tensor in the polar configuration (cf. Eq. (4.11)). Complex angle of the Kerr effect, Eg. (4.42), can be rewritten as a sum of two contributions

$$\Phi_K = \Phi_K^R + \Phi_K^P, \quad (4.43)$$

where we have introduced

$$\Phi_K^R = \theta_K^R - i\epsilon_K^R = \frac{-i\varepsilon_2(1-r_{01}^2)(1+r_{12}^2e^{-2i\beta_1})(1-e^{-2i\beta_1})}{4\varepsilon_1(1+r_{01}r_{12}e^{-2i\beta_1})(r_{01}+r_{12}e^{-2i\beta_1})}\,, \quad (4.44)$$

$$\Phi_K^P = \theta_K^P - i\epsilon_K^P = \frac{-i\varepsilon_2(1-r_{01}^2)4i\beta_1 r_{12}e^{-2i\beta_1}}{4\varepsilon_1(1+r_{01}r_{12}e^{-2i\beta_1})(r_{01}+r_{12}e^{-2i\beta_1})}\,. \quad (4.45)$$

Detailed examination of these two contributions leads to the conclusion that the first term Φ_K^R corresponds predominantly to the effect of light reflection from the upper interface, id est from the surface of the layer. On the other hand, the term Φ_K^P is more related to the effect of light propagation in the layer. Indeed, with the increasing value of β_1 (increasing value of the product of layer thickness and layer absorption) the term Φ_K^P approaches zero, whereas the term Φ_K^R, reduces to the relation of polar Kerr effect derived for a single interface, Eg. (4.16). The term Φ_K^P is most important when the layer thickness is comparable or greater than the light penetration depth in the layer. In other words, multiple light reflections and interference in the film that strongly influence the magneto–optical effect are described by Φ_K^P.

As an example we present in Fig. 4.9 the two contributions θ_K^P and θ_K^R of the Kerr rotation θ_K calculated for a single layer of $NiFe_2O_4$ with a thickness of 250nm. The spectral dependence of the absorption coefficient in the available spectral range UV-VIS-NIR allows us to present most of the introduced phenomena. In the ultraviolet, nickel

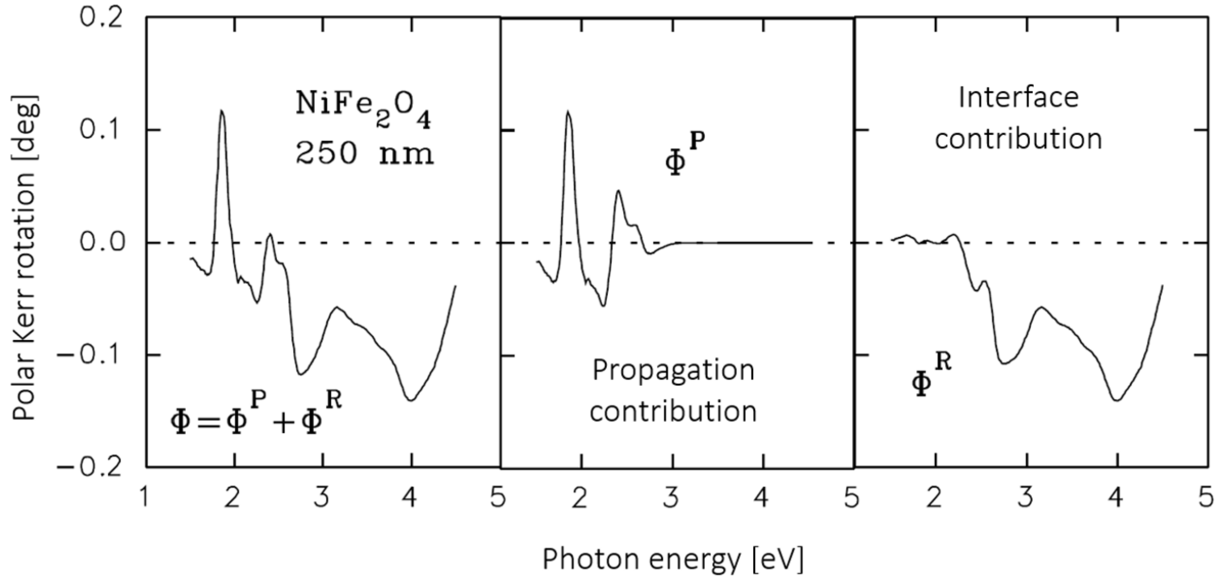

Fig. 4.9: Normal incidence polar Kerr rotation (left) calculated for 250 nm thick $NiFe_2O_4$ film deposited on fused quartz and its propagation (middle) and surface (right) contributions. Modified from Mistrík [126].

ferrite is absorbing with a penetration length of some tens of nanometers. UV radiation interacts predominantly with the air/layer interface. Consequently, in this spectral zone the contribution Φ_K^P is almost zero and Φ_K^R reproduces the value of Φ_K obtained on the bulk $NiFe_2O_4$ (see Fig. 4.2).

In the photon energy range, where bulk nickel ferrite exhibits penetration length comparable with layer thickness, i.e., for photon energies smaller than about 2.7eV, the light starts to interact with the layer/substrate interface, and the effect of propagation is no longer negligible. It even becomes more important than Φ_K^R for photon energies around 2.0 eV. In the case of a selected nickel ferrite layer, we thus identified three spectral zones: in the ultraviolet reflection from the surface of the layer dominates, in the near-infrared, it is the propagation in the layer which determines the spectrum and finally in between these two zones, in the VIS range, the two contributions are comparable. The presence and spectral localization of the propagation and reflection effects are determined by the permittivity tensor element of the given material and the layer thickness.

An illustration of the phenomena discussed is further presented in Fig. 4.10 where the spectra of the Kerr rotation calculated for a layer of $NiFe_2O_4$ with different thicknesses: 230, 250, and 270 nm are shown. We see that in the ultraviolet range, the Kerr rotation does not vary with thickness. On the other hand, in the visible and near-infrared, the spectra calculated for different thicknesses differ significantly. That is in agreement with the fact that the contribution of the propagation effects strongly depends on the thickness while the contribution of the reflection is almost independent.

As it is evident from the previous text, the light interference in a layer can be employed for an enhancement of magneto–optical response for the selected wavelength. Tha

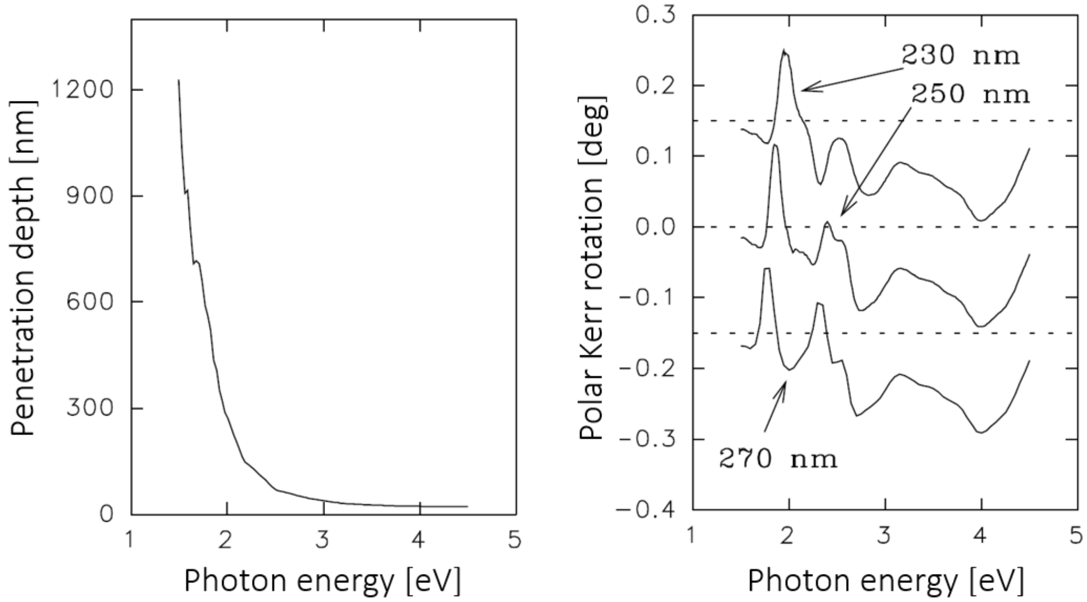

Fig. 4.10: Penetration depth of $NiFe_2O_4$ (left) and modelled normal incidence polar Kerr rotation spectra of $NiFe_2O_4$ single–layers with various thicknesses: 230, 250 and 270nm (right). Substrate is fused quartz. Modified from Mistrík [126].

is applied, for example, for magneto–optical memory discs where the enhancement is further augmented by sandwiching magneto–optical film with dielectric overlayers and incorporating an aluminum underlayer as a reflector [140, 141]. The interference effect that is strongly dependent on layer thickness gives also the possibility to use magneto–optical spectra for film thickness determination. That was demonstrated for single layers of magnetic oxides (nickel ferrite, Sm orthoferrite, and YIG) in [126, 78]. The films of Sm orthoferrites will be treated in more detail in the forthcoming section.

4.4.2 Examination of pulsed laser deposited $SmFeO_3$ films

In this section, we present magneto–optical characterization of $SmFeO_3$ polycrystalline layers deposited by pulsed laser on amorphous quartz substrates [126]. Our particular motivation is to underscore the strength of the magneto–optics among other complementary characterization tools.

Studied samples

We have prepared a set of samples, #1—#12, with different deposition parameters (see Tab. 4.2). The Nd:YAG laser operating at its third harmonic frequency (wavelength of 355 nm) generated laser pulses focused on a Sm target with spot diameter either 1mm or 2mm and fluences P_L equal to 6, 12, 15 or 18 $\mathrm{J} \cdot \mathrm{cm}^{-2}$. The rate of the shots f and the duration of a pulse $\Delta\tau$ were 10 Hz and 6 ns, respectively. Fused quartz substrates

were heated and substrate temperature varied for the different samples between 340 and 870°C. All samples were prepared under an oxygen atmosphere with a pressure equal to 80 mTorr. The $SmFeO_3$ target was sintered from iron oxides and samarium with purity better than 99.9999%. The distance between the target and the substrate was equal to 5 cm. To access both magneto–optical contribution of layer propagation and surface reflection, the deposition time was set between 30 min and 3 h. A synoptic representation of the different values of laser fluence, substrate temperature, and spot diameter for the different samples is shown in Fig. 4.11.

	deposition				**AFM**	**thickness[nm]**	
#	time	T_s[°C]	P_L[Jcm^{-2}]	spot diameter	RMS [nm]	t_{Elli}	t_{MO}
1.	1h	830	18	1 mm	115.3	234	235
2.	1h	760	15	1 mm	83.1	235	230
3.	1h	830	15	2 mm	61.9	336	320
4.	2h	830	15	2 mm	77.2	$\approx$ 1262	$\approx$ 1220
5.	30’	830	12	1 mm	36.8	189	190
6.	1h	870	6	2 mm	44.8	254	250
7.	3h	870	6	1 mm	30.4	$\approx$ 833	$\approx$ 840
8.	1h	670	18	2 mm	$\otimes$	$\otimes$	$\otimes$
9.	1h	430	15	2 mm	$\otimes$	$\otimes$	$\otimes$
10.	1h	340	12	2 mm	$\otimes$	$\otimes$	$\otimes$
11.	1h	670	12	2 mm	$\otimes$	$\otimes$	$\otimes$
12.	1h	830	12	1 mm	$\otimes$	$\otimes$	$\otimes$

Tab. 4.2: Pulsed laser deposition parameters of $SmFeO_3$ films together with their surface roughness, determined by AFM, and film thickness, obtained by spectroscopic ellipsometry and magneto–optics.

Magnetic phase formation and the Curie temperature – Faraday rotation magnetometry

As the Faraday rotation is linearly dependent on sample magnetization, recording its value while cycling external magnetic field between +1.2 T and -1.2 T provided sample hysteresis loops. The fixed photon energy of 2.1 eV, for which the samples were semi–transparent, was employed. From obtained hysteresis loops, we assessed the magnetic ordering in the $SmFeO_3$ layers. It was found that only samples #1–#7, prepared with elevated substrate temperatures ($T_s \geq 760$°C), show magnetic ordering. For deposition temperatures lower than 760°C the orthorhombic structure of $SmFeO_3$ with specific weak ferromagnetic behavior of canted spins does not form. X–Ray diffractometry consistently approved the amorphous phase of non–magnetic samples #8–#12, whereas the samples #1–#7 were found to be polycrystalline.

Comparing two selected samples, magnetically ordered sample #2 and non–magnetic sample #12, both deposited with the same substrate temperature $T_s = 760$°C, we conclude that the difference in their magnetic state is due to the difference in the laser fluences ($P_L^{\#2} = 15\,\mathrm{J \cdot cm^{-2}}$ and $P_L^{\#12} = 12\,\mathrm{J \cdot cm^{-2}}$) that were used for the samples abla-

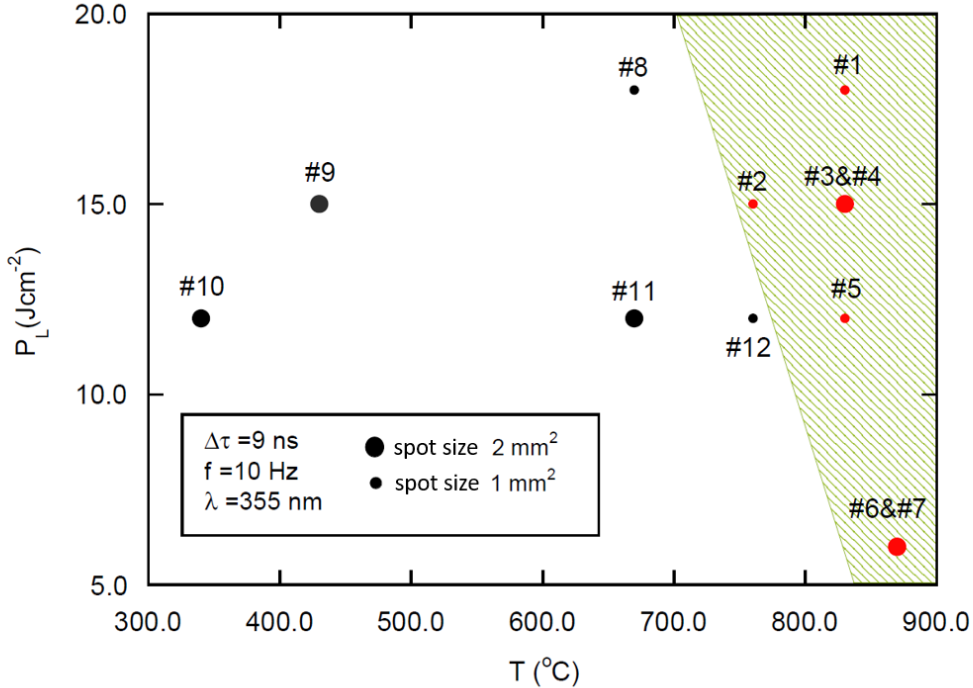

Fig. 4.11: Schematic representation of laser-ablated $SmFeO_3$ films plotted as a function of their deposition parameters, laser fluence, and deposition temperature. An estimated interval of deposition conditions where $SmFeO_3$ films show magnetic ordering is indicated by hatching. Modified from Mistrík [126].

tion. Therefore, the substrate temperature needed for magnetically ordered orthorhombic structure can be decreased by the simultaneous increase of the laser fluence. Cracuin et al. [142] presented similar phenomenon in the case of piezoelectric layer ablation of $Pb(ZrTi)O_3$. They found that ablation with high laser fluences ($\approx 26\text{J} \cdot \text{cm}^{-2}$) enables a decrease of the substrate temperature by $\approx 130°\text{C}$ while maintaining the structural and piezoelectric properties of the layers. In Fig. 4.11 the approximate range of values of the substrate temperatures and laser fluences, where the formation of high-quality Sm orthoferrite films is expected, was indicated.

The Curie temperature, which is related to the strength of the exchange interactions in a magnetic material, was considered to verify whether the magnetically ordered $SmFeO_3$ films exhibit the magnetic properties characteristic for the bulk monocrystal. For this purpose, we studied the Faraday rotation of sample #6 as a function of the temperature. The thermal variation of the Faraday rotation, measured in the temperature range between 330 and 670 K, is shown in Fig. 4.12 (middle). The value of the Faraday rotation for each temperature is determined from hysteresis loops as an average of absolute values of the Faraday rotation measured in external magnetic field maximum +1.2 T and minimum -1.2 T.

It should be noted that for temperatures $\leq$ 580K the hysteresis cycles are not saturated. In other words, for these temperatures, we observe the minor cycles (cf. Fig.

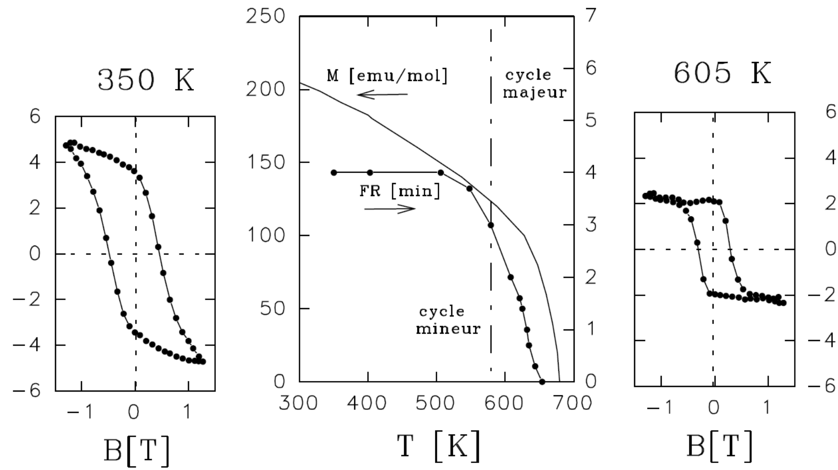

Fig. 4.12: Determination of the Curie temperature of $SmFeO_3$ film (#6) evaluating temperature dependence of its Faraday rotation (middle). Low-temperature minor hysteresis loops (left) and high-temperature major hysteresis loops (right) are presented as well. Modified from Mistrík [126].

4.12(left)). The value of the Faraday rotation obtained from these cycles then presents values reduced compared to that corresponding to sample in saturation. However, for temperatures $\geq$ 580K the hysteresis cycles show magnetic saturation, and the values of the Faraday rotation get saturated values. The thermal variation of the Faraday rotation is monotonic. For temperatures greater than 580K the Faraday rotation decreases and it becomes almost zero for the temperature 654 ± 20K. This value is in good agreement with the Curie temperature $T_c = 674$K of monocrystalline Sm orthoferrite. That demonstrates that the exchange interactions in the ablated $SmFeO_3$ thin film are comparable to that of bulk $SmFeO_3$.

Film thickness – propagation contribution of polar Kerr rotation spectra

In this section, we discuss room-temperature polar Kerr rotation spectra of layers #1–#7. In the ultraviolet, the propagation effect is negligible, and therefore, the Kerr rotation of the layers is attributed to the layer surface and corresponds with bulk. On the other hand, in the region of low photon energies, $SmFeO_3$ is (semi-)transparent, and thus, the propagation contribution strongly modifies the spectral features of the Kerr rotation of the layers compared to the massive sample. That is demonstrated in Fig. 4.13 where the experimental and the closest theoretical spectra are presented for samples #3 and #6. The corresponding spectrum of bulk $SmFeO_3$ (single interface) is presented there as well for comparison. In the calculations, we used the optical constants of Eu orthoferrite and the magneto–optical constants of Sm orthoferrite reported by Kahn et al. [58]. A relatively good agreement between the experimental and theoretical spectra obtained for all the samples in the whole spectral range indicates the formation of $SmFeO_3$

in the layers, which has already been confirmed by X–Ray analyzes. From magneto-optical spectroscopic studies, we can further confirm the presence of anisotropic exchange interactions characteristic of orthoferrites.

The propagation contribution allows us to estimate the layer thickness. The thickness of the layers as determined from magneto–optical modelization are summarized in Table 4.2 together with results provided by spectroscopic ellipsometry. Even though the obtained values correspond, it should be noted that spectroscopic ellipsometry is, as far as concerns thickness evaluation, a more maturated technique enabling fitting the data, whereas magneto–optical spectroscopy, also due to its complexity, is based on modelization and spectra comparison only.

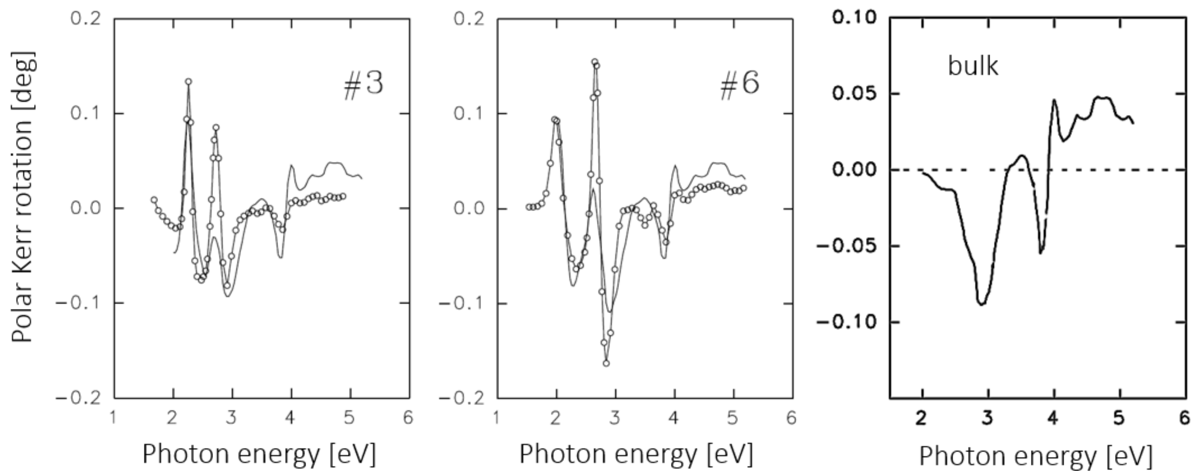

Fig. 4.13: Experimental (symbols) and theoretical (curves) spectra of polar Kerr rotation corresponding to samples #3 and #6. Corresponding spectrum of bulk $SmFeO_3$ (single interface) is presented as well. Modified from Mistrík [126].

4.5 Multilayer

Magneto-optical devices are usually more complex than a single layer. The magnetic layer covered by the non-magnetic film (protective layer or interference amplification layer) was analytically treated, for example, by Mayevskij [143]. Other approaches are based on recursive formalism [123] or on 4x4 matrix algebra (see for example works by Smith [144], Yeh [145], Visnovsky [146, 147], Atkinson [148] or Woollam [149]) and 2x2 matrix algebra applied by Mansuripur [150]. These approaches are convenient for computer modeling of magneto-optical phenomena in multilayered systems. A common strategy for calculation of electromagnetic wave propagating through or reflecting from a multilayer is again based on the solution of the wave equation for each layer and linking these together considering the boundary conditions on each multilayer's interface. That is a generalization of the treatment already encountered in the case of a single interface and single layer. Here

we use 4x4 matrix algebra calculations based on Yeh formalism that was modified for absorbing media by Višňovský [7] and demonstrate its application for characterization of a $[\alpha Fe_2O_3/NiO]_{2.5}$ multilayers [151].

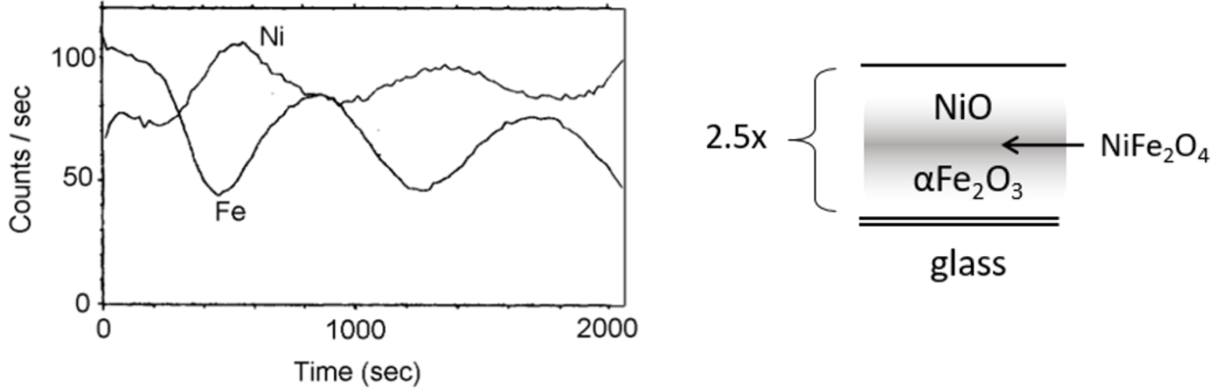

Fig. 4.14: Experimental SIMS profile of Ni and Fe ions across the multilayer evidencing interdiffusion (left). Studied $[\alpha Fe_2O_3/NiO]_{2.5}$ multilayers with a schematic indication of ions interdiffusion through the interfaces accompanied with formation of ferrimagnetic $NiFe_2O_4$ (right).

4.5.1 Interdiffusion in $\alpha Fe_2O_3/NiO$ multilayers

In this part, we discuss the magneto-optical examination of $[\alpha Fe_2O_3/NiO]_N$ multilayers prepared by laser ablation. The successive deposition of NiO and αFe_2O_3 layers with required elevated deposition temperature is accompanied by a formation of $NiFe_2O_4$ at the interfaces [152]. The origin of this formation is linked to the diffusion of Ni ions into αFe_2O_3 and Fe ions into NiO through interfaces. This process depends on the temperature of the substrate, the square root of the annealing deposition time, and the successive order of the NiO and αFe_2O_3 layers in the multilayer [153].

The two selected $[\alpha Fe_2O_3/NiO]_{2.5}$ multilayers that we discuss here were deposited on the amorphous quartz substrate, maintaining deposition temperature at 485°C. The deposition time of individual NiO and αFe_2O_3 layers has been constant and equal to 15 min and 20 min, respectively. Johnson et al. [154] have shown experimentally that deposition of $\alpha Fe_2O_3/NiO$ bilayers with an exceedingly high substrate temperatures ($T_s \geq 750$°C) results in a complete transformation of αFe_2O_3 into $NiFe_2O_4$ due to the diffusion of nickel into the hematite layer. The $\alpha Fe_2O_3/NiO$ bilayer then transforms to $NiFe_2O_4/NiO$. In our case, the substrate temperature does not reach such high values, and therefore, we can assume that the hematite layer has not been entirely converted into nickel ferrite. The concentration profile of Ni and Fe ions measured by SIMS (see Fig. 4.14(left)) presents an oscillatory character, which implies progressive interfaces between the NiO and αFe_2O_3 layers. It is in this interface zone where the formation of nickel ferrite is expected (see Fig. 4.14 (right)).

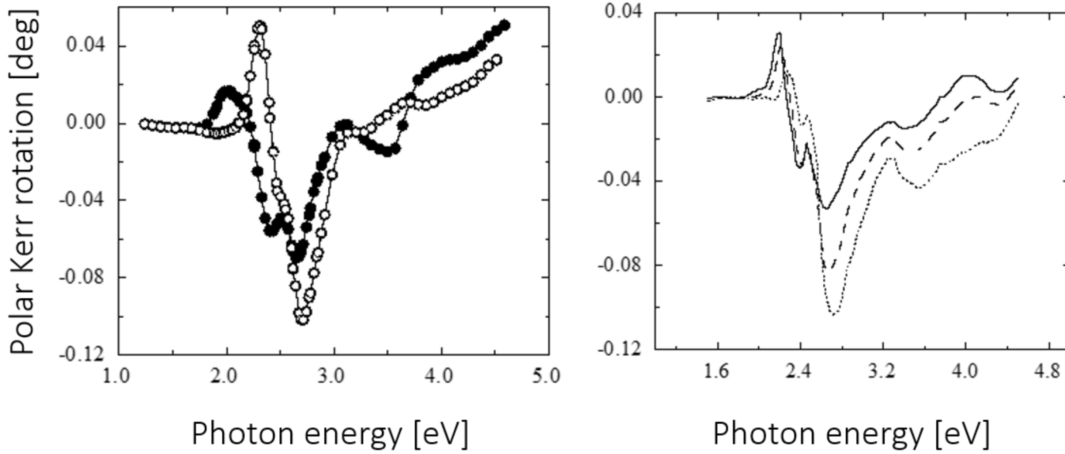

Fig. 4.15: Polar Kerr rotation spectra measured on $[\alpha Fe_2O_3/NiO]_{2.5}$ multilayers with deposition times per layer 15 min (hollow circles) and 20 min (dots) (left). Matrix calculation of $[\alpha Fe_2O_3(t)/NiFe_2O_4(16nm)/NiO(t)]_{2.5}$ model multilayer with the base layer thicknesses of 5nm (dotted line) and 7 nm (dashed line) and 9 nm (solid line) (right). Reprinted from Mistrík et al. [151].

In Fig. 4.15 we show the polar Kerr rotation (PKR) spectra of the multilayers and compare them with the calculations. The model system consists of a multilayer with planar interfaces, where the interdiffusion of Ni and Fe through the interfaces results in the formation of a ferrimagnetic $NiFe_2O_4$ interlayer. The spectral dependences of optical and magneto–optical constants were found in the literature [155, 156, 127]. Magnetization measurements carried out on αFe_2O_3 single layers showed no magnetic moment. That implies for our modeling that αFe_2O_3 is magneto–optically non-active.

Polar Kerr spectra of model multilayers $[Fe_2O_3/NiFe_2O_4/NiO]_{2.5}$ were calculated for various thicknesses of NiO and αFe_2O_3 based layers and $NiFe_2O_4$ interlayers (in a range from 1 to 30 nm). As the deposition time for both base layers was kept constant during the sample growth, the identical values of their thicknesses were considered. The matrix calculation showed the dependence of PKR peaks height and spectral position on the thicknesses of both base layers and interlayers. The analytical approach explains this effect by additional phase changes and optical absorption in these layers [157]. The calculated PKR spectra of $[\alpha Fe_2O_3(t)/NiFe_2O_4(16nm)/NiO(t)]_{2.5}$ multilayers (with t = 5, 7 and 9 nm) that display similar spectral structure as the experimental dependences are plotted in Fig. 4.15 (right). With increasing base layer thickness, theoretically predicted decrease of the peak amplitude at 2.7 eV and the red-shift of PKR spectral features in the visible region were found consistent with the experimental data. The spectral structure in the UV region that can be observed in calculated PKR spectra is also well pronounced in the measured PKR spectrum of $[\alpha Fe_2O_3/NiO]_{2.5}$ multilayer with base layers deposition time of 20 min. However, the corresponding experimental PKR spectral structure of $[\alpha Fe_2O_3/NiO]_{2.5}$ multilayer with base layers deposition time of 15 min is somehow

smoothed out. That can be partially associated with wavelength-dependent light scattering at the diffused interfaces.

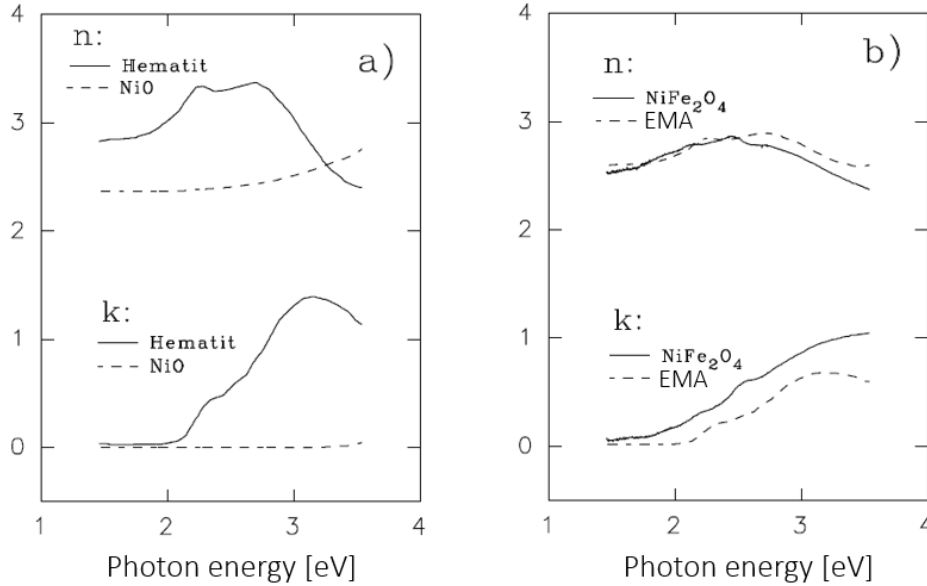

Fig. 4.16: Refractive index n and extinction coefficient k of NiO and hematite αFe_2O_3 a). Comparison of $NiFe_2O_4$ optical constants with those of intermixed NiO and hematite calculated by Bruggeman effective medium approximation b). Modified from Mistrík [126].

We have shown that a model multilayer system with $NiFe_2O_4$ interlayers and sharp interfaces roughly describes the encountered interdiffusion process in the real multilayers and may be understood as a reasonable approximation. Further modeling should take into account the roughness of the surface (interfaces) and appropriate optical and magneto–optical constants of the layers. It is worth noting that in this particular case, magneto–optical spectroscopy provides a unique opportunity to evidence interface formation of ferrimagnetic $NiFe_2O_4$. Other optical methods, including spectroscopic ellipsometry, could not unambiguously distinguish it from an unreacted mixture of nickel oxide and hematite due to their nearly identical optical constants as indicated in Fig. 4.16.

4.6 Linear grating

Magneto–optical spectroscopy can serve as a scatterometric technique analogously to optical ellipsometry and reflectometry that are both frequently used in the industrial inspection of the surface profile of laterally patterned nanostructures (for more details about ellipsometric scatterometry refer to Section 3.6.1). Besides surface geometry, magneto–optics is sensitive to magnetic ordering as well. Therefore, images of magnetization distribution on a sample surface are provided, for example, by single wavelength diffracted

magneto-optical Kerr effect (MOKE) [158] or microscopic MOKE [159]. The conventional alternative tools for the characterization of surface patterning are scanning probe techniques such as atomic force microscopy or scanning electron microscopy. Static micromagnetic properties can be further analyzed by magnetic force microscopy [160], or spin-polarized scanning tunneling microscopy [161]. However, such techniques with respect to MOKE methods are often expensive, cumbersome, and inappropriate for in–situ measurements.

In this section, we show the potentiality of magneto–optic scatterometry applied as accurate quality control of lithography manufactured permalloy linear gratings as well as a tool quantitatively determining the line-edge roughness (LER), native oxide, and other effects that the MOKE is sensitive to [162, 163, 164, 165]. Rigorous coupled-waves analysis (RCWA), already introduced in Section 3.6.1, together with Local modal method (LMM), were applied here to interpret recorded magneto–optical spectra.

Local Modal Method is an approximate analytical method based on the far-field Fourier analysis of grating amplitude reflectance where the reflection coefficients, at each point of the grating's surface, are locally approximated by a laterally uniform structure. This method, derived for treating shallow diffraction patterns, entirely neglects the diffraction effects of the edges. In a special case of a 1D lamellar grating, the far-field reflection coefficients in the specular reflection do not depend on the periodical arrangement but are just weighted functions of the reflectances of the two alternating media

$$r_{jk}^{(0)} = w r_{I,jk} + (1-w) r_{II,jk}\,, \tag{4.46}$$

where $r_{I,jk}$ and $r_{II,jk}$ represent the reflection coefficients corresponding to a lamella element (non-etched medium) and space between lamellas (etched medium including the air gap), respectively. Parameter w denotes the filling factor of the pattern (ratio of the lamella area to the period area), and j,k represent any of the s– and p– polarizations. The higher diffraction orders depend also on the periodical arrangement. But if we assume a simple 1D array of periodic nanowires with the direction of periodicity lying in the plane of incidence, we obtain for higher diffraction orders ($n \neq 0$)

$$r_{jk}^{(n\neq 0)} = \frac{i}{2\pi n}(r_{I,jk} - r_{II,jk})(1 - e^{2\pi i n w})\,, \tag{4.47}$$

which depends on the period only via the filling factor w. It can be further shown that solely r_{pp} coefficient exhibits different values when calculated employing either rigorous RCWA or approximated by LMM, suggesting sensitivity to the edge effect. The r_{ss} and r_{ps} coefficients do not reveal such sensitivity. Therefore, **line–edge roughness** (LER) can be correlated with r_{pp} coefficient. If we evaluate the response of an ideal structure as the exact RCWA calculation and rewrite it into the form

$$r_{pp}^{ideal} = r_{pp}^{LMM} + (r_{pp}^{RCWA} - r_{pp}^{LMM})\,, \tag{4.48}$$

then the value in the parentheses is the error of LMM with respect to rigorous calculation. This error can be identified with the effect of pattern edges. In reality the part of this

effect is reduced due to LER. The reduction can be taken into account by a slightly generalized formula

$$r_{pp}^{real} = r_{pp}^{LMM} + \eta(\lambda)(r_{pp}^{RCWA} - r_{pp}^{LMM}) \tag{4.49}$$

yielding a more realistic value. Here the effect of edges written in the parentheses is reduced by the factor η taking on values assumed between 0 and 1. We refer to the η-factor as the LER parameter, being $\eta = 1$ in the case of ideal regular edges, or $\eta = 0$ when no edge effects are observed. Although the LER parameter is generally assumed to depend on the wavelength, no such dependence is observed in our experimental example given in the next section.

4.6.1 Surface oxidation and edge effect of permalloy lamellar gratings

We apply magneto–optical scatterometry (MOS) to analyze arrays of periodic, about 10 nm thick, Permalloy wires deposited on Si substrates with periodicities of nearly 1000 nm and protected by a 2 nm thick Cr capping layer. Two samples with different periods and wire linewidths were fabricated by means of electron beam lithography combined with ion beam etching. The grating parameters were verified by AFM (cf. Fig. 4.17), which allowed minimizing the number of parameters to be determined by MOKE. The geometrical parameters extracted from AFM pictures are summarized in Tab. 4.3. The

Sample	Period	Linewidth	Thickness (NiFe)
1	900 nm	536 nm	11 nm
2	910 nm	700 nm	12 nm

Tab. 4.3: Description of the samples.

MOKE experiments were performed with a magneto–optical spectroscopic ellipsometer employing the azimuth modulation and compensation technique. The samples were set up with an applied out-of-plane magnetic field of 1.4 T, sufficient to saturate the polar magnetization. The magneto–optical spectra were measured in the specular mode for the incidence angle of 7° in the spectral range of 1.3–5.1 eV for both the s– and p– incident polarizations without revealing any significant differences. The reflection angles of higher diffraction orders are wavelength-dependent, and therefore, a special arrangement was adopted to measure the MOKE in the –1st diffraction order. The angle between the incident and reflected beams was fixed to 20° with the sample free to rotate about the axis parallel to the wires while the wavelength was swept. The position of the beam spot on the detector could not be kept completely fixed with the changing wavelength, which produced artificial jumps in the measured spectra.

Evidence of surface oxidation

The application of s–polarized incident light enables us to detect the presence and thickness of native oxide overlayers developed both on the top of the Cr capping and

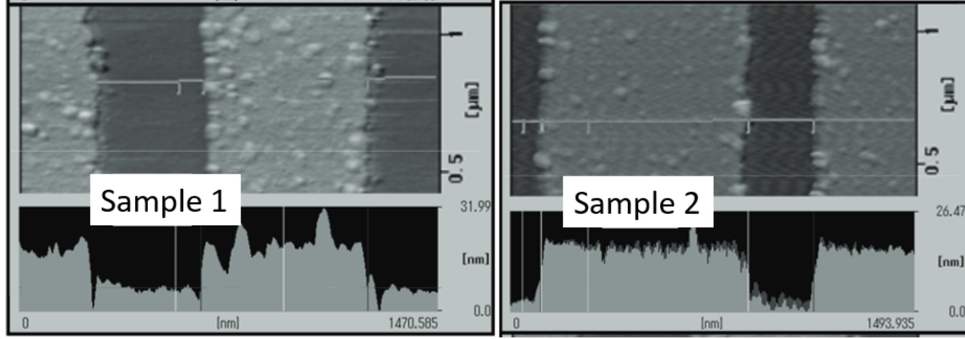

Fig. 4.17: AFM pictures of the NiFe lamellar gratings. Modified from Antoš, Mistrík et al. [162].

the naked Si. We present this analysis obtained on Sample 2 because, in this case, the measurement with s-polarized incident light was affected by the smallest artificial jumps mentioned above. According to the considerable differences among the simulation

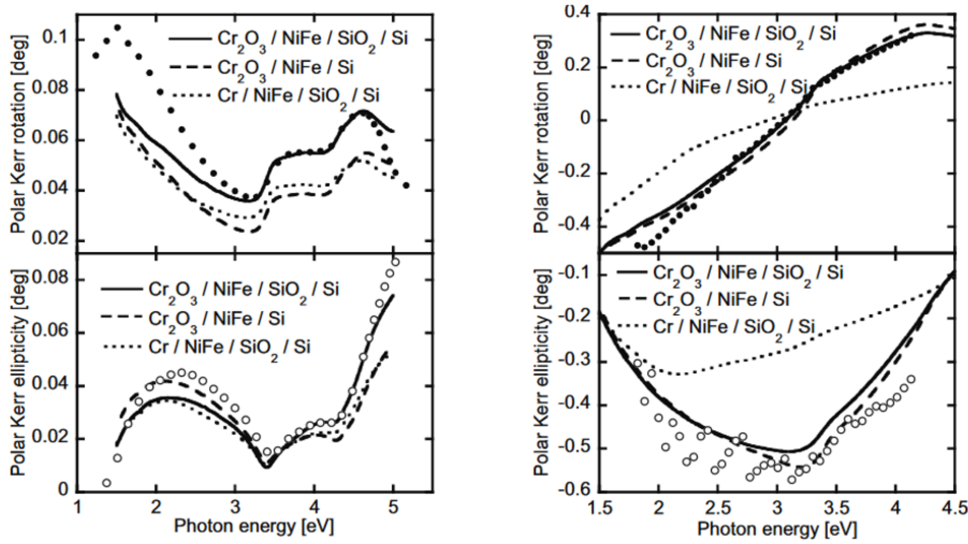

Fig. 4.18: The specular (left) and -1st order (right) MOKE spectra measured on Sample 2 (circles) and computed with LMM simulations employing different thickness of the capping and the substrate native oxide layers: $t(Cr_2O_3)$=2nm and $t(SiO_2)$=3nm (full curves), $t(Cr_2O_3)$=2nm and $t(SiO_2)$=0nm (dashed curves), t(Cr)=2nm and $t(SiO_2)$=3nm (dotted curves). Reprinted from Antoš, Mistrík et al. [164].

curves in Fig. 4.18 (left), the specular (0th order diffracted) MOKE possesses ultra-high sensitivity to the nanoscale native oxides. However, both the top native Cr_2O_3 overlayer and the SiO_2 interlayer exhibit similar trends, and hence the diffracted MOKE in the –1st order becomes essential for distinguishing between the two oxides, as obvious from Fig.

4.18 (right). Here the account for the completely oxidized capping layer ($t(Cr_2O_3) = 2$ nm) remarkably improves the agreement with the experiment. On the other hand, the –1st order diffracted MOKE is less sensitive to $t(SiO_2)$. The explanation can be found in Eq. (4.47), because the contributions of SiO_2 to both, $r_{I,jk}$ and, $r_{II,jk}$ are comparable making the sensitivity of their difference weak to $t(SiO_2)$. This fact is essential for the selective account for the effect of the native oxides and thus manifests the uniqueness of the proposed technique even without simultaneous analyses of reference samples.

Edge effect

In Fig. 4.18 we have only shown LMM simulations since those yielded by RCWA were nearly identical. The agreement between LMM and RCWA simulations does not occur when the p-polarized incident light is applied, which we utilize in the second MOSS analysis. Concretely, the application of p-polarized incident light in a –1st diffraction order configuration where r_{pp} takes on small values enables us to detect LER with remarkable sensitivity. Due to the jumps mentioned above, for p-polarized incident light appearing more significantly on Sample 2, we present this analysis performed on Sample 1. The effect of ideal edges can be seen from Fig. 4.19 (left), where we compare the RCWA and LMM calculations, none of which correctly follows the experimental data. On the other

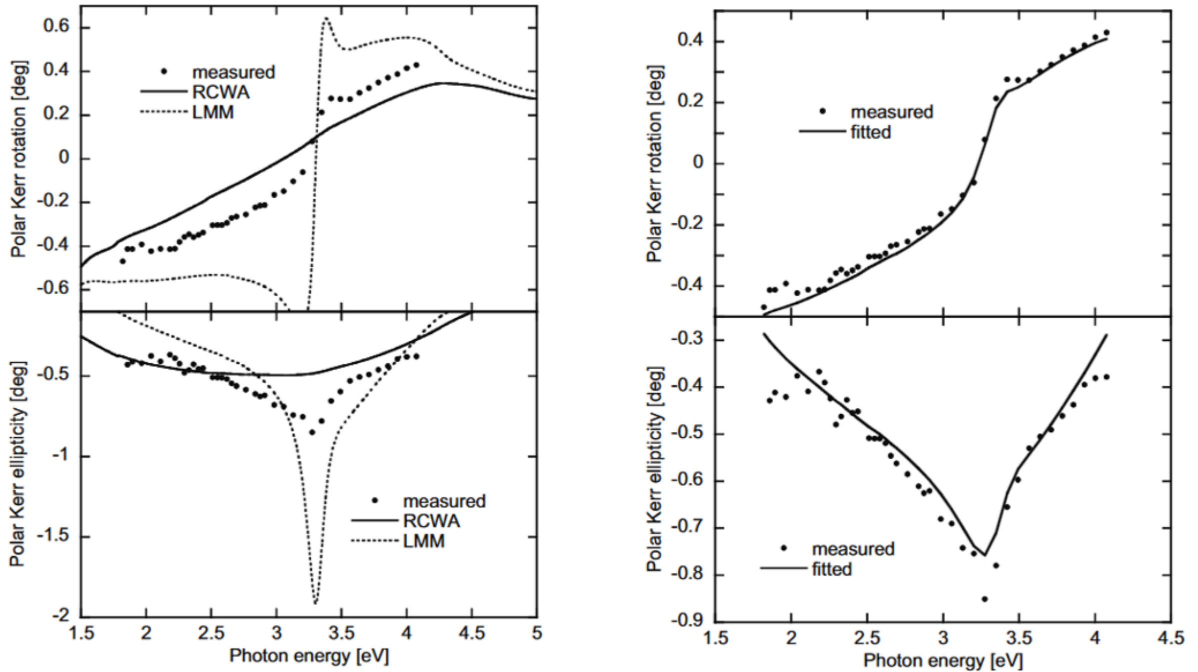

Fig. 4.19: LMM and RCWA simulations of the -1st diffraction order MOKE with p–polarized incident light compared with experimental data (left) and REEM calculation fitted to the experimental data (right) recorded on Sample 1. Reprinted from Antoš, Mistrík et al. [162].

hand, the application of the REEM yields remarkable agreement with the measurement (Fig. 4.19 (right)), provided we have fitted the LER parameter $\eta = 0.53$ defined by Eq. (16). As mentioned above, taking a constant value independent of wavelength was sufficient. The same fitting procedure performed on Sample 2 yielded $\eta = 0.70$, suggesting that Sample 2 is of higher quality. Qualitative comparison of the pattern quality of the both samples can be done by viewing their AFM images shown in Fig. 4.17, where such difference is indeed evident.

4.7 Conclusions

Compared to spectroscopic ellipsometry, magneto-optics reveals additional information about the studied system through a reduced symmetry of the applied external magnetic field or by magnetizing the sample. Although not as matured as spectroscopic ellipsometry, it provides several unique features superior to ellipsometry. Mainly the sensitivity on magnetic arrangement of the studied substance (magnetometry), including the buried layer in multilayers, detection of the strength and nature of exchange interactions and accurate identification of magnetic materials, sensitive crystallographic orientation (employing quadratic magneto–optical phenomena), and more precise characterization of magnetic laterally structured samples by scatterometry, etc. The non-reciprocal nature of magneto–optical phenomena then find employment in various devices of (integrated) magneto–photonics.

Part II

Contribution to the field

Chapter 5

Determination of optical and magneto-optical constants

Publications arranged in this group deals with the determination of material optical and/or magneto-optical constants. Motivation for this kind of material research can be found in several directions (i) expansion, refinement, and spectral broadening of existing data in the material databases (ii) revealing material electronic band structure by analyzing spectral dependencies of optical and magneto–optical constants (iii) tuning theoretical ab-initio calculations comparing these with experimentally obtained spectra (iv) investigation of various influences that have an impact on optical and magneto–optical properties due to for example different deposition methods, quantum confinement, bulk vs. nanostructure, phases (crystalline, amorphous), etc. and finally (v) design of (integrated) photonic elements and other optical or magneto–optical devices such as optical isolators, circulators, modulators, dielectric mirrors, (magneto–)optical memories, etc. with predictable and optimized functionalities.

5.1 Combined method of spectroscopic ellipsometry and magneto–optics

Nickel ferrite [78]

Present work extends the studies of Kahn and Krinchik, who determined and discussed the optical and magneto-optical constants of bulk monocrystalline and polycrystalline $NiFe_2O_4$. In our paper, a single crystal (grown by Prof. Krishnan, LMOV, Université de Versailles) was used. Its native (111) facet was examined by an ellipsometer and a magneto–optical spectrometer. The recorded ellipsometric and complex polar Kerr effect spectra were directly converted to the optical and magneto-optical constants of this material. The optical opacity of the bulk sample enabled the employment of inverse analytical relations developed for the single interface. Obtained constants refined the existing data (especially in the range of absorption edge) and significantly improved modeling of

magneto–optical response of pulsed laser deposited $NiFe_2O_4$ single layers, presented in the article as well. The data reliability was proved by theoretical and experimental consistency of the longitudinal Kerr spectra. Additional details, covering bulk polycrystalline $NiFe_2O_4$ samples as well, and including discussion of optical and magneto–optical spectral features in the framework of electronic dipole transitions of Fe and Ni ions can be found in dissertation thesis [126]. The importance of the results is further evidenced by theoretically focused publications with LSD and LSD-U ab–initio calculations of $NiFe_2O_4$ magneto–optical constants providing reference to our data determined from the experiment [166].

Copper ferrite [167]

Optical and magneto–optical constants of Cu ferrite were determined from ellipsometric and complex polar Kerr spectra recorded on sputtered thin films (Prof. Prasad's group, Indian Institute of Technology, Bombay, India). Numerical treatment of the experimental spectra required iterative fitting in contrast to the analytical inverse formula of a single interface. Obtained spectra were parameterized by a set of oscillators and interpreted by inter–valence and inter–sublattice charge transfer transitions. These were compared with electronic transitions typical for other ferrites studied so far. Influence of layer post–deposition treatment, when the $CuFe_2O_4$ cubic structure was obtained by fast cooling (quenching) from the deposition temperature, or the tetragonal structure by slow cooling, was discussed as well.

Perovskite $La_{2/3}Sr_{1/3}MnO_3$ [168, 50]

Doped $LaMnO_3$ (LMO) is a material interesting for its rich and versatile properties (for example, metal-insulator transition, colossal magneto–resistance, etc.). In particular, $La_{2/3}Sr_{1/3}MnO_3$ (LSMO) exhibits strong spin polarization, which predestines it for spintronic applications. Optical and magneto-optical spectroscopy reveals the complex electronic structure of this material through the electronic transitions captured in spectra of optical and magneto-optical constants. Mentioned article [168] shows these spectral dependencies obtained by optical and magneto-optical ellipsometry on a series of LSMO layers deposited on monocrystalline $SrTiO_3$ substrate in the laboratory of prof. Ph. Lecoeur, Orsay, France by pulsed laser ablation. One of the LSMO layers was designed to be optically thick, and therefore, its spectra were treated in the approximation of a single interface. The optical and magneto-optical constants were then determined directly from light interaction with the layer surface without the need to take into account the interference phenomena in the layer. The reliability of the determined constants was verified by modeling the polar Kerr rotation spectra of LSMO thinner films and comparing them with the experiment. Both propagation phenomena in the layer and phenomena related to reflection from the surface were identified and theoretically interpreted. The nature of electronic transitions was discussed in more detail in the subsequent publication [50]. The obtained results were used by other authors as a reference for ab–initio calculations

of LSMO magneto–optical spectra [169, 170] and in the study of ferromagnetic surface polarization of the LMO/STO interface detected by nonlinear magneto–optics [171].

Garnet Ce-YIG [31]

Monolithically integrated and nanostructured magneto–optical modulators, isolators, and circulators, based on non–reciprocal behavior of the Faraday rotation, are the key component of optical signal processors and other photonic devices. The most commonly used magneto–optical materials are cerium or bismuth substituted yttrium iron garnets that show one of the highest figure of merit, i.e., the ratio of Faraday rotation and absorption coefficient. These materials manifest low transmission loss as well as high Faraday rotation in technologically relevant IR spectral region. The present paper reports on optical and magneto–optical characterization of Ce:YIG thin films pulsed laser deposited onto gadolinium gallium garnet substrates with various crystallographic orientations (group of prof. Rosse, MIT, Boston, USA). Ellipsometric and magneto–optical (Faraday and polar Kerr effect) spectroscopy enabled determination of both diagonal and off–diagonal elements of Ce:YIG dielectric tensor in the relatively broad spectral range from 200 to 1770 nm. The highest figure of merit in the IR range was achieved for films deposited on (111) substrate orientation. It is worth noting that it presents the highest figure of merit of Ce:YIG thin films reported so far. For the wavelength of interest $\lambda = 1550$nm, the absorption of the films was relatively small. At such low extinction values, the fitting of the sole ellipsometric spectra (recorded in reflection) does not yield sufficiently precise values of extinction coefficient. Therefore, additional transmission measurements in the IR region with FTIR spectrometer were carried out and included in numerical data treatment.

5.2 Optical ellipsometry

Work selected in this section contributed to (i) correction or refinement of existing optical constants ($LaNiO_3$, $PbZrTiO_3$), (ii) determination of optical constants of materials that have not been analyzed yet and that proved to be of application interest (FeF_2, TaN, VN), (iii) assessment of differences in optical properties of bulk and thin-film forms along with the influence of thin-film deposition conditions (NiO), (iv) assessment of differences in optical properties of amorphous and poly–crystalline chalcogenides (MoS_2, Sb_2S_3, Sb_2Se_3), and (v) VUV extension of optical constant spectral range by reflectivity measurements on a synchrotron facility ($PbZrTiO_3$).

Perovskites $LaNiO_3$ [172] and $PbZr_{1/2}Ti_{1/2}O_3$ [82, 81]

Bilayer $LaNiO_3/PbZr_{1/2}Ti_{1/2}O_3$ system is used in a number of electro–optical applications. The metallic $LaNiO_3$ (LNO) layer serves as an electrode and at the same time acts as a seed or buffer layer for textured growth of piezoelectric $PbZr_{1/2}Ti_{1/2}O_3$ (PZT). Presented works deal with optical constants of both materials (LNO and PZT), which supplement or expand the data available in the literature until then. Samples were prepared

by the sol-gel method in the laboratory of prof. N. Dai (Shanghai Institute of Technical Physics, China). Optical constants of LNO, parameterized by a dielectric function consisting of the sum of Lorentz oscillators, were determined by simultaneous evaluation of ellipsometric and reflectance spectra applying a single-layer model. Special attention was devoted to the influence of LNO surface roughness represented either by the effective medium or the Rayleigh–Rice theory. The roughness determined by optical methods was then compared with complementary AFM measurements.

Evaluating PZT optical constants, parameterization of the joined density of states directly related to the material band structure was considered. In this manner, UV spectral features related to 4d and 3d valence electrons of Zr and Ti were identified. PZT layers were afterward measured at the synchrotron facility (Okazaki, Japan) in the vacuum UV spectral region to expand the range of its optical spectra and to gain additional knowledge of the electronic transitions. The results are summarized in a technical report [81], which describes the experimental measurement of wide spectral range reflectivity and its numerical treatment by Kramers-Kronig relations, allowing calculation of the phase of the reflection coefficient. Knowledge of its both real and imaginary parts then yields the VUV optical constant of PZT. For more details refer to Section 3.3.3.

Nitrides TaN and VN [43]

Motivation for optical constants determination of vanadium and tantalum nitride comes from their intended use as barrier layers in ultra-large-scale integrated (ULSI) circuits. Knowledge of the optical constants is essential for effective in–line optical monitoring of the ULSI circuits deposition process. VN optical constants with a typical metallic character were available in the literature. Nevertheless, the method of their determination, i.e., high energy electron loss spectroscopy, which is fundamentally different from spectroscopic ellipsometry, was one of the reasons (together with the different microstructure of the studied samples) of certain quantitative deviations of ours and literature data. In our case, the V and Ta nitrides were deposited by reactive magnetron sputtering (RIE, University of Shizuoka, Japan). In addition, TaN layers prepared under various substrate temperatures and deposition times showed different optical constants. This was manifested mainly by the weakening of their metallic character with lowering deposition temperatures. The reason for this variation was attributed to the presence of different TaN phases (the filling factors of which depended on the specific deposition conditions) in the complex phase diagram of the Ta-N system.

Flouride FeF_2 [173]

Optical characterization of iron fluoride FeF_2, that forms one of the particular results in the present article, is closely related to the optimization of the design of a magneto-optical sensor based on a sandwiched $FeF_2/Fe/FeF_2$ structure, operating on the wavelength of Ti: sapphire laser (810nm). This sensor was intended to detect weak magnetic fluxes up to microwave frequencies with sub-micrometer resolution. Films were MBE grown on noble

metal reflectors separated from GaAs(001) substrates by a seed Fe layer (Dr. Celinski, Univerity of Colorado at Colorado Springs, USA). The sum of three modified oscillators, which could change from Gaussian to Lorentzien shape tuning the value of one parameter, proved to be a suitable parameterization of FeF_2 optical constants in the UV, visible and near-infrared regions. The parameters of the oscillators were determined by fitting the ellipsometric spectra. Obtained FeF_2 optical constants allowed theoretical modeling of the magneto-optical spectral response of the $FeF_2/Fe/FeF_2$ sandwich structure and its optimization by tuning the thicknesses of the individual layers to maximize magneto–optical signal in the targeted NIR region.

Nickel oxide [174]

This work compares optical constants of polycrystalline NiO deposited in the form of a thin layer by laser ablation (LMOV laboratory, University of Versailles, France) with those of the bulk single crystal (data available in the literature). Thin-film refractive index and extinction coefficient were determined by simultaneous fitting of the ellipsometric and optical reflectance and transmittance spectra, taking into account several non–idealities of the layer such as its surface roughness and gradient profile of the refractive index across the layer. The difference of mono–crystalline bulk and poly–crystalline thin film optical constants was attributed mainly to their different crystallinity.

Chalcogenides MoS_2[175], Sb_2S_3 and Sb_2Se_3[176]

Amorphous and crystalline chalcogenides have found potential in numerous applications such as optoelectronics, biosensors, data and energy storage, and photo-thermal therapy, among others. Knowledge of mechanisms that control amorphous-to-crystal transition is an essential requirement for integrating chalcogenides into smart devices. Determination of optical properties of amorphous and crystalline MoS_2 contributed to the understanding of the underlying scenario during annealing-induced crystallization of this material. That was theoretically modeled by the ab–initio molecular dynamics approach. On the other hand, precise optical constants determination of Sb_2S_3 and Sb_2Se_3 was motivated by the application of these phase change materials in reconfigurable photonic devices. Based on obtained optical properties, the performance of low–loss directional couplers in the telecommunication spectral zone was modeled by Finite difference time domain calculations by Yu Teo. Chalcogenide films were sputter deposited in the group of Dr. Krbal, CEMNAT, the University of Pardubice (MoS_2) and by Dr. Simpson (Sb_2S_3, Sb_2Se_3), Singapore University of Technology and Design, Singapore.

Chapter 6

Characterization of nanostructures

6.1 Single layers

In this section, I summarize papers where optical and magneto-optical ellipsometry was employed for the evaluation of layer inner structure, magnetic ordering, doping, surface plasmons, and correlation of mechanical and optical properties of polymer films. Mentioned are also works related to the study of refractive index modification of a material by an electron, charged particle, or light beam irradiation. Effects of the surface roughness and sample temperature are mentioned as well.

Inner structure: nanocrystalline NCD [94]

Ellipsometry study of the inner structure and diamond quality of nanocrystalline diamond (NCD) film is presented in detail in Section 3.5.1.

Doping: B-NCD [177], Co-CeO_2 [178], Sn-ZnO [42], and PSS-PEDOT [40]

Doping of diamond allows inducing its semiconducting nature with either hole or electron conductivity according to the type of dopant. Therefore, diamond pn junction is realizable, which opens a new path for the application of a plethora of diamond attractive properties (including high thermal conductivity) not only in electronics. This work is devoted to the study of boron-doped nanocrystalline diamond layers deposited by MWPE–CVD using an innovative reactor with a set of linear antennas and pulsed plasma. This reactor was specifically designed and constructed in the Institute of Physics of the Czech Academy of Sciences, Prague for homogeneous large areas and low substrate temperature deposition of diamond layers. Plasma initiation was done in a working gas mixture of TMB, CO_2 and CH_4. Layers prepared with different ratios of these gas components, hence, with different boron doping levels, were simultaneously characterized by following methods: conductivity and Hall measurements, neutron depth profiling, SEM, Raman, and ellipsometric spectroscopy to study plasmo–chemical processes and their influence

on structure and composition of the deposited layers. Spectroscopic ellipsometry has proven to be a method that is sensitive not only to the examination of the layer thickness and surface roughness but also to the degree of hole concentration and diamond quality. The concentration of holes (of the order of 10^{23}cm^{-3}) was quantified using the values of the Drude term amplitude in the NIR spectral region. The qualitative assessment of diamond quality (sp^3/sp^2 ratio of hybridized carbon) was based on monitoring the absorption edge in the UV region that was parameterized by Tauc–Lorentz oscillator. The obtained results from spectroscopic ellipsometry proved to be consistent with the other complementary tools and at the same time, the considerable potential of this method in the characterization of thin films was underlined.

The second article included in this group relates to the spectro-ellipsometric and magneto-optical characterization of CeO_2 layers doped with Co. Doping the nonmagnetic host material CeO_2 with magnetic Co ions influences its optical and magneto–optical properties. This can be ultimately used for the fabrication of optimized magneto–optical materials and their applications as, for example, magneto-optical insulators, magneto–plasmonic sensors, or magneto–photonic crystals. Studied layers were prepared by pulsed laser deposition in the group of prof. Rosse, MIT, USA. As shown by X–Ray diffraction, Co ions formed a solid phase solution in the CeO_2 host medium. The optical constants of the layers, parameterized by the sum of the Lorentz oscillators and the Tauc–Lorentz oscillator, were determined by simultaneous fitting of the ellipsometric and optical reflectance and transmittance spectra. The presence of Co ions increased absorption in the CeO_2 forbidden band and caused a redshift in its absorption edge, which can be attributed to the impurity states of various types of defects (oxygen vacancies, Co ions, etc.). Due to the relatively low concentration of Co ions, parameterization of NIR optical constants did not require the use of the Drude term, contrary to the case of boron–doped nanocrystalline diamond films.

In this paragraph, we refer also to the ellipsometry studies of Sn doped ZnO [42], and PSS doped PEDOT films [40].

Surface plasnoms: Au island structure [38] and Au nano–spheres

When light interacts with metallic nanostructures, the generation of surface plasmons may occur. The surface plasmons can be excited in metallic nanoparticles embedded in a dielectric environment, on rough surfaces of metals, or metallic grids. At present, these structures are used in various forms, for example, as plasmonic sensors. Consequently, optical characterization and theoretical approaches are being improved for the non-destructive characterization of such nanostructures (determination of nanoparticle distribution, shape and size). Present article deals with the study of surface morphology, crystal structure, electrical transport, and optical properties of sputtered Au thin films (Prof. Švorčík's group, VŠChT, Prague). Au layers deposited within the shortest times showed an island-like discontinuous structure. Increasing deposition time, they became denser and eventually turned into a continuous layer passing the percolation limit. Ellipsometric spectra of the given Au nanostructures were evaluated by an approximate

sample model consisting of a homogeneous thin film. Island–like structure of thinner layers leads to the excitation of surface plasmon manifested in optical constants by localized Lorentz type oscillator, whose resonant frequency red-shifts and splits from one oscillator into two by approaching the percolation limit. Here, also transition from non-conductive to conductive nature of the Au layers occurs as detected by the amplitude of the Drude term. The results drawn from the analysis of ellipsometric spectra were confirmed by other complementary characterization methods.

Similar features, as described above, can be observed for gold nanospheres as well. Fig. 6.1 presents surface plasmons on Au nanoparticles deposited with increasing density and approaching percolation limit on c-Si substrates.

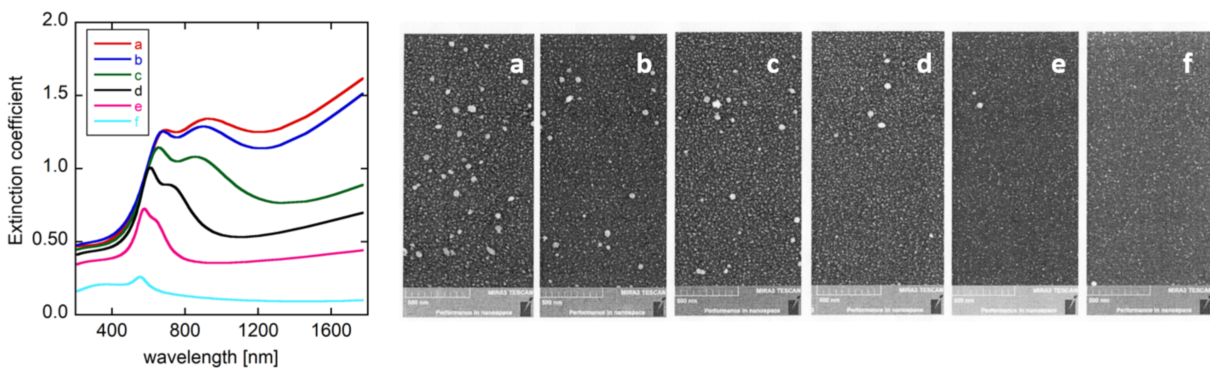

Fig. 6.1: Surface plasmons (left) excited on Au nanoparticles deposited on Si substrates with increasing density (right). Samples provided by prof. Biederman, Faculty of Mathematics and Physics, Charles University, Prague.

Magnetic ordering in orthoferrites: $SmFeO_3$ [179, 180]

Orthoferrites are interesting from the point of view of both basic research (phase transition due to the spin reorientation) and applied research (strong Faraday rotation). Recently, deposition of orthoferrites in the form of thin films by pulsed laser ablation has been succeeded (Prof. Krishnan, Dr. Keller, LMOV, Université de Versailles). Magneto–optical spectroscopy, due to its sensitivity to subtle magnetic arrangement through spin-orbital interaction, proved to be an extremely effective characterization tool of the so-called weak ferromagnets. These include orthoferrites, with almost compensated spin magnetic moments governed by Dzialoshinsky–Moria interaction. Paper [179] presents pulsed laser deposition of thin layers of Dy, Y, Sm, and Gd orthoferrites. Their proper magnetic interaction and ordering were examined by magneto–optical response measured in Faraday and polar Kerr configurations. Calculated and experimental magneto–optical spectra in the UV region (where no propagation contribution is shown and the spectra are characteristic for the given material regardless of the layer thickness) consistently featured all electronic transitions typical for orthoferrites. Furthermore, the X-Ray diffractometry confirmed the polycrystalline orthorhombic structure of the layers.

In addition, deposition parameters of $SmFeO_3$ thin films were optimized establishing relationship between the deposition temperature and fluence of the laser beam focused on the target during ablation [126] (cf. Section 4.4.2). It has been shown that the deposition temperature can be reduced within certain limits while increasing the laser fluence. Optical constants obtained by ellipsometry on bulk $SmFeO_3$ targets polished to optical quality were used to model the magneto–optical spectra. For more reliable magneto–optical characterization, spectroscopic ellipsometry on $SmFeO_3$ ablated thin films was performed, and corresponding optical constants were determined in [180].

Correlation of optical an mechanical properties: polymer VTES single layers [181] and functionally gradient TVS films [182, 183]

The primary motivation of this work is related to the control of mechanical binding between different constituents inside composite construction materials. More specifically, it concerns the preparation of a functional intermediate layer between the epoxy matrix and the reinforcing glass fibers (Prof. Čech, Brno University of Technology). In an optimized composite, the two components should be firmly bonded to each other and provide a smooth transition of the mechanical elastic modules from the matrix to the reinforcing fibers through the functionalized interlayer. Due to the correlation of optical and mechanical properties of the polymer layers, spectroscopic ellipsometry was used as one of the methods of their characterization. First, the study took place on single polymer layers and then on multilayer systems, which were eventually replaced by an interlayer with a fully gradient nature of mechanical (and at the same time optical) properties. The present article presents the optical characterization of polymer layers prepared by plasma-assisted CVD from VTES monomer. Tauc Lorentz's formula turned out to be a suitable parameterization of its optical constants. The internal structure of the layer was assessed against various sample models taking into account properties of substrate/ layer interface, the gradient nature of the layers, and in the case of thick layers, the effect of their thickness inhomogeneity on the optical spectra.

Then the single–layer investigation was expanded to the case of multilayer systems with a step-like change of polymer physico–chemical properties. The change of these properties was intentionally induced by time variation of the effective plasma power in the pulsed plasma chemical reactor. The TVS monomer used in the gas phase is thus converted by plasma polymerization into the polymer with different degrees of crosslinking and organic / inorganic ratio as a function of the applied effective power. The ultimate purpose was to induce a continuous change of mechanical properties of the multilayer (modulus of elasticity and mechanical strength), which on one side chemically bonds to one (matrix) and on the other side to the other (reinforcing fibers) component of composite material. Due to the relationship between optical and mechanical properties, the spectroscopic ellipsometry can indirectly monitor these changes of mechanical parameters of the multilayer (through evaluation of refractive index profile) and thus non–invasively and in–situ assess transition characteristics, such as linear or exponential, as presented in [183].

Other effects influencing optical properties

Here I mention contributions dealing with modification of optical properties of a material due to its irradiation or exposure by an electron [49], heavy particle [184], or light beam [48]. Influence of surface roughness is treated, for example, in [185, 172] and effect of sample temperature on optical constants are discussed in more detail in Section 8.2 and in [47].

6.2 Multilayers

Multilayered nanostructures are widely used in a plethora of current applications across various industries profiting from their specific optical, electrical, and magnetic properties. With a suitable internal structure, unique functionalities can be achieved that are not naturally offered in the bulk or single–layered form. This section presents works that use optical and magneto–optical ellipsometry for the characterization of application–promising multilayers.

Exchange interaction in Co/Cu multilayers [186]

The discovery of the giant magnetoresistance (GMR) exhibited by certain metallic multilayers with alternating magnetic and non–magnetic layers was awarded the Nobel Prize (Albert Fert and Peter Grünberg in 2007). Parallel and anti–parallel ordering of magnetic moments of ferromagnetic layers coupled by a non-magnetic spacing layer has been the subject of several theoretical studies. This fundamental phenomenon has found application in high-capacity storage media employing spin-polarized current. The exchange interaction mediating this magnetic arrangement, and periodically dependent on the space layer thickness, modifies the band structure of the layered materials. The presented paper shows the effect of this modification on the experimental magneto–optical spectra recorded in the polar and longitudinal configuration on Co/Cu multilayers, which show significant differences for AFM and FM arrangements. These phenomena are not predictable by theoretical calculations using bulk optical and magneto–optical constants of the given materials (Co and Cu). Experimental ellipsometric spectra showed similar differences in AFM and FM ordering as well. It was concluded that the dominant effect of the exchange interaction is related to the modification of the optical constants of the non-magnetic metal through which the exchange interaction takes place.

Omniderectional mirror [187]

The motivation of this work was the design and fabrication of a dielectric mirror whose reflectance band does not significantly change with the incidence angle (omnidirectional mirror). The central wavelength was chosen to be $\lambda = 1.55$ μm, i.e., in the spectral region often used for telecommunication applications (for example, missile guidance). A dielectric mirror consisting of alternating high and low index layers of optical thickness $\frac{\lambda}{4}$ was

prepared from a pair of chalcogenide materials $Ge_{25}S_{75}$ and $Sb_{40}Se_{60}$ transparent in the IR region and with refractive index difference $\Delta n = 1.16$ (deposited by Dr. Kohoutek, University of Pardubice). The calculated band structure of a given multilayer (assuming an infinite number of bilayers) is indicated in Fig. 6.2. Value of the forbidden band for the normal incidence corresponds to the interval $1.33 - 1.79$ μm, and for the oblique incidence it becomes $1.33 - 1.57$ μm. The real multilayer was prepared by evaporating 7.5 $Ge_{25}S_{75}/Sb_{40}Se_{60}$ bilayers on SiO_2 substrates. Mirror quality and effect of post-deposition annealing were assessed by reflectance and ellipsometric spectroscopy carried out for different angles of incidence. The quality of the interfaces was simultaneously monitored by TEM.

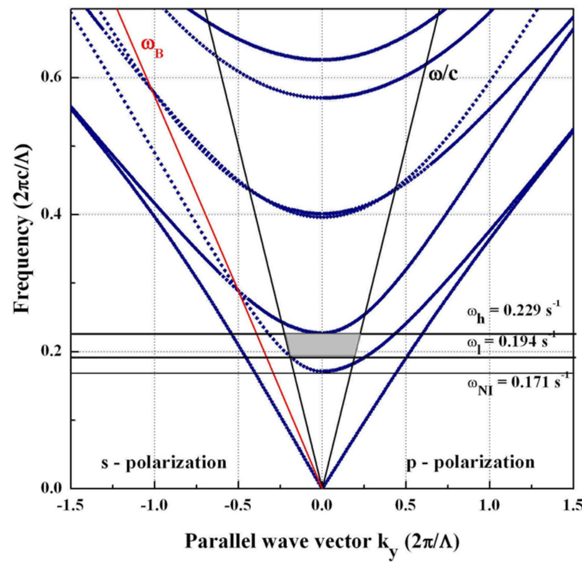

Fig. 6.2: Projected bandgap structure of the $Ge_{25}S_{75}/Sb_{40}Se_{60}$ quarter wave stack, with refractive indices n_H=3.23, n_L=2.07 and layer thicknesses d_H=119 nm, d_L=187 nm, showing the first order omni– directional and normal–incidence bandgap near 1.55 μm; ω/c line is the light line in the multilayer; ω_B relates to the Brewester angle.

Interdiffusion in αFe_2O_3/NiO multilayers [151]

One of the advantages of optical and magneto-optical ellipsometry is its non-invasive examination of sample subsurface structure within the penetration depth of light. The present article demonstrates this by magneto–optical identification of ferrimagnetic inverse spinel $NiFe_2O_4$ that forms on the interface of αFe_2O_3/NiO multilayers (prepared by pulsed laser deposition by Dr. Keller, LMOV, University of Versailles). The SIMS evidenced interdiffusion of Ni and Fe ions across the interfaces between antiferromagnetic materials NiO and αFe_2O_3. Spectroscopic ellipsometry was not, in this particular case, sensitive enough to distinguish $NiFe_2O_4$ due to similar values of its refractive index with a mixture of

NiO and hematite (approximated by the two-component EMA). Nevertheless, modeling of magneto-optical spectra has convincingly demonstrated the presence of $NiFe_2O_4$ material at the interfaces and thus demonstrating the usefulness of this characterization method. For more details refer to Section 4.5.1.

6.3 Linear gratings

Application of optical and magneto-optical ellipsometry, as a characterization tool, has been for a long time restricted for samples that could be approximated by a single planar interface (bulks) or by a plane–parallel stratified media (single layers and multilayers) for which appropriate theoretical formalism (recurrent formulas, matrix calculus) were available. On the other hand, scatterometry studying the angular dependence of the intensity of diffracted monochromatic light was devoted to the characterization of laterally periodic structures (for example gratings). Accelerating the increase of the computer power together with the amelioration of theoretical procedures (for example, RCWA, FEMA) in the last decades has made it possible to extend optical and magneto-optical spectroscopic ellipsometry also for the characterization of laterally periodic structures, and photonic crystals in general.

Ni garting: optical scatterometry [109]

Optical scatterometry of the sinusoidal holographic Nickel grating is presented in Section 3.6.1 where results of other conventional complementary characterization techniques are presented and compared as well.

Permalloy garting: magneto–optical scatterometry [188, 162, 163]

Present articles show one of the first magneto-optical studies of laterally periodic structures, namely, permalloy wires prepared by electron lithography on silicon substrates and covered with a Cr protective layer (Prof. Hillebrands, University of Kaiserslautern, Germany). Magneto-optical spectra in the polar Kerr configuration were measured in both the zeroth (specular reflection) and the first diffraction orders. Theoretical dependences were then calculated by the rigorous method (RCWA) and by the approximate LMM approach developed for shallow gratings neglecting diffraction at the edges of NiFe wires. Detailed modeling of the magneto-optical spectra evidenced the oxidation of the Cr coating of the permalloy wires and the presence of SiO_2 on the exposed part of the silicon substrates (cf. Section 4.6.1). The results of magneto–optical ellipsometry showed agreement with AFM and proved the sensitivity of this method not only to the surface oxidation (influence of aging or post-deposition) but to the geometric quality of relief gratings and the edge profile as well.

6.4 Complex architectures

1D conical nanotubular TiO_2/CdS heterostructure [189]

Enhancement of photon harvesting efficiency is a key issue in photovoltaics. So far, different strategies were employed to achieve this goal. The present work reports on the superior performance of solar cell heterostructure (fabricated in the group of Dr. Macák, CEMNAT, University of Pardubice) based on a 1D conical TiO_2 nanotubular scaffold homogenously coated by CdS thin-film photosensitizer. A significant feature of the heterostructure, with respect to the uncoated TiO_2 nanotubes, was a pronounced redshift of the onset edge observed in the photon-to-current efficiency spectrum. It was suggested that this effect is caused by a sub–bandgap tail of the CdS coating. This hypothesis was proved to be correct by ellipsometric measurements of CdS thin films deposited under the same conditions onto planar Si substrates. Light scattering inside the nanotubular structure with the associated multiple transmission and absorption processes plausibly elucidate the observation of the redshift which furthermore indicates the possible improved performance of the heterostructure integrated into the solar cell.

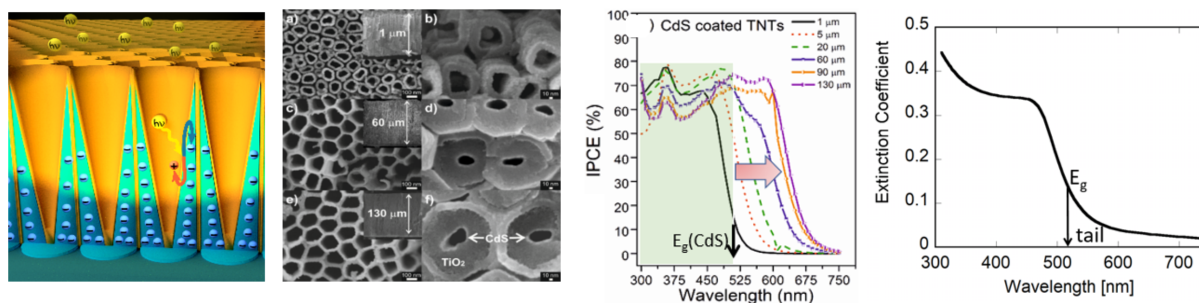

Fig. 6.3: From left: schematic 1D nanotubular structure, SEM top-view pictures, spectral dependence of IPCE as a function of CdS overlayer thickness, and CdS extinction coefficient determined by spectroscopic ellipsometry (reprinted from [189]).

2D $MoTe_2$ nanosheets [190]

2D $MoTe_2$ nanosheets were atomic layer deposited in the group of Dr. Macak (CEMNAT, University of Pardubice) and intensively studied for their photo–electrocatalytic properties. It is worth mentioning that spectroscopic ellipsometry employed for characterization of these nanostructures differentiated their semi–metallic 1T' phase with respect to the more stable semiconducting 2H phase. The predominantly semi–metallic nature of $MoTe_2$ lead to the reported excellent photo–electrocatalytic properties of TiO_2 nano-tube heterostructures decorated by $MoTe_2$ nanoflakes.

Chapter 7

Theoretical approaches

Inhomogeneous index–gradient films [191]

Inhomogeneous thin films that present index gradient along its surface normal are often encountered in practice. It can be either an undesirable effect due to uncontrolled deposition process or intended feature, where carefully designed index gradient gives an exceptional spectral dependence of reflectance or transmittance – the case of rugate filters, for example. The present article deals with a new algorithm of reflection and transmission coefficients calculation, developed for inhomogeneous films, that extends well known Wentzel–Kramers–Brillouin–Jeffreys (WKBJ) approximation. The algorithm is based on

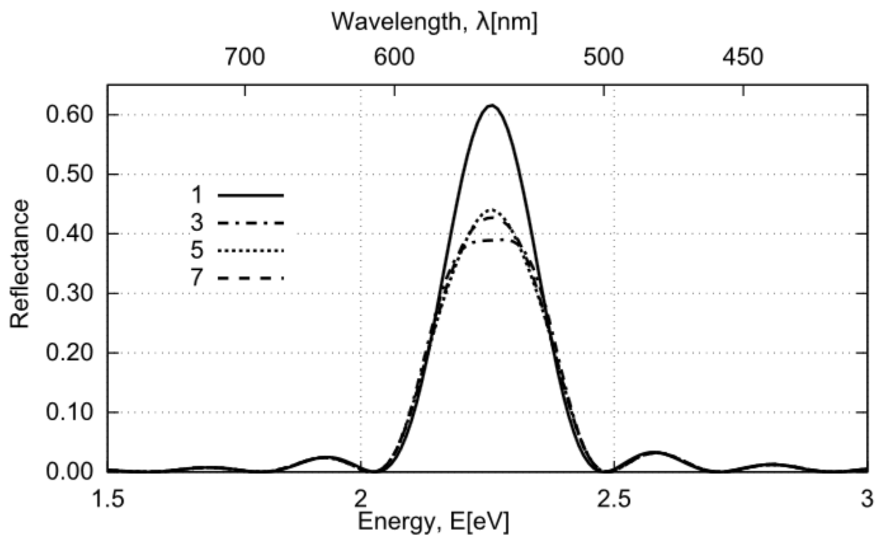

Fig. 7.1: Rugate filter with matched surroundings layers. The refractive index of the ambient and the substrate is 2.0. The film index is given by $n = 2.0[1{+}0.05\sin(\omega z)]$. The resonance wavelength is $\lambda_0 = 550$ nm, $\omega = (4\pi n_0)/\lambda_0$, the number of periods is 10, and the total thickness is 1375 nm. The reflectivity is calculated with indicated truncation of the expansion (reprinted from [191]).

multiple–beam interference expansion of reflection and transmission coefficients where the first term is the WKBJ contribution. The degree of calculation precision can be easily controlled by the expansion truncation. The calculation speed is considerably enhanced by the application of Chebyshev polynomials. Therefore, it is acceptable also for on–line monitoring of fabrication of rugate–type filters (cf. Fig. 7.1). Inhomogeneous films with various index gradient profiles on dielectric or metallic substrates are modeled and discussed concerning the calculation speed and convergence. Experimental ellipsometric data recorded on the inhomogeneous SiN layer and their treatment by the new approach are presented as well.

Chapter 8

Collaboration with industry and application motivated research

In this chapter, I provide a list and brief description of my participation in application–motivated research conducted by below mentioned companies.

8.1 Murakami Kaimeido, Ltd., Japan

The research aim was the identification of structural non–idealities of fabricated dielectric multilayer mirrors $[SiO_2/Nb_2O_5]_N$ deposited on glass substrates that manifested deteriorated optical performance. The simultaneous combination of spectroscopic ellipsometry and optical reflectance and transmittance enabled the identification of the origin of searched defects. Namely, the unintended change of the substrate refractive index, caused by inappropriately set deposition parameters of selected deposition technique, id est, high-density reactive ion plating (cf. Fig. 8.1). For more details refer to [90] and see also Section 3.4.2.

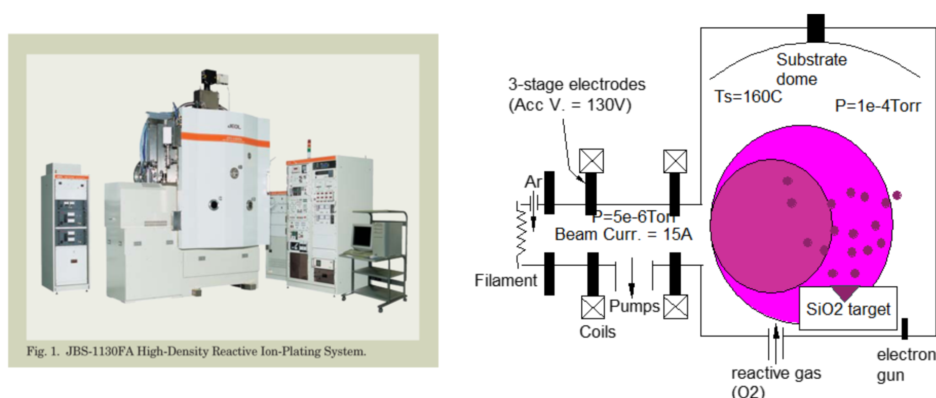

Fig. 8.1: High-density reactive ion plating deposition apparatus (left) and its schematic picture (right).

8.2 Komatsu Electronics, Ltd., Japan

The goal of this collaboration consisted of proof of concept and development of a non-contact optical device measuring Si wafer temperature and simultaneously monitoring the growth of a dielectric overlayer. The request came from Komatsu Electronics, Ltd., manufacturer of high–quality crystalline Si wafers, which is a producer of heating plates with homogeneously distributed and precisely controlled temperatures as well. These systems are frequently used in various deposition apparatus in the semiconductor industry.

The research was based on previous studies related to the temperature dependence of c-Si optical constants [192]. The temperature-sensitive ratio of the s– and p– reflection coefficients (angle of incidence 70°) near the E_1 critical point of c-Si (wavelength 370 nm) was used to measure the surface temperature. Additional spectral points were selected to monitor also the growth kinetics of the dielectric overlayers. It turned out that for the required accuracy of temperature measurement (0.1 °C) it was essential to detect the light intensities of s– and p– polarized reflected waves at the same times, and thus eliminating fluctuation of the light source (high-pressure Hg-Xe lamp) intensity. The proof of concept was accomplished in various experimental designs. Finally, the one that is described in the article [47] (cf. Fig 8.2) achieved the required measurement accuracy comparable to regularly used contact sensors as, for example, Pt thermometers. The results were eventually passed onto Komatsu Electronics, which finalized this work in a commercial device [193].

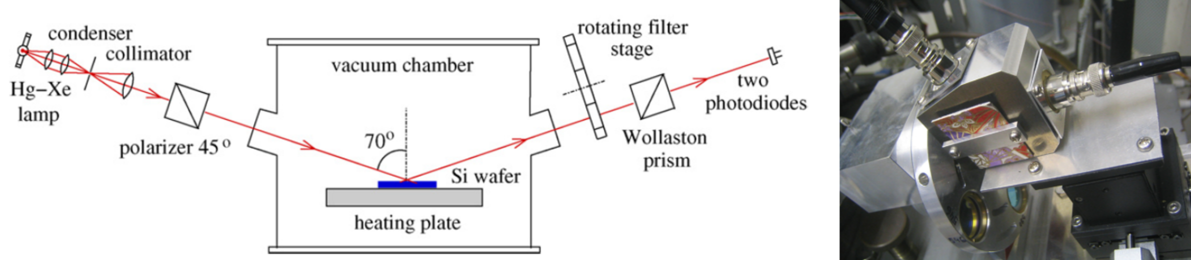

Fig. 8.2: Proof of concept (left, reprinted from [47]) and photography of a detection unit (right).

8.3 ELLA-CS, s.r.o., Czech Republic

This research was motivated by a demand for increased biocompatibility of stainless steel coronary stents – human body medical implants. This has been realized by coating them with a thin layer of nanocrystalline diamond. The interdisciplinary consortium that carried out this activity in the frame of BIOKOM project consisted of (i) Institute of Physics, Czech Academy of Sciences - deposition of nanocrystalline diamond films (tuning of deposition parameters) and their characterization (ii) University of Pardubice - complementary characterization of diamond layers by spectroscopic ellipsometry, (iii)

3rd Medical Faculty, Charles University - design and realization of an animal model, in–vivo tests and final evaluation of surface-functionalized implant biocompatibility (iv) ELLA–CS, s.r.o., stent manufacturer - expert consultations and stent supplier.

MW–PECVD apparatus based on an innovative plasma source with a set of 4 linear antennas [194] was used for the stent coating. When searching for a suitable pulsed plasma frequency and substrate deposition temperature for nanocrystalline diamond, the spectroscopic ellipsometry provided significant results, which helped determine the diamond quality of the diamond layers and their internal structure (distinguishing seed and bulk sub–layers). The obtained results were complemented with Raman spectroscopy and scanning microscopic methods, AFM and SEM, which helped reduce the correlations between the fitted parameters, for more detail see Section 3.5.1 and paper [94]. Coronary stents, coated with tuned deposition conditions, were implanted into a group of pigs (animal model), and subsequently, their improved surface biocompatibility was evaluated in–vivo through optical coherence tomography. The details of the animal model study and the final results are published in [195].

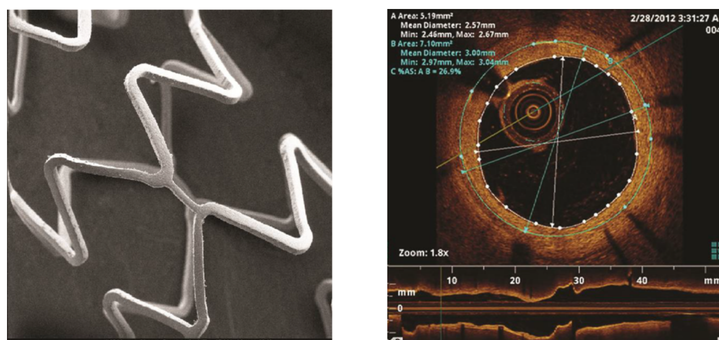

Fig. 8.3: SEM image of NCD coated stent (left) and in–vivo evaluation of neointimal hyperplasia by optical coherence tomography (right, reprinted from [195]).

8.4 TOSEDA, s.r.o., Czech Republic

Optical properties of organic polymers and co–polymers were examined in the middle infrared spectral range. This knowledge facilitated the assessment of the potential use of these materials as an optical matching glue for optical elements that are designed for space applications.

8.5 Synthesia, a.s. Czech Republic

Knowledge of optical properties of pigments used for color decoration is often very important from both technology and application viewpoints. Spectral dependence of pigment particle complex refractive index, together with the particle size, determines the final color of a pigment coating. Moreover, pigment particle size, a parameter controlled

in the manufacturer site, is usually indirectly measured by the dynamic light scattering, and in this method, the refractive index of pigment particles for the excitation beam wavelength is needed.

In this research, we introduced a novel application of spectroscopic ellipsometry for organic pigment optical characterization. Pressing pigments powders into the form of high-density pellets with optical surface quality enabled determination of pigments optical constants in the DUV-VIS-NIR spectral range. Special care was devoted to the verification of the structural identity of the obtained pellets and the initial powders. This was done by Raman spectroscopy. The results are summarised in Fig. 8.4. For more details refer to [196].

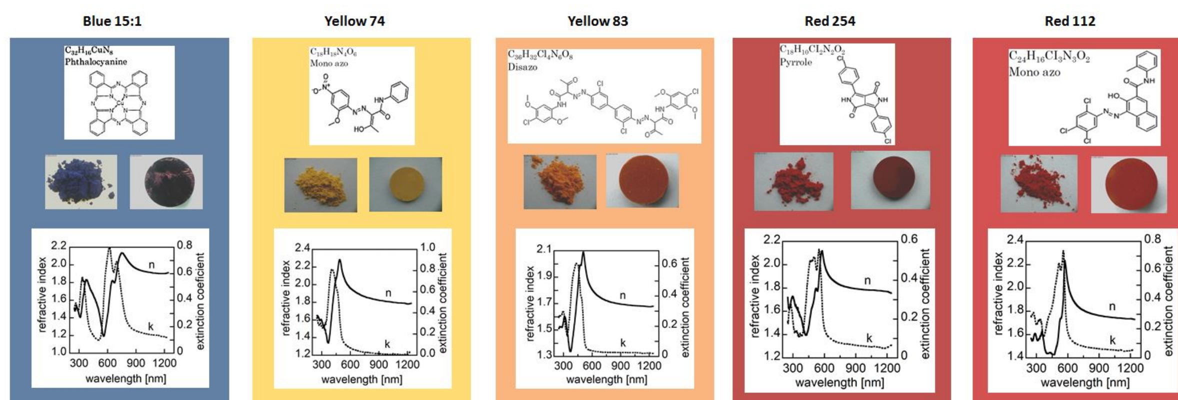

Fig. 8.4: Optical constants of the studied pigments.

Part III

Selected papers

Chapter 9

List of selected publications

1. **Magneto-optical Polar and Longitudinal Kerr Spectra of $NiFe_2O_4$ Single-crystal**
J. Mistrík, S. Visnovsky, J. Grondilova, N.Keller, M.Guyot, and R. Krishnan, J. Magn. Soc. Japan **25**, 267 (2001); doi: 10.3379/jmsjmag.25.267

2. **Optical properties of rough $LaNiO_3$ thin films studied by spectroscopic ellipsometry and reflectometry**
J. Mistrík, T. Yamaguchi, D. Franta, I. Ohlidal, G. Hu, and N. Dai, Applied Surface Science **244**, 431 (2005); doi: 10.1016/j.apsusc.2004.09.151

3. **Evidence of native oxide on the capping and substrate of Permalloy gratings by magneto-optical spectroscopy in the zeroth- and first- diffraction orders**
R. Antos, J. Mistrík, T. Yamaguchi, S. Visnovsky, S. Demokritov, and B. Hillebrands, Applied Physics Letters **86**, 1 (2005); doi: 10.1063/1.1944904

4. **Magneto-optical and optical spectroscopic ellipsometries of $La_{2/3}Sr_{1/3}MnO_3$ thin films**
J. Mistrík, T. Yamaguchi, M. Veis, E. Liskova, S. Visnovsky, M. Koubaa, A. Haghiri-Gosnet, P. Lecoeur, J. Renard, W. Prellier, and B. Mercey, Journal of Applied Physics **99**, 08Q317 (2006); doi: 10.1063/1.2172908

5. **Optical measurements of silicon wafer temperature**
K. Postava, M. Aoyama, J. Mistrík, T. Yamaguchi, and K. Shio, Applied Surface Science **254**, 416 (2007); doi: 10.1016/j.apsusc.2007.07.086

6. **Spectroscopic ellipsometry characterization of nano-crystalline diamond-films prepared at various substrate temperatures and pulsed plasma frequencies using microwave plasma enhanced chemical vapor deposition apparatus with linear antenna delivery**
J. Mistrík, P. Janicek, A. Taylor, F. Fendrych, L. Fekete, A. Jager, and M. Nesladek, Thin Solid Films **571**, 230 (2014); doi: 10.1016/j.tsf.2014.10.071

7. **Optical and magneto-optical behavior of Cerium Yttrium Iron Garnet thin films at wavelengths of 200-1770 nm**
   M. Onbasli, L. Beran, M. Zahradník, M. Kucera, R. Antoš, J. Mistrík, G. Dionne, M. Veis, and C. Ross, Scientific Reports **6**, 23640 (2016); doi: 10.1038/srep23640

8. **A 1D conical nanotubular** TiO_2/CdS **heterostructure with superiror photon-to-electron conversion**
   R. Zazpe, H. Sopha, J. Prikryl, M. Krbal, J. Mistrík, F. Dvorak, L. Hromadko, and J. Macak, Nanoscale **10**, 16601 (2018); doi: 10.1039/c8nr02418a

Perspectives

There are a plethora of tools devoted to the characterization of nanomaterials. Among them, optical and magneto–optical ellipsometry are maturated techniques that are still growing due to their significant advantages. Some of these have been mentioned in this thesis already. They are non–destructive, phase–sensitive, and thickness selective owing to the penetration depth wavelength dependence. The latter enables distinguishing surface and volume sample properties. Light spot size can cover a relatively large area, averaging sample properties over several mm squared, or can be focused down to tens-of-micrometers. For better lateral resolution (down to a micron) imaging alternatives are available as well. Both ex–situ table–top ellipsometers with a high spectral resolution and ultra–fast in–situ ellipsometers studying various kinetics with a limited number of wavelengths exist. Several types of commercial ellipsometers cover a broad spectral range from terahertz to VUV. Moreover, synchrotron facilities enable covering X-Ray as well. Thus, selecting the appropriate spectra range for a specific application is relatively easy. Recent theoretical advancements in RCWA calculations facilitated expanding ellipsometry from layered systems to laterally patterned samples and to photonic crystals in general. A large database of optical and magneto–optical constants is available for designing new devices. A relatively simple experimental set-up that does not require cumbersome components (for example high vacuum) is another benefit of ellipsometry over, for example, scanning probe methods.

Moreover, magneto–optical spectroscopy proved to be successful for magnetic monolayer detection, element specificity by X–ray magnetic circular dichroism where core electrons are excited [197, 198], and high dynamic response suitable for observation of ultrafast remagnetization processes [199]. This combination of characteristics is unique among other characterization tools. In addition, magnetic ordering of interfaces and surfaces can be effectively probed by non–linear magneto-optics owing to the broken symmetry that yields second harmonic polarizability [200]. Noteworthy, the mono–layer detection sensitivity enables characterization of atomically thin two–dimensional materials as, for example graphene, transition metal dichalcogenides, or black phosphorus with large optical and magneto–optical anisotropies and new magnetic properties that represents promising candidates in modern frontier applications [201]. Sensitivity to spin-orbit interaction enables probing subtle exchange interactions of magnetic sub–lattices in ferrimagnets, weak ferromagnets, and anti–ferromagnets. The exchange coupling in magnetic multilayers or composite nanostructures is observable by magneto-optics as well. Furthermore, quadratic magneto–optical effects are beneficial due to their fine detection of the crystallographic

orientation of cubic crystals. In addition, magneto–optical imaging is the appropriate method for magnetic domain wall observation and examination of its evolution during remagnetization [202].

The continuous search for new (nano)materials with unique optical, magnetic, or structural properties that would open new pathways in multi-disciplinary applications motivates further development of the optical and magneto-optical ellipsometry instrumentation together with the refinement of theoretical approaches coming out of standard approximations. For example, higher spatial resolution is realized by near-field (magneto)optical methods [203]. Time-resolved quadratic MO effect with the pump-probe method was recently used for the characterization of antiferromagnetic materials with promising applications in spintronics [204]. A new non–reciprocal magnetophonon Raman scattering effect was observed in ferromagnetic few–layer CrI_3 [205]. Modern on-chip integrated photonic devices employing, for example, giant optical anisotropy for light manipulation owing to birefringence phenomena [206], high refractive contrast in phase-change materials for directional coupler switches [176], or high magneto-optical figure of merit for isolators, rotators, and modulators profitably uses the potential of optical and magneto-optical ellipsometry and continuously increasing database of optical and magneto-optical constants of new attractive materials. This is also valid for tuning optical properties of photosensitizers for effective solar energy harvesting in photovoltaic devices or photodynamic (photothermal) therapy of cancer or infection treatment [207] showing a rather broad and active application of both ellipsometries. Magneto–optics significantly contributed to the elucidation of giant magnetoresistivity, the effect recently employed in high-density recording media. Magneto–optical memory discs with ever-increasing capacity are under research as well.

Regarding recent refinement of theoretical approaches devoted to the interaction of light with nanostructured materials on which optical and magneto–optical ellipsometry are based, one should mention, for example, the improvement of convergence in RCWA for scatterometry, incorporation of thin–film non-idealities into the standard thin–film optics [89] and taking into consideration partial light coherence. In addition, continuous advances in the accuracy of ab-initio calculations and molecular dynamics for design and prediction of novel nano–materials and heterostructures with desired optical and magneto–optical properties are worth mentioning as well.

Acknowledgement

I am grateful to all my colleagues and co–workers that helped me, during the last more than twenty years, to gain numerous experiences in various fields of experimental and theoretical physics. In particular, I am thankful to Prof. Š. Višňovský and Assoc. prof. M. Nývlt (Charles University, Prague) for introducing me to magneto-optics, to Dr. M. Guyot and Dr. N. Keller (University of Versailles, France) for strengthening me in magnetism, and to Prof. T. Yamaguchi (Shizuoka University, Japan) for sharing his expertise in spectroscopic ellipsometry. My acknowledgment also belongs to numerous foundations, agencies, and companies for their financial support enabling my work. Last but not least, I deeply value the long–lasting support of my parents, my wife, and my children.

References

[1] R. M. A. Azzam and N. M. Bhashara, *Elipsometry and Polarized Light* (North Holland, Amsterdam-New York-Oxford, 2003).

[2] M. Born and E. Wolf, *Principles of Optics* (Cambridge University Press, Cambridge, UK, 1999).

[3] C. Brosseau, *Fundamentals of polarized light; a statistical optics approach* (John Wiley & Sons Inc, London-New York-Sydney-Toronto, 1998).

[4] P. Drude, Ann. Phys. **272**, 865 (1889).

[5] P. Drude, Ann. Phys. **272**, 532 (1889).

[6] P. Drude, Ann. Phys. **39**, 481 (1890).

[7] M. Faraday, Phil. Trans. Roy. Soc. (London) **136**, 1 (1846).

[8] J. Kerr, Rep. Brit. Ass. **5**, (1876).

[9] N. Voigt, *Magneto und Electrooptik* (G. B. Teubner, Leipzig, 1908).

[10] P. Zeeman, Phil. Mag. **(5) 28**, 226 (1897).

[11] C. G. Darwin, Proc. Roy. Soc. **151**, 512 (1935).

[12] M. Losurdo and K. e. Hingerl, *Ellipsometry at the Nanoscale* (Springer, Heidelberg, Germany, 2013).

[13] J. Mistrík, in *Optical Properties of Materials and Their Applications*, *Wiley Series in Materials for Electronic and Optoelectronic Applications*, 2nd ed., edited by J. Singh (John Wiley & Sons, Chichester, England, 2019), Chap. 15, pp. 435–464.

[14] L. D. Landau and E. M. Lifshitz, *Electrodynamics of Continuous Media* (Pergamon Press, Inc., New York, 1960).

[15] P. S. Pershan, J. Appl. Phys. **38**, 1482 (1967).

[16] J. Humlicek, *Polarized Light and Ellipsometry. In: Handbook of Ellipsometry* (eds. Tompkins, H. G. and Irene, E. A., Springer, Heidelberg, Germany, 2005).

[17] P. Fumagalli, Habilitation thesis, Rheinisch–Westfalischen Technischen Hochschule Aachen, 1997.

[18] F. Wooten, *Optical Properties of Solids* (Academic Press, New York - London, 1972).

[19] R. W. Colins and A. S. Ferlauto, *Optical Physics of Materials. In: Handbook of Ellipsometry* (eds. Tompkins, H. G. and Irene, E. A., Springer, Heidelberg, Germany, 2005).

[20] W. Wettling, J. Magn. Magn. Mater. **3**, 147 (1976).

[21] A. K. Zvezdin and V. A. Kotov, *Modern magnetooptics and magnetooptical materials*, 1 ed. (Taylor & Francis, New York, 1997).

[22] Y. B. Band, *Light and matter*, 2 ed. (Wiley, Chichester, 2006).

[23] L. Onsager, Phys. Rev. **37**, 405 (1931).

[24] S. Višňovský, Czech. J. Phys. B **36**, 1424 (1986).

[25] S. Visnovsky, Czech. J. Phys. B **36**, 1424 (1986).

[26] K. Postava, H. Jaffres, A. Schuhl, F. Van Dau, M. Goiran, and A. Fert, Journal of Magnetism and Magnetic Materials **172**, 199 (1997).

[27] J. Hamrlová, J. Hamrle, K. Postava, and J. Pištora, Physica Status Solidi (B) Basic Research **250**, 2194 (2013).

[28] K. Postava, D. Hrabovský, J. Pištora, A. Fert, S. Višňovský, and T. Yamaguchi, Journal of Applied Physics **91**, 7293 (2002).

[29] K. Postava, J. Pistora, D. Ciprian, D. Hrabovsky, M. Lesnak, and A. Fert, Proceedings of SPIE - The International Society for Optical Engineering **3820**, 412 (1999).

[30] S. Visnovsky, Cs. Cas. fyz. **40**, 559 (1990).

[31] M. Onbasli, L. Beran, M. Zahradník, M. Kucera, R. Antoš, J. Mistrík, G. Dionne, M. Veis, and C. Ross, Scientific Reports **6**, 23640 (2016).

[32] L. Novotny and B. Hecht, *Principles of nano-optics*, 1st ed. ed. (Cambridge University Press, New York, 2006).

[33] D. Y. Smith, *Theoretical Aspects and New Developments in Magneto-Optics* (Springer US, Boston, MA, 1980), pp. 133–182.

[34] R. Collins and K. Vedam, *Optical properties of solids. In: Encyclopedia of Applied Physics* (Wiley-VCH, Chichester, UK, 1995).

[35] H. Fujiwara, *Spectroscopic Ellipsometry, Principles and Applications* (Wiley, Chichester, UK, 2007).

[36] J. Mistrík, S. Kasap, H. E. Ruda, C. Koughia, and J. Singh, in *Springer Handbook of Electronic and Photonic Materials*, 2nd ed., edited by S. Kasap and P. Capper (Springer International Publishing, Berlin, Heidelberg, 2017), Chap. 3, pp. 47–84.

[37] H. A. Lorentz, *The theory of electrons and its applications to the phenomena of light and radiant heat* (Dover Publications, Mineola, N.Y., 2003).

[38] V. Švorčík, J. Siegel, P. Šutta, J. Mistrík, P. Janíček, P. Worsch, and Z. Kolská, Applied Physics A: Materials Science and Processing **102**, 605 (2011).

[39] V. Švorčík, Z. Kolská, T. Luxbacher, and J. Mistrík, Materials Letters **64**, 611 (2010).

[40] T. Syrovy, P. Janicek, J. Mistrík, K. Palka, P. Hawlova, L. Kubac, and M. Gunde, Synthetic Metals **227**, 139 (2017).

[41] A. Taylor, L. Fekete, P. Hubik, A. Jager, P. Janicek, V. Mortet, J. Mistrik, and J. Vacik, Diam. Relat. Mater **47**, 27 (2014).

[42] P. Janicek, K. Niang, J. Mistrík, K. Palka, and A. Flewitt, Applied Surface Science **421**, 557 (2017).

[43] J. Mistrík, K. Takahashi, R. Antos, M. Aoyama, T. Yamaguchi, Y. Anma, Y. Fukuda, M. Takeyama, A. Noya, Z.-T. Jiang, S. Thurgate, and G. Riessen, Thin Solid Films **455-456**, 473 (2004).

[44] D. Franta, I. Ohlídal, and D. Munzar, Acta Physica Slovaca **48**, 451 (1998).

[45] D. Franta, I. Ohlídal, V. Buršíková, and L. Zajíčková, Thin Solid Films **455-456**, 393 (2004).

[46] P. Y. Yu and M. Cardona, *Fundamentals of semiconductors*, 4th ed ed. (Springer, Berlin, 2010).

[47] K. Postava, M. Aoyama, J. Mistrík, T. Yamaguchi, and K. Shio, Applied Surface Science **254**, 416 (2007).

[48] K. Pálka, M. Vlček, and J. Mistrík, Journal of Optoelectronics and Advanced Materials **13**, 1510 (2011).

[49] P. Janicek, S. Funke, P. Thiesen, S. Slang, K. Palka, J. Mistrík, M. Grinco, and M. Vlcek, Thin Solid Films **660**, 759 (2018).

[50] M. Veis, S. Višňovsky, P. Lecoeur, A.-M. Haghiri-Gosnet, J.-P. Renard, P. Beauvillain, W. Prellier, B. Mercey, J. Mistrík, and T. Yamaguchi, Journal of Physics D: Applied Physics **42**, 195002 (2009).

[51] K. Mak, C. Lee, J. Hone, J. Shan, and T. Heinz, Physical Review Letters **105**, 136805 (2010).

[52] P. H. Lissberger and M. R. Parker, Journal of Applied Physics **42**, 1708 (1971).

[53] R. Carey and B. Thomas, Journal of Physics D: Applied Physics **7**, 2362 (1974).

[54] H. Hulme, Proc. Roy. Soc. (London) **A135**, 237 (1932).

[55] C. Kittel, Phys. Rev. **83**, A208 (1951).

[56] P. Argyres, Phys. Rev. **97**, 3349 (1955).

[57] H. Bennett and E. Stern, Phys. Rev. **A448**, (1965).

[58] J. F. Kahn, P. S. Pershan, and J. P. Remeika, Phys. Rev. **186**, 891 (1969).

[59] D. Y. Smith, Phys. Rev. **13**, 5303 (1976).

[60] D. R. Hartree, Mathematical Proceedings of the Cambridge Philosophical Society **24**, 111–132 (1928).

[61] L. H. Thomas, Math. Proc. Cambridge. Philos. Soc. **23**, 542 (1927).

[62] Z. Fermi, Phys. A: Hadrons Nucl. **48**, 73 (1928).

[63] W. Kohn and L. J. Sham, Phys. Rev. **140**, A1133 (1965).

[64] O. Gunnasson and B. I. Lundquist, Phys. Rev. B **13**, 4274 (1976).

[65] U. von Barth and L. J. Hedin, Phys. C **5**, 1629 (1972).

[66] J. Kubo, J. Phys. Soc. Jpn. **12**, 570 (1957).

[67] C. Wang and J. Callaway, Phys. Rev. B **9**, 4897 (1974).

[68] P. Oppeneer, T. Mauret, J. Sticht, and J. Kubler, Phys. Rev. B **45**, 10924 (1992).

[69] J. Kunes, Physica Scripta **T109**, 116 (2004).

[70] J. Kunes and P. M. Oppeneer, Trans. Mag. Soc. Japan. **2**, 141 (2002).

[71] J. Kuneš and J. Mistrík, Physica Status Solidi (B) Basic Research **220**, 991 (2000).

[72] M. Schubert, B. Rheinländer, J. Woollam, B. Johs, and C. Herzinger, Journal of the Optical Society of America A: Optics and Image Science, and Vision **13**, 875 (1996).

[73] H. G. Tompkins and E. A. Irene, *Handbook of Ellipsometry* (Springer, Heidelberg, Germany, 2005).

[74] O. Cermakova and S. Visnovsky, Czech. J. Phys. B **36**, 537 (1986).

[75] Garcia-Caurel, R. E., Ossikovski, and M. Foldyna, *Advanced Mueller Ellipsometry instrumentation and data analyses. In: Ellipsometry at the Nanoscale* (eds. Losurdo M. and Hingerl K., Springer., Heidelberg, Germany, 2013).

[76] H. G. Tompkins and E. A. Irene, *Instrumentation. In: Handbook of Ellipsometry, Part II* (Springer, Heidelberg, Germany, 2005).

[77] D. E. Aspnes, J. Opt. Soc. Am. **64**, 639 (1973).

[78] J. Mistrík, S. Visnovsky, J. Grondilova, N.Keller, M.Guyot, and R. Krishnan, J. Magn. Soc. Japan **25**, 267 (2001).

[79] G. Finch and A. Quarrell, Nature **137**, 516 (1936).

[80] L. Ward, *The Optical Constants of Bulk Materials and Films* (Adam Hilger., Bristol and Philadelphia, 1988).

[81] J. Mistrík, M. Aoyama, T. Yamaguchi, and N. Dai, UVSOR Activity Report **87** (2005).

[82] D. Franta, I. Ohlídal, J. Mistrík, T. Yamaguchi, G. Hu, and N. Dai, Applied Surface Science **244**, 338 (2005).

[83] J. Mistrík, T. Yamaguchi, N. Dai, and M. Shimizu, UVSOR activity report 87 (2004).

[84] I. Ohlídal and D. Franta, Progress in Optics **41**, 181 (2000).

[85] C. M. Herzinger, B. Johs, and W. A. McGahan, J. Appl. Phys. **83**, 3323 (1998).

[86] G. J. Jellison and F. Modine, Appl. Phys. Lett. **69**, 371 (1996).

[87] W. Jackson, N. Amer, A. Boccara, and D. Fournier, Appl. Opt. **20**, 1333 (1981).

[88] R. Swanepoel, J. Phys. E **17**, 896 (1984).

[89] I. Ohlídal, M. Čermák, and J. Vohánka, in *Optical Characterization of Thin Solid Films*, edited by O. Stenzel and M. Ohlídal (Springer International Publishing, Cham, 2018), pp. 271–313.

[90] J. Mistrík, I. Ohlidal, R. Antos, M. Aoyama, and T. Yamaguchi, Applied Surface Science **244**, 51 (2005).

[91] O. S. Heavens, *Optical Properties of Thin Solid Films* (Dover Publications, New York, 1965/1991).

[92] M. Kildemo, O. Hunderi, and B. Drevillon, J. Opt. Soc. Am. A **14(4)**, 931 (1997).

[93] A. Vasicek, *Optics of Thin Films.* (Interscience Publishers, New York, 1960).

[94] J. Mistrík, P. Janicek, A. Taylor, F. Fendrych, L. Fekete, A. Jager, and M. Nesladek, Thin Solid Films **571**, 230 (2014).

[95] For a review, see for example (J. Humlicek (2013). Data analyses for Nanomaterials: effective medium approximation, its limits and implementations. In: Ellipsometry at the Nanoscale (eds. M. Losurdo and K. Hingler) Ch. 3. Springer, and D.E. Aspnes (1982). Thin Solid Films, 89: 249.

[96] D. A. G. Bruggeman, Ann. Phys. **24**, 636 (1935).

[97] D. Edwards and H. Philipp, *Handbook of Optical Constants of Solids* (ed. E. D. Palik, Academic Press, INC., Orlando, 1985).

[98] Database of optical constants of solids, (http://sspectra.com/sopra.html).

[99] See for example: Bergmair, M., Hingerl, K., and Zeppenfeld, P. (2013). Spectroscopic Ellipsometry on metallic gratings. In: Ellipsometry at the Nanoscale (eds. M. Losurdo and K. Hingerl). Ch. 7. Springer.

[100] M. Veis and R. Antos, J. Nanomater **2013**, 621531 (2013).

[101] H. Huang and F. J. Terry, Thin Solid Films **455-456**, 828 (2004).

[102] T. Novikova, A. De Martino, P. Bulkin, Q. Nguyen, B. Drévillon, V. Popov, and A. Chumakov, Optics Express **15**, 2033 (2007).

[103] J. Zhu, S. Liu, X. Chen, C. Zhang, and H. Jiang, Optics Express **22**, 22031 (2014).

[104] K. Rokushima and J. Yamakita, J. Opt. Soc. Am. **73**, 901 (1983).

[105] K. Rokushima, R. Antos, J. Mistrik, S. Vusnovsky, and T. Yamaguchi, Czechoslov. J. Phys. **56**, 665 (2006).

[106] S. Visnovsky, *Optics in Magnetic Multilayers and Nanostructures* (CRC Press, Taylor & Francis, 2006).

[107] K. Yee, IEEE Antennas Propag. Mag. **14**, 302 (1966).

[108] J. Hugonin and L. L., Reticolo software for grating analyses. Technical Report, Institut d'Optique, Orsay, France (2005).

[109] J. Mistrík, M. Karlovec, K. Palka, and R. Antos, 2017 IEEE International Conference on Computational Electromagnetics, ICCEM 2017 298 (2017).

[110] R. Antos, J. Pistora, J. Mistrík, T. Yamaguchi, S. Yamaguchi, M. Horie, S. Visnovsky, and Y. Otani, Journal of Applied Physics **100**, 054906 (2006).

[111] J. Mistík, Master thesis, Univerzita Karlova, Prague, Czech, 1998, 64 pages.

[112] K. Postava, A. Maziewski, A. Stupakiewicz, A. Wawro, L. Baczewski, S. Visnovsky, and T. Yamaguchi, Journal of the European Optical Society **1**, 1 (2006).

[113] M. Billardon, Ann. Phys. **7**, 233 (1962).

[114] H. G. Jerrard, Surface Sci. **16**, 137 (1969).

[115] I. Williams, Surface Sci. **16**, 174 (1969).

[116] H. J. Mathieu, D. E. McClure, and R. H. Muller, Rev. Sci. Instr. **45**, 798 (1974).

[117] H. Takasaki, J. Opt. Soc. Am. **51**, 463 (1961).

[118] H. Takasaki, J. Opt. Soc. Am. **56**, 557 (1966).

[119] H. Takasaki, Appl. Opt. **5**, 759 (1966).

[120] D. E. Aspnes, *Spectroscopic Ellipsometry of Solids. In: Optical Properties of Solids New Developments* (eds. Seraphin, B. O., Nort-Holland Publishing Company, Amsterdam, Oxford, 1976).

[121] S. Višňovský (unpublished).

[122] M. Nývlt, PhD. dissertation, Charles University in Prague, 1996.

[123] K. Postava, PhD. dissertation, Palacky University, Olomouc, Czech & Institut national des Sciences Appliquees, Toulous, France, 1997.

[124] S. Visnovsky, Czech. J. Phys. B **37**, 218 (1987).

[125] G. S. Krinchik and A. V. Artemjev, Zh. Exp. Teor. Fiz. **53**, 1901 (1967).

[126] J. Mistík, Doctoral thesis, Université de Versailles Saint–Quentin-en-Yvelines, Versailles, France, 2002.

[127] G. S. Krinchik, K. M. Mukimov, S. M. Sharipov, A. P. Chrebtov, and E. M. Speranskaya, Zh. Exp. Teor. Fiz. **72**, 697 (1977).

[128] A. M. Clogston, J. Appl. Phys. **31**, 198 Suppl. (1960).

[129] D. L. Wood, B. Ding, and B. Liu, Nano Select **1**, 298 (2020).

[130] S. Visnovsky, R. Krishnan, M. Nyvlt, and V. Prosser, J. Magn. Soc. Jpn. **41**, Suppl. S1 (1996).

[131] K. Postava, J. Pistora, and S. Višňovský, Czech. J. Phys. **49**, 1185 (1998).

[132] K. Postava, J. Pistora, R. Kantor, A. R. Fert, M. Goiran, A. Schuhl, and F. Nguyen van Dau, in *X Polish-Czech-Slovak Optical Conference - Wave and quantum aspects of contemporary optics* (Wroclav, Poland, 17-20 September 1996).

[133] A. V. Sokolov, *Opticeskie svojstva metalov* (Gasudarstvenoje izdavatelstvo fiziko-matematiceskoj literatury, Moskva, 1961).

[134] K. Postava, J. Pištora, and T. Yamaguchi, Sensors and Actuators, A: Physical **110**, 242 (2004).

[135] I. Kopriva, D. Hrabovsky, K. Postava, D. Ciprian, J. Pistora, and A. Fert, Proceedings of SPIE - The International Society for Optical Engineering **4016**, 54 (2000).

[136] O. Stejskal, R. Silber, J. Pištora, and J. Hamrle, Photonics and Nanostructures - Fundamentals and Applications **32**, 24 (2018).

[137] R. Silber, O. Stejskal, L. Beran, P. Cejpek, R. Antoš, T. Matalla-Wagner, J. Thien, O. Kuschel, J. Wollschläger, M. Veis, T. Kuschel, and J. Hamrle, Physical Review B **100**, 064403 (2019).

[138] S. Visnovsky, Czech. J. Phys. B **36**, 834 (1986).

[139] S. Višňovský, R. Lopušník, M. Nývlt, V. Prosser, J. Ferré, C. Train, P. Beauvillain, D. Renard, R. Krishnan, and J. Bland, Czech. J. Phys. **50**, 857 (2000).

[140] M. Mansuripur, *The physical Principles of Magneto–optical Recording* (Cambridge University Press, UK, 2009).

[141] M. Mansuripur, *Classical Optics and its Applications* (Cambridge University Press, UK, 1995).

[142] F. Cracuin, P. Verardi, M. Dinescu, and G. Guidarelli, Thin Solid Films **343-344**, 90 (1999).

[143] M. Mayevskii, V., Phys. Met. Metalloved **59**, 1 (1985).

[144] D. O. Smith, Opt. Acta **12**, 13 (1965).

[145] P. Yeh, Surf. Sci. **96**, 41 (1980).

[146] S. Visnovsky, Czech. J. Phys. **41**, 663 (1991).

[147] S. Visnovsky, J. Magn. Soc. Japan **15**, 67 (1991).

[148] R. Atkinson, J. Magn. Magn. Mater **118**, 271 (1993).

[149] A. McGahan, W. and J. A. Woollam, Applied Physics Communications **9**, 1 (1989).

[150] M. Mansuripur, J. App. Phys. **67**, 6466 (1990).

[151] J. Mistrík, R. Lopusnik, S. Visnovsky, N. Keller, M. Guyot, and R. Krishnan, Ferrites: Proceedings of the Eighth International Conference on Ferrites (ICF 8) 1015 (2000), Kyoto and Tokyo, Japan.

[152] N. Keller, M. Guyot, A. Das, M. Porte, and R. Krishnan, Solid State Communications **105**, 333 (1998).

[153] N. Keller, M. Guyot, A. Das, M. Porte, and R. Krishnan, IEEE Trans. Magn. **MAG-34**, 837 (1998).

[154] M.-T. Johnson, P.-G. Kotula, and C. Barry Carter, J. of Cryst. Growth **206**, 299 (1999).

[155] A. I. Galuza, V. V. Eremenko, and A. P. Kirichenko, Sov. Phys. Solid. State **21**, 654 (1979).

[156] P. C. Bailey, J. Appl. Phys. **31**, 39S (1960).

[157] R. Lopusnik, S. Visnovsky, N. Keller, M. Guyot, R. Krishnan, and M. Tessier, J. Magn. Soc. Jpn. **23**, S1(59) (1999).

[158] M. Grimsditch and W. Vavassori, J. Phys.: Condens, Matter **16**, R257 (2004).

[159] Y. Acremann, C. H. Back, M. Buess, O. Portman, A. Vaterlaus, D. Pescia, and H. Melchior, Science **290**, 492 (2000).

[160] T. Shinjo, T. Okuno, R. Hassdorf, K. Shigeto, and T. Ono, Science **289**, 930 (2000).

[161] A. Wachowiak, J. Wiebe, M. Bode, O. Pietzsch, M. Morgenstern, and R. Wiesendanger, Science **298**, 577 (2002).

[162] R. Antoš, J. Mistrík, M. Aoyama, T. Yamaguchi, S. Višňovský, and B. Hillebrands, Journal of Magnetism and Magnetic Materials **272-276**, 1670 (2004).

[163] R. Antos, J. Mistrík, T. Yamaguchi, S. Visnovsky, S. Demokritov, and B. Hillebrands, Optics Express **13**, 4651 (2005).

[164] R. Antos, J. Mistrík, T. Yamaguchi, S. Visnovsky, S. Demokritov, and B. Hillebrands, Applied Physics Letters **86**, 1 (2005).

[165] R. Antos, J. Mistrík, T. Yamaguchi, M. Veis, E. Liskova, S. Visnovsky, J. Pistora, B. Hillebrands, S. O. Demokritov, T. Kimura, and Y. Otani, J. Magn. Soc. Japan **30**, 630 (2006).

[166] O. N. Horpynyuk, V. N. Antonov, A. P. Shpak, and A. Plotnikov, N, Metallofizika i Noveishie Tekhnologii **28(12)**, 1603 (2006).

[167] M. Veis, R. Antos, S. Visnovsky, P. Kulkarni, N. Venkataramani, S. Prasad, J. Mistrík, and R. Krishnan, Materials **6**, 4096 (2013).

[168] J. Mistrík, T. Yamaguchi, M. Veis, E. Liskova, S. Visnovsky, M. Koubaa, A. Haghiri-Gosnet, P. Lecoeur, J. Renard, W. Prellier, and B. Mercey, Journal of Applied Physics **99**, 08Q317 (2006).

[169] L. Uba, S. Uba, L. Germash, L. Bekenov, and V. Antonov, Physical Review B - Condensed Matter and Materials Physics **85**, 125124 (2012).

[170] F. Haidu, M. Fronk, O. Gordan, C. Scarlat, G. Salvan, and D. Zahn, Physical Review B - Condensed Matter and Materials Physics **84**, 195203 (2011).

[171] N. Ogawa, T. Satoh, Y. Ogimoto, and K. Miyano, Physical Review B - Condensed Matter and Materials Physics **78**, 212409 (2008).

[172] J. Mistrík, T. Yamaguchi, D. Franta, I. Ohlidal, G. Hu, and N. Dai, Applied Surface Science **244**, 431 (2005).

[173] J. Pistora, M. Lesnak, E. Liskova, S. Visnovsky, I. Harward, P. Maslankiewicz, K. Balin, Z. Celinski, J. Mistrík, T. Yamaguchi, R. Lopusnik, and J. Vlcek, Journal of Physics D: Applied Physics **43**, 155301 (2010).

[174] D. Franta, B. Negulescu, L. Thomas, P. Dahoo, M. Guyot, I. Ohlídal, J. Mistrík, and T. Yamaguchi, Applied Surface Science **244**, 426 (2005).

[175] M. Krbal, V. Prokop, A. Kononov, J. Pereira, J. Mistrik, A. Kolobov, P. Fons, Y. Saito, S. Hatayama, Y. Shuang, Y. Sutou, S. Rozhkov, J. Stellhorn, S. Hayakawa, I. Pis, and F. Bondino, ACS Applied Nano Materials **4**, 8834 (2021).

[176] T. Y. Teo, M. Krbal, J. Mistrík, J. Prikryl, L. Lu, and R. E. Simpson, Opt. Mater. Express **12**, 606 (2022).

[177] A. Taylor, L. Fekete, P. Hubík, A. Jäger, P. Janíček, V. Mortet, J. Mistrík, and J. Vacík, Diamond and Related Materials **47**, 27 (2014).

[178] M. Veis, M. Kucera, M. Zahradnik, R. Antos, J. Mistrík, L. Bi, H.-S. Kim, G. Dionne, and C. Ross, Journal of Applied Physics **115**, 17A940 (2014).

[179] N. Keller, J. Mistrík, S. Višňovský, D. Schmool, Y. Dumont, P. Renaudin, M. Guyot, and R. Krishnan, European Physical Journal B **21**, 67 (2001).

[180] B. Berini, J. Mistrík, Y. Dumont, E. Popova, A. Fouchet, J. Scola, and N. Keller, Thin Solid Films **520**, 1890 (2012).

[181] J. Mistrík, B. Cechalova, J. Studynka, and V. Cech, Journal of Materials Science: Materials in Electronics **20**, S451 (2009).

[182] A. Babik, J. Mistrík, J. Zemek, and V. Cech, Journal of Adhesion Science and Technology **26**, 2543 (2012).

[183] L. Hoferek, J. Mistrík, R. Trivedi, K. Chen, V. Perina, and V. Cech, Surface and Coatings Technology **254**, 49 (2014).

[184] A. Jagerová, R. Mikšová, O. Romanenko, I. Plutnarova, Z. Sofer, P. Slepička, J. Mistrík, and A. Macková, Physical Chemistry Chemical Physics **23**, 22673 (2021).

[185] I. Ohlídal, J. Vohánka, J. Mistrík, M. Čermák, and D. Franta, Surface and Interface Analysis **50**, 1230 (2018).

[186] J. Mistrík, R. Krishnan, S. Visnovsky, N. Keller, A. Biondo, A. Franca De Souza, A. Mello, and E. Baggio-Saitovitch, Journal of Magnetism and Magnetic Materials **240**, 523 (2002).

[187] T. Kohoutek, J. Orava, J. Prikryl, J. Mistrík, T. Wagner, and M. Frumar, Optical Materials **32**, 154 (2009).

[188] R. Antos, J. Mistrík, M. Aoyama, T. Yamaguchi, S. Visnovsky, and B. Hillebrands, Transactions of the Magnetics Society of Japan **4**, 282 (2004).

[189] R. Zazpe, H. Sopha, J. Prikryl, M. Krbal, J. Mistrík, F. Dvorak, L. Hromadko, and J. Macak, Nanoscale **10**, 16601 (2018).

[190] R. Zazpe, H. Sopha, J. Charvot, R. Krumpolec, J. Rodriguez-Pereira, J. Michalička, J. Mistrík, D. Bača, M. Motola, F. Bureš, and J. Macak, Applied Materials Today **23**, 101017 (2021).

[191] I. Ohlídal, J. Vohánka, J. Mistrík, M. Čermák, F. Vižd'a, and D. Franta, Thin Solid Films **692**, 137189 (2019).

[192] Z.-T. Jiang, T. Yamaguchi, M. Aoyama, and T. Hayashi, Japanese Journal of Applied Physics, Part 1: Regular Papers and Short Notes and Review Papers **37**, 479 (1998).

[193] K. Shio, H. Wakai, K. K., and H. Akiba, Komatsu Technical Report **54**, 1 (2008).

[194] A. Taylor, F. Fendrych, L. Fekete, J. Vlček, V. Řezáčová, V. Petrák, J. Krucký, M. Nesládek, and M. Liehr, Diamond and Related Materials **20**, 613 (2011).

[195] V. Kocka, T. Jirasek, A. Taylor, F. Fendrych, B. Rezek, Z. Simunkovaa, I. Mraaová, P. Tousěk, J. Mistrík, V. Mandys, and M. Nesládek, Experimental and Clinical Cardiology **20**, 65 (2014).

[196] S. Sajdlova, Master thesis, Univerzita Hradec Kralove, Hradec Kralove, Czech, 2014, 60 pages.

[197] B. Thole, G. Van Der Laan, and G. Sawatzky, Physical Review Letters **55**, 2086 (1985).

[198] G. Van Der Laan, B. Thole, G. Sawatzky, J. Goedkoop, J. Fuggle, J.-M. Esteva, R. Karnatak, J. Remeika, and H. Dabkowska, Physical Review B **34**, 6529 (1986).

[199] M. Freeman, W. Hiebert, and A. Stankiewicz, Journal of Applied Physics **83**, 6217 (1998).

[200] J. Reif, C. Rau, and E. Matthias, Physical Review Letters **71**, 1931 (1993).

[201] T. Lan and J. P. Remeika, J. Appl. Phys. **37**, 1232 (1966).

[202] A. Hubert and R. Schafer, *Magnetic domains: the analyses of magnetic microstructures* (Springer, Berlin, 1998).

[203] E. Betzig, J. Trautman, R. Wolfe, E. Gyorgy, P. Finn, M. Kryder, and C.-H. Chang, Applied Physics Letters **61**, 142 (1992).

[204] V. Saidl, P. Němec, P. Wadley, V. Hills, R. Campion, V. Novák, K. Edmonds, F. Maccherozzi, S. Dhesi, B. Gallagher, F. Trojánek, J. Kuneš, J. Železný, P. Malý, and T. Jungwirth, Nature Photonics **11**, 91 (2017).

[205] Z. Liu, K. Guo, G. Hu, Z. Shi, Y. Li, L. Zhang, H. Chen, L. Zhang, P. Zhou, H. Lu, M.-L. Lin, S. Liu, Y. Cheng, X. Liu, J. Xie, L. Bi, P.-H. Tan, L. Deng, C.-W. Qiu, and B. Peng, Science Advances **6**, eabc7628 (2020).

[206] G. Ermolaev, D. Grudinin, Y. Stebunov, K. Voronin, V. Kravets, J. Duan, A. Mazitov, G. Tselikov, A. Bylinkin, D. Yakubovsky, S. Novikov, D. Baranov, A. Nikitin, I. Kruglov, T. Shegai, P. Alonso-González, A. Grigorenko, A. Arsenin, K. Novoselov, and V. Volkov, Nature Communications **12**, 854 (2021).

[207] N. Thorat, S. Tofail, B. Von Rechenberg, H. Townley, G. Brennan, C. Silien, H. Yadav, T. Steffen, and J. Bauer, Applied Physics Reviews **6**, 041306 (2019).

Appendixes A

Single interface reflection matrix

Provided are elements of reflection matrix expressed as a function of material permittivity tensor ε (considered in a general form) and proper numbers $\bar{N}_z$ of the wave equation. For more detail, refer to Section 4.3.

Diagonal elements:

$$r_{ss} = \frac{P+Q-S-T}{P+Q+S+T}, \tag{A.1}$$

$$r_{pp} = \frac{P-Q+S-T}{P+Q+S+T}, \tag{A.2}$$

where

$$\begin{aligned} P = N_0{\alpha_z}^2(&\varepsilon_{13}\varepsilon_{33}\bar{N}_z^+\bar{N}_z^-\bar{N}_y(\bar{N}_z^+ + \bar{N}_z^-) \\ &-\varepsilon_{33}[\varepsilon_{12}(\varepsilon_{33}-\bar{N}_y^2)-\varepsilon_{13}\varepsilon_{32}][\bar{N}_z^{+2}+\bar{N}_z^{-2}] \\ &-[\varepsilon_{12}\varepsilon_{33}(\varepsilon_{33}-\bar{N}_y^2)-\varepsilon_{13}\varepsilon_{32}(\varepsilon_{33}+\bar{N}_y^2)](\bar{N}_z^+\bar{N}_z^-) \\ &-\varepsilon_{32}\bar{N}_y[\varepsilon_{12}(\varepsilon_{33}-\bar{N}_y^2)-\varepsilon_{13}\varepsilon_{32}](\bar{N}_z^+ + \bar{N}_z^-) \\ &+[\varepsilon_{12}(\varepsilon_{33}-\bar{N}_y^2)-\varepsilon_{13}\varepsilon_{23}][\varepsilon_{33}(\varepsilon_{11}-\bar{N}_y^2)-\varepsilon_{13}\varepsilon_{31}] \\ &+\varepsilon_{13}\bar{N}_y^2[\varepsilon_{32}(\varepsilon_{11}-\bar{N}_y^2)-\varepsilon_{12}\varepsilon_{31}])\ , \end{aligned} \tag{A.3}$$

$$\begin{aligned} Q = N_0^2\alpha_z(&\varepsilon_{13}\bar{N}_y(\varepsilon_{33}-\bar{N}_y^2)(\bar{N}_z^+\bar{N}_z^-) \\ &-(\varepsilon_{33}-\bar{N}_y^2)[\varepsilon_{12}(\varepsilon_{33}-\bar{N}_y^2)-\varepsilon_{13}\varepsilon_{32}](\bar{N}_z^+ + \bar{N}_z^-) \\ &+\varepsilon_{13}\bar{N}_y[(\varepsilon_{11}-\bar{N}_y^2)(\varepsilon_{33}-\bar{N}_y^2)-\varepsilon_{13}\varepsilon_{31}])\ , \end{aligned} \tag{A.4}$$

$$\begin{aligned} S = \alpha_z(&\varepsilon_{13}\varepsilon_{33}\bar{N}_y(\bar{N}_z^+\bar{N}_z^-)^2 \\ &-\varepsilon_{33}[\varepsilon_{12}(\varepsilon_{33}-\bar{N}_y^2)-\varepsilon_{13}\varepsilon_{32}](\bar{N}_z^+\bar{N}_z^-)(\bar{N}_z^+ + \bar{N}_z^-) \\ &+\varepsilon_{13}\bar{N}_y[\varepsilon_{33}(\varepsilon_{11}-\bar{N}_y^2)-{\varepsilon_{13}}^2](\bar{N}_z^+\bar{N}_z^-) \\ &-\varepsilon_{32}\bar{N}_y[\varepsilon_{12}(\varepsilon_{33}-\bar{N}_y^2)-\varepsilon_{13}\varepsilon_{32}](\bar{N}_z^+\bar{N}_z^-) \\ &+\varepsilon_{13}\bar{N}_y^2[\varepsilon_{32}(\varepsilon_{11}-\bar{N}_y^2)-\varepsilon_{12}\varepsilon_{31}](\bar{N}_z^+ + \bar{N}_z^-) \\ &-\bar{N}_y[\varepsilon_{12}(\varepsilon_{33}-\bar{N}_y^2)-\varepsilon_{13}\varepsilon_{32}][\varepsilon_{32}(\varepsilon_{11}-\bar{N}_y^2)-\varepsilon_{12}\varepsilon_{31}])\ , \end{aligned} \tag{A.5}$$

$$T = \bar{N}_0(-(\varepsilon_{33} - \bar{N}_y^2)[\varepsilon_{12}(\varepsilon_{33} - \bar{N}_y^2) - \varepsilon_{13}\varepsilon_{32}](\bar{N}_z^+ \bar{N}_z^-)$$
$$+\varepsilon_{13}\bar{N}_y[(\varepsilon_{11} - \bar{N}_y^2)(\varepsilon_{33} - \bar{N}_y^2) - \varepsilon_{13}\varepsilon_{31}](\bar{N}_z^+ + \bar{N}_z^-)$$
$$-[\varepsilon_{12}(\varepsilon_{33} - \bar{N}_y^2) - \varepsilon_{13}\varepsilon_{32}][(\varepsilon_{11} - \bar{N}_y^2)(\varepsilon_{33} - \bar{N}_y^2) - \varepsilon_{13}\varepsilon_{31}]) \,. \tag{A.6}$$

Off-diagonal elements:

$$r_{sp}(P + Q + S + T) =$$
$$-2N_0\alpha_z(\varepsilon_{33}(\varepsilon_{33} - \bar{N}_y^2)(\bar{N}_z^+ \bar{N}_z^-)^2$$
$$-\varepsilon_{33}[(\varepsilon_{11} - \bar{N}_y^2)(\varepsilon_{33} - \bar{N}_y^2) - \varepsilon_{13}\varepsilon_{31}][(\bar{N}_z^+)^2 + (\bar{N}_z^-)^2]$$
$$+\varepsilon_{13}\varepsilon_{31}(\bar{N}_z^+ \bar{N}_z^-)\bar{N}_y^2 - \varepsilon_{31}\bar{N}_y[\varepsilon_{12}(\varepsilon_{33} - \bar{N}_y^2) - \varepsilon_{13}\varepsilon_{32}](\bar{N}_z^+ + \bar{N}_z^-)$$
$$+[(\varepsilon_{11} - \bar{N}_y^2)(\varepsilon_{33} - \bar{N}_y^2) - \varepsilon_{13}\varepsilon_{31}][\varepsilon_{33}(\varepsilon_{11} - \bar{N}_y^2) - \varepsilon_{13}\varepsilon_{31}]) \,, \tag{A.7}$$

$$r_{ps}(P + Q + S + T) = 2N_0\alpha_z((\varepsilon_{13})^2 \bar{N}_y^2(\bar{N}_z^+ \bar{N}_z^-)$$
$$-\varepsilon_{13}\bar{N}_y[\varepsilon_{12}(\varepsilon_{33} - \bar{N}_y^2) - \varepsilon_{13}\varepsilon_{32}](\bar{N}_z^+ + \bar{N}_z^-)$$
$$+[\varepsilon_{12}(\varepsilon_{33} - \bar{N}_y^2) - \varepsilon_{13}\varepsilon_{32}]^2) \,. \tag{A.8}$$